MODEL BASED VALIDATION SCHEME FOR ORGAN SEGMENTATION IN MEDICAL IMAGE DATA

by

Hossein Badakhshannoory

M.A.Sc, Sharif University of Technology, 2007

A Thesis submitted in partial fulfillment
of the requirements for the degree of
Master of Applied Science
in the School
of
Engineering Science

SIMON FRASER UNIVERSITY
Summer 2011

APPROVAL

Name:	Hossein Badakhshannoory
Degree:	Master of Applied Science
Title of Thesis:	Model Based Validation Scheme for Organ Segmentation in Medical Image Data
Examining Committee:	Dr. Carlo Menon Chair
	Dr. Parvaneh Saeedi, Senior Supervisor
	Dr. Bozena Kaminska, Supervisor
	Dr. Marinko Sarunic, Examiner
Date Approved:	June 14, 2011

Declaration of
Partial Copyright Licence

SFU SIMON FRASER UNIVERSITY
THINKING OF THE WORLD

STATEMENT OF ETHICS APPROVAL

The author, whose name appears on the title page of this work, has obtained, for the research described in this work, either:

(a) Human research ethics approval from the Simon Fraser University Office of Research Ethics,

or

(b) Advance approval of the animal care protocol from the University Animal Care Committee of Simon Fraser University;

or has conducted the research

(c) as a co-investigator, collaborator or research assistant in a research project approved in advance,

or

(d) as a member of a course approved in advance for minimal risk human research, by the Office of Research Ethics.

A copy of the approval letter has been filed at the Theses Office of the University Library at the time of submission of this thesis or project.

The original application for approval and letter of approval are filed with the relevant offices. Inquiries may be directed to those authorities.

Simon Fraser University Library
Simon Fraser University
Burnaby, BC, Canada

Last update: Spring 2010

Abstract

Model based methods have proven to be among the most reliable and robust solutions for application of medical image processing in organ segmentation and reconstruction. They assume a repetitive geometric pattern for the organ of interest and therefore utilize probabilistic models to characterize organs shape or other attributes. A common strategy, adopted by most of the model based methods, is to use model attributes as prior information in the actual segmentation process. In this work, we propose a novel approach for accurate 3D organ segmentation and modeling in the CT scan volumes. Instead of direct use of the organs prior information in the segmentation process, here we utilize the knowledge of the organ to validate a large number of potential segmentation hypotheses that are generated by a generic segmentation process. For this, PCA based organ space is utilized to measure the fidelity of each segment to the organ. We detail applications of the proposed method for 3D segmentation of human kidney and liver in CT scan volumes. For evaluation purposes, the public database of MICCAI 2007 grand challenge workshop has been used. Implementation results show an average Dice similarity measure of 90% for segmentation of the kidney which shows better results than the 88.6% presented by other kidney segmentation methods. For the liver, the proposed algorithm achieves an average volume overlap error of 8.7% and an average surface distance of 1.51 mm while the best reported average values for these measures are 6.65% and 1.03 mm by an automatic algorithm on the same dataset.

Acknowledgments

Here I would like to thank my supervisor, Dr. Parvaneh Saeedi, for admitting me to her group and giving me the opportunity to work as a member in her laboratory. Your time and hard work for supervising my project and providing me with the assistance and advice on different phases of my project are truly appreciated. I would also like to thank my supervisory committee for the time and energy they spent to review my work in this thesis. I would also like to thank the Natural Sciences and Engineering Research Council (NSERC) of Canada for providing the financial support for my research.

In the end I like to thank my family, my father, my mother and my sister that have always supported me throughout all different aspects of my life including my academic years. I cannot imagine to have achieved anything without their support.

Contents

List of Figures

List of Abbreviations

AAM	Active Appearance Model
AEM	Accumulative Edge Map
ASM	Active Shape Model
CT	Computed Tomography
DERMS	DEformable Registration and Multi-layer Segmentation
EEM	Enhanced Edge Map
EM	Edge Map
EMSI	Edge Map of Segmented Image
FN	False Negative
GUI	Graphical User Interface
MOVS	Model based Validation Scheme
MRI	Magnetic Resonance Imaging
MSE	Mean Square Error
PCA	Principal Component Analysis
TP	True Positive

Chapter 1

Introduction

The main objective of the work in this thesis is to automatically segment 3D organs from medical image data. Such a task is a part of every minimally invasive surgery [1]. Minimally invasive surgery is a modern surgical technique in which operations in the patient's body are performed through small incisions (usually 0.5 to 1.5 cm) as compared to the large openings that are usually required in open surgeries. Minimally invasive surgeries are preferred over traditional open surgeries since they require smaller incisions and therefore, are less invasive. They usually result in faster recovery time and with less trauma after surgery for the patient. They provide similar or better outcomes and have lower cost. Figure 1.1 compares the minimally invasive and open colon resection surgical procedures graphically. The dime size incisions in the minimally invasive approach are used to enter two or more endoscopes inside the patient's body to provide an indirect view to the organs inside the body which reduces the size of the incision on the belly, required for entering the surgical instruments, from 6-12 inches to 3-4 inches.

Perhaps all the above advantages explain the fast transition from traditional open surgeries to minimally invasive ones. In essence, this means replacing the direct view of the surgery sight with an indirect image based one. The challenge of this transition is to achieve similar accuracy and precision as the open surgeries through such visual feedbacks instead of a direct view. Due to the limited access and partial views of the organ under surgery during the procedure, a complete 3D reconstructed model of the organ, can provide additional information that may compensate for the lack of direct visual information. Such models are usually a representation of the organ in 3D space and are available to the surgeon through a software's Graphical User Interface (GUI). This 3D representation also provides

soft tissue properties through deformation simulations [2][3][4]. Providing a visual 3D model of organs and structures under the surgery, not only grants additional overall view of the patient specific anatomy but also augments the surgeon's ability to localize spatial features of anatomical organs by means of rotation and deformation of the 3D model.

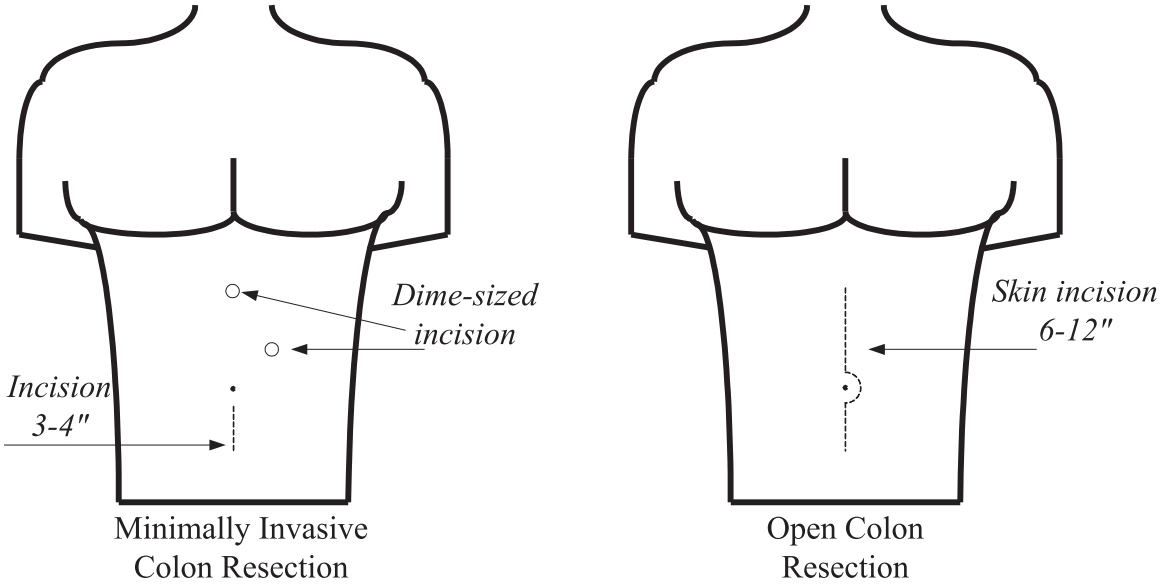

Figure 1.1: Comparison of minimally invasive and open surgeries.

A minimally invasive procedure can be described by two phases in a time-line based analogy. These two phases include: pre-operative planning, which is performed prior to the surgery and intra-operative planning, which is executed during the surgery.

In the pre-operative phase, the objective is to create a patient specific plan for performing the surgery based on pre-operative patient data. There are several modalities for acquiring medical data of patients such as Computed Tomography (CT) and Magnetic Resonance Imaging (MRI). These modalities are used to visualize internal organs and structures such as bone and soft tissues. The acquired data is classified into anatomically meaningful structures. This process, called segmentation, generates 3D model of the organs and structures under surgery. Another part of the pre-operative planning is to incorporate soft tissue properties (for organs) through deformable models that can project and simulate deformations that naturally occur when interacting with that organ. In the intra-operative planning phase, first the coordinate system of the pre-operative 3D model is aligned with that of the

surgical site and then an interactive procedure is applied to provide the surgeon with accurate and adjustable visual feedback of the organs under surgery. This includes providing a suitable view of the organ for the surgeon by rotating and deforming the pre-operative 3D model. Figure 1.2 shows the rotation of a 3D model of the liver organ at six different angles. Such transformations enable the surgeon to view the organ from different aspects while performing the surgery.

The patient specific 3D model of the organ under surgery is generated by segmenting the organ from a set of medical images (bundled into a volume) that are acquired from various sensor modalities such as CT scans or MRI. The quality of these images could be affected by conditions such as non-uniform intensity distribution (both inside a single slice and across the volume), improper settings of the acquisition devices and noise. Techniques for image segmentation that rely only on low-level image information are usually dependent on the setting of parameters that compensate for such conditions and artifacts. Therefore, the performances of such methods are not as robust as required. Given the intricate anatomical structures, it is more logical to use prior knowledge of the organ than merely relying on low-level image content. In this sense, probabilistic model based segmentation techniques have been proposed to incorporate statistical knowledge of the organ as *a priori* in the segmentation and identification process. In this work, we propose a novel approach [5] that incorporates statistical information (acquired from a training dataset) as a mean of outcome quality and evaluation measure. Here a large number of possible segmentation outcomes are generated using a generic segmentation algorithm. A statistical model is then used to choose the candidate hypothesis with the highest fidelity to the organ's predetermined model (via training dataset).

In order to demonstrate the quality of segmentation achieved by the proposed approach, the proposed algorithms are tested for segmentation of liver and kidney from CT scan image volumes.

1.1 Contributions

In this work, two contributions toward the goal of organ segmentation from medical image data have been made:

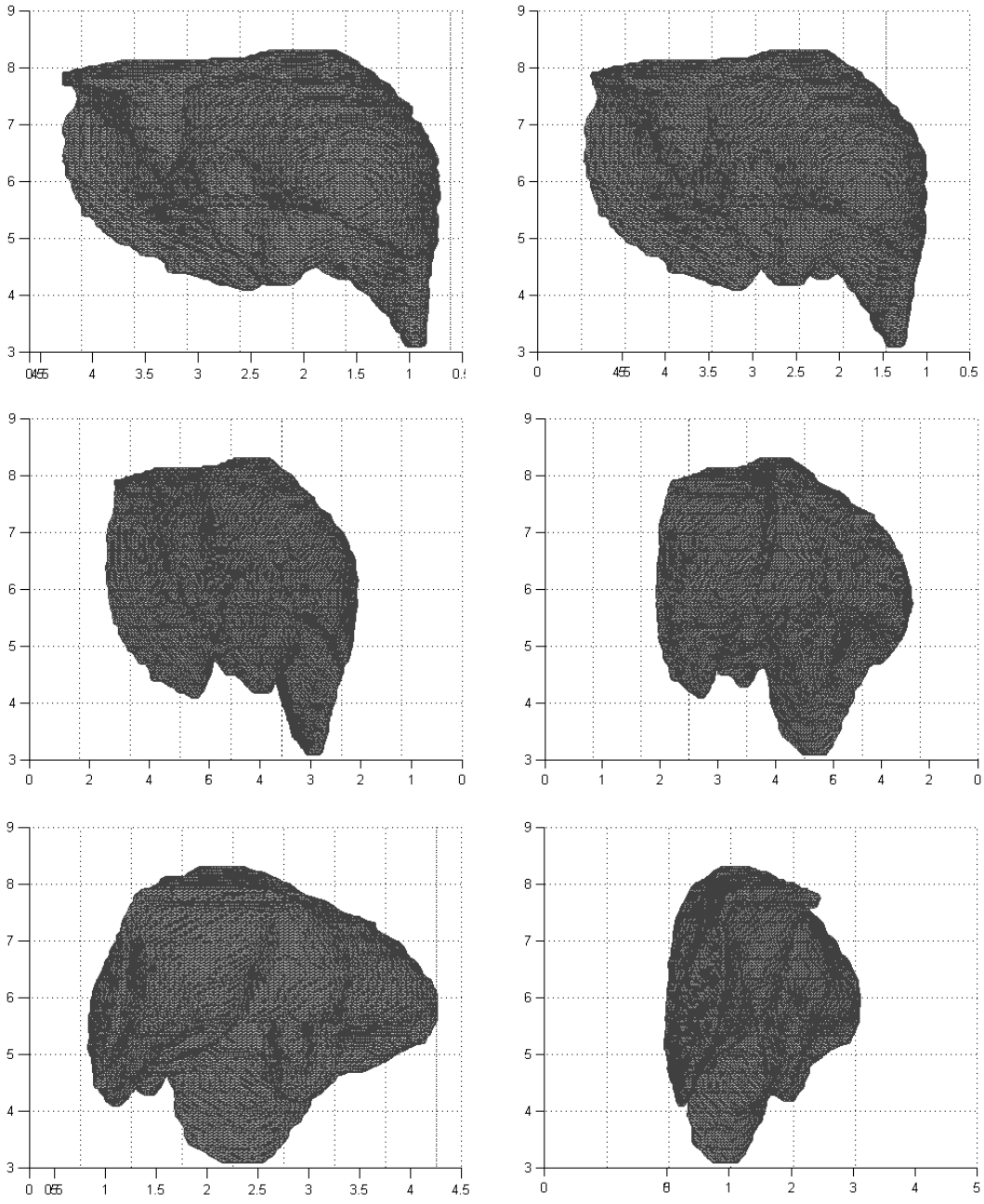

Figure 1.2: Rotation of the 3D organ model at six different angles. From left to right, top to bottom, the model is rotated 15 degrees clockwise

1. Presenting a novel approach that instead of leading the segmentation process towards results that are biased by the prior information, validates all potential unbiased segmentation outcomes according to the statistical characteristics of the organ.

2. Proposing a dynamic parameter setting scheme that allows automatic variation of segmentation quality control parameters at slice level and according to the fidelity of the generated output segments for that slice with the model.

1.2 Thesis Organization

The remainder of this thesis is divided into four chapters. Chapter 2 presents the state of the art in organ segmentation using medical image data and reviews several previous works in details. Chapter 3 describes the proposed approach for tackling the problem of organ segmentation. Experimental results are presented in Chapter 4 followed by the conclusions and discussion of potential future work in Chapter 5.

Chapter 2

State of the Art in Organ Segmentation

Segmentation of medical organs is defined as partitioning the image into connected regions that each correspond to a different organ. Such a task can be performed manually in software platforms with interactive cropping and editing capabilities. Pure manual segmentation proves to be problematic in medical applications, as volume datasets of images often include hundreds of samples. Overall, pure manual segmentation is a tedious, tiresome and time consuming process. A group of researchers have tried to reduce the amount of human interaction involved in the manual segmentation process by analyzing most of the data automatically while allowing user to manually edit and change the output results until satisfactory results achieved. These methods are generally referred to as interactive methods. All interactive methods incorporate human interaction to some level and therefore may still be slow or expensive. Also, the accuracy of these methods is dependent on the user's knowledge of the organ and therefore they require training of the user before the interaction. In order to address the above issues, algorithmic methods, which do not rely on user's interaction, have been proposed. These methods rely solely on image data and some knowledge of the organ. Here, image data is intensity level information of the voxels in a medical image volume and knowledge of the organ includes information such as organ's shape, position and size with respect to other structures or organs in the body. Algorithmic methods can be either fully automatic, where the user does not have any interaction with the system other than running it, or they can be semi-automatic, where the user has limited

and well defined tasks such as setting initial seed points for the segmentation.

The following discussion provides further details of algorithms that are developed for the application of medical organ segmentation. The use of interactive methods is explored first followed by the review of the algorithmic approaches.

2.1 Interactive Organ Segmentation

Interactive segmentation methods define segmentation as a process in which the user is provided with real-time feedback of the intermediate segmentation results. Here, the user is able to modify the segmentation results directly until acceptable results are obtained. Such algorithms are generally called user steered segmentation methods, since the user observes and verifies the segmentation results and explicitly steers the algorithm to a desired segmentation outcome. In the extreme case, the user performs the entire segmentation process manually. Most well known examples of these approaches are the family of livewire algorithms that are proposed for both 2D [6][7] and 3D [8][9] segmentations. These methods produce a piecewise optimal boundary representation of the object by viewing the image or the volume as a weighted graph and finding the shortest path between user specified boundary points. Most interactive segmentation methods are edge based. Here, user draws contours interactively to outline a region of interest in the image. The system computes the best path (sequence of pixels in the image) from the current identified position to the last clicked cursor point according to some energy function (usually using image gradient). A more recent example of this approach based on the concept of random walks is proposed in [10]. Here the image or the volume is considered as a weighted graph and the user marks a number of pixels per object and background. Every unclassified pixel is then labeled according to the probability value of a random walk, starting at the pixel's position and reaching to one of the user labeled pixels.

Another class of interactive segmentation methods such as Intelligent Paint [11] and Griffin's Hierarchical Segmentation [12] are region based. In these methods, the user is required to roughly indicate the location and region of the object and background by using strokes. In Intelligent Paint, the image is partitioned into small homogeneous regions using a watershed scheme. The user can click the mouse button to select a region where the growing process (paint flow) starts. In Griffin's Hierarchical Segmentation, seeds are marked on the image to impose hard constraints on the object and its background. The underlying

segmentation approach is then a hierarchical clustering technique. In their method, since the segmentation is only region based, there is no provision to smooth the boundaries or minimize their lengths. Graph Cuts [13][14] is another example of this group of approaches that utilizes the same framework as [12] but instead of hierarchical clustering, they use graph cuts. Here a graph is formed by connecting all pairs of neighboring image pixels. Certain pixels are used as priori information identifying object or background seeds. The objective is to cut the graph so that the object seeds are completely separated from the background seeds.

Depending on the amount of user interactions, interactive methods could often yield results that are as good as manual segmentation. However the user's interaction can be labor intensive for wide use in clinical settings given the continued growth in size and resolution of datasets. Despite the requirement for manual interaction, interactive methods are still proven to be practical for research purposes or a valid post processing approach where it is used to modify results obtained by automatic segmentation methods.

In order to overcome the intensity of labor use in interactive methods, algorithmic methods are proposed where no user interaction occurs during segmentation and the user's only task is to run the algorithm for different images or volumes.

2.2 Algorithmic Organ Segmentation

The vast majority of algorithms proposed for anatomical organ segmentation fall into the algorithmic segmentation category. These are methods where the user does not interfere with the segmentation process at all (automatic) or the user has only minimal amount of interference (semi-automatic). Automatic approaches are approaches where the user's job is only to run the program and wait for the results. In semi-automatic approaches the user's task includes minor initialization such as providing manually extracted starting points for segmentation process or manual setting of seed points. In these methods, the manual interference usually occurs before the segmentation process starts running. In this sense, semi-automatic approaches do not require real interaction with the user. Most of the algorithmic segmentation methods are automatic since tasks such as manual seed point extraction can usually be performed automatically by using unique characteristics from the structures and organs in human's body.

Both automatic and semi-automatic approaches include high and low-level algorithms

such as thresholding, edge detection, region identification, level-set, and deformable models. These methods can also include learning schemes to capture the characteristics of the organ in the form of a model, prior to segmentation. In this sense, the existing methods for 2D and 3D algorithmic segmentation of organs in medical applications using image processing can be divided into non-model and model based methods. Detailed review of each group is presented next.

2.2.1 Non-Model Based Techniques

Non-model based approaches generally rely on local image information such as texture, intensity, spatial correlation of the 2D organ images in consecutive slices, and the location of the organ in the body with respect to neighboring structures. The success of these methods depends on the ways they take advantage of the available local information. In this section a general review of these methods is provided. Many of these methods are developed for extracting kidney and liver in medical images.

The most general approach for extracting an organ from medical images is to treat this problem as a general pattern recognition problem. Here, texture based features are extracted from input images and the pixels are clustered according to their feature distances in a feature space. Therefore, based on the hypothesis that soft tissues can be discriminated using texture [15], texture information is used to segment organs in medical images. Susomboon *et al.* [16] propose an algorithm for pixel-level texture based classification in 2D segmentation of the liver in human abdomen. In [17], the previous algorithm is extended to segment the liver volume (in a slice by slice fashion) by calculating the texture at the pixel-level for each CT slice image. While this method utilizes several types of features to represent the liver's texture, it fails to produce good results on MICCAI's 2007 grand challenge database [18] [19]. Moreover it is computationally expensive. The failure is perhaps due to the fact that there is no organ shape model incorporated to compensate for variations of the texture and intensity values in different slices.

Since relying only on texture or intensity information will not provide satisfying results, organ specific information such as trajectory and location with respect to more identifiable structures such as spine and ribs are utilized. Seo *et al.* [20] propose a multi-modal threshold based method using piecewise linear interpolation that uses spine location as a reference point. Forouzan *et al.* [21] further improve their approach by taking the similarity of organ's data in consecutive slices of an image volume into consideration. In their approach, they

segment a 3D liver from a CT scan volume in a slice by slice fashion. The first slice is manually segmented (making this method a semi-automatic approach) and the rest of the slices are segmented based on a multi-layer thresholding technique using thresholds that are obtained by statistical analysis of the liver's pixels intensities, from the previously segmented slices. They also take advantage of the ribs location to achieve better segmentation results. Lin *et al.* [22] propose a method for kidney segmentation, in which the spine is used as landmark. They limit the processed image region to a region that contains the kidney using an elliptical shape that is localized according to the position and orientation of the spine in each image. After that, they segment the kidney based on an adaptive region growing. While [20] and [21] take advantage of the organ's relative position to the spine and ribs (easily and uniquely identifiable in medical images of abdominal area) they are still threshold based. Determining stable thresholds that perform robustly and consistently under different imaging conditions or variant intensity values (such as those in the MICCAI's dataset) is very difficult if not impossible. [22] reports good results based on Dice measure but since this method is based on region growing technique, it could be sensitive to the lighting conditions (as such conditions exist in 40% of the MICCAI's dataset volumes).

Active contours, snakes and level-set methods are also utilized in the field of organ segmentation. These methods are based on minimizing an energy formulation that consists of two terms: internal and external energies. The internal energy relates to the shape of the contour while the external energy is derived from the image data at locations related to the contour position itself. A minimized energy corresponds to contours with less stretching and bending. This means that the active contour method leads to segmentation results where the final segments have more natural shapes. Most of the active contour based methods are edge based and utilize information about the edges in the image into their external energy component. Chan and Vese [23] evolve the basic active contour methods to include statistical information about the region to be segmented. Pan and Dawant [24] incorporate a geometrical level-set method for automatic segmentation of the liver in abdominal CT scans that does not rely on prior knowledge of shape or size. Garamendi *et al.* [25] combine Chan and Vese method with a pre-processing step and apply it for segmentation of liver in CT scans. Linney *et al.* [26] improve the original active contour method by adding an inflationary force to the basic snake equation, and initializing the snake inside the liver. Wu and Sun report a deformable contour based method that includes texture classification and shape to identify kidney in ultrasound images [27]. Although these methods rely on model

based techniques that outperform threshold based techniques, none of them use organ's shape as prior knowledge. As a result, they perform relatively poorly in the cases where the organ includes tumors. Moreover, the methods in [24] and [25] are verified only on a very limited number of datasets. As for [27], the proposed work is tested and verified only on ultrasound images. Ultrasound images are essentially very different from CT and MRI images where the image contains other similar looking organs such as stomach in close vicinity of the left kidney.

Non-model based methods for organ segmentation are in general subject to inaccuracies due to variation in imaging condition, presence of tumor inside the organ, and noise. Relying on texture and image values can cause inaccuracies in the segmentation process as such features could change from one dataset to another. Moreover, most of these methods are parameter dependent and for the best performance, often these parameters require adjustment from one volume to another. Medical images could also be noisy, and usually contain more than one anatomical structure with small distances between organs such as the distance between liver and abdomen muscles or the distance between kidney and stomach. In addition, the organ boundaries may diffuse. To cope with these challenges, many algorithms incorporate domain specific prior knowledge. Such knowledge is often learned from a training set of data to form a specific understanding of the organ (usually in the form of a model).

2.2.2 Model Based Techniques

Incorporating anatomic knowledge into the segmentation introduces a more constrained framework which replaces the task of segmentation with registration of pre-segmented models to the test data. These models could be patient specific, atlas based, or statistical based. An interesting intrinsic characteristic of these approaches is that results are guaranteed to be topologically correct, assuming the model is not allowed to change its topology during the algorithm propagation.

In the most basic approach, the model is patient specific. Here, an instance of the anatomical structure is provided in one modality and the goal is to segment another instance of such structure in a different modality. In this process the model is registered with the target image or volume and the result of registration defines the segmentation output. In this approach, registration moves a known segmentation to another dataset. An example

of this approach is provided by [28], where a CT based vertebral model is registered to X-ray image. The tasks of segmentation and registration are coupled via an iterative scheme and segmentation results are ranked according to the registration results. An incremental registration update is computed based on the segmentation results.

An extension to this approach can be using a general atlas instead of a patient specific model. An atlas consists of a set of images or volumes and their segmentation results. This atlas is then registered to a new patient's data, producing a set of new segmentation results. As the model is generic, registering it to patient specific data requires the use of curved (deformable) transformations. While the combination of an atlas and curved transformations enables segmentation of structures that differ significantly from their atlas representation, it can also lead to erroneous results if the transformation parameters are unconstrained. This approach is mainly applied to segmentation of brain structures using different deformable registration techniques [29] [30] [31].

A more general mechanism for modeling an organ is to use statistical models of shape and appearance. Such statistical models are anatomy specific models that encode variations in shape and intensities as captured by a set of segmented training images. These methods aim to recover an organ based on statistical information. State of the art on model based segmentation are based on active shape models (ASM) [32][33] and active appearance models (AAM) [34]. Active shape and appearance models incorporate statistical or parametric shape models (from training data) in the actual segmentation process. ASM based methods model the shape of the object of interest while AAM based methods are a combined modeling of pixel intensities and object's shape. AAM methods are proven to be very robust and widely applicable to model objects within an image.

ASM and AAM are closely related to each other. It is argued that a disadvantage of ASM is that it only uses shape constraints (together with some information about the image structure near the landmarks), and does not take advantage of all the available information such as the texture across the target object. This disadvantage can be addressed using an AAM. However, in all the methods that utilize ASM for segmentation of a structure from medical image data, the texture and intensity information of the images are included into the main algorithm. Therefore, model based algorithms devised for medical image segmentation, whether they utilize ASM or AAM, they all take advantage of both shape and texture information.

Cootes *et al.* [32] describe ASM as point distribution models to construct statistical

models of general shapes from a training set. They exploit a linear formulation of the shape models to iteratively search for specific objects in the image. Kainmuller *et al.* [35] use ASM in combination with a model of the typical intensity distribution around the liver boundary and neighboring structures. The method in [36] incorporates statistical shape model in combination with an evolutionary algorithm to provide initialization for a deformable mesh that searches for human liver boundaries. Both of the two above methods perform a search strategy similar to ASM with an improved initialization step. Ling *et al.* [37] expand ASM by two new learning techniques including marginal space learning and steerable features that are accompanied by a new shape space initialization. They improve the original ASM by handling highly heterogeneous texture patterns. Wimmer proposes a new ASM [38] which is entirely built upon non-parametric estimates of probabilities. Spiegel *et al.* [39] apply non-rigid registration to remove the problem of establishing point correspondence among training data samples in ASM. Ali *et al.* [40] estimate kidney shape variations using a distance probabilistic model to approximate densities of kidney and its surroundings using Poisson distribution.

AAM based segmentation proves to be successful in face recognition (e.g. Cootes *et al.* [34]) and medical image segmentation (e.g. for 2D ultrasound sequences and 3D MRI [41]). Mitchell *et al.* [41] introduce the comprehensive design of a three-dimensional AAM as an evolved extension of the AAM framework introduced by Cootes *et al.* [34] where they utilize this method for segmentation of cardiac ultrasound images and MRI volumes. Stegmann *et al.* [42] summarize AAM applications in medicine and describe a public domain implementation. They improve the performance and make more general models by applying parallel analysis to obtain objective model truncation. Mitchell *et al.* [43] combine AAM and ASM in a novel multistage hybrid appearance model methodology that avoids local minima of the matching function.

Algorithms proposed in [35]-[43] are all variations of the original methods by Cootes *et al.* [32][33][34], where the shape and texture model of the organ are utilized as *a priori* to lead the segmentation algorithms towards better results. All of these methods suggest improvements over the original approach either by improving the complexity and time or simplification of the required steps for constructing the model.

The main advantages of the model based techniques are accuracy and robustness. They are also capable of compensating for the missing image features via interpolation. The performances of these methods however are dependent on the number and the type of the

training data. Also, if the shape to be segmented lies too far away from the model space, it may not be reachable even by those better methods that incorporate free-form deformation and statistical models. Therefore, for some test volumes and organs, due to diversity in shape and size, the performance of model based approaches can vary. Also, all model based organ segmentation techniques, proposed up to now, have utilized statistical information of the organs as *a priori* in their main segmentation scheme. In general, in these methods both shape and intensity variations are constrained to the sub-space defined by the modes of variation computed from the training set. This is both beneficial and detrimental. It is beneficial, as the training set enforces reasonable constraints on possible object appearance. It is detrimental if the constraints are too limiting.

2.3 Proposed Algorithmic Model Based Technique

As described in the previous sections, interactive techniques present very good results but they are time consuming and labor intensive. Therefore they are not the best choice for applications in clinical settings where large datasets are required to be segmented. Algorithmic techniques, however, do not require interaction with the user and are often performed fully automatic with no or minimum user interference. Among algorithmic methods, non-model based techniques (merely based on low-level image processing techniques) suffer from inaccuracies in segmentation due to their incompatibilities to cope with different imaging conditions and similarity of color and texture between neighboring organs. Therefore, the most adopted approach for segmentation of organs in medical images are model based techniques, where prior information of the organ is included to guide the underlying segmentation technique towards better results. In these techniques however, shape variations are limited by the model generated from prior information of the organ.

In this work, we propose a novel alternative approach for utilizing statistical model information in an identification phase that is devised to choose the best segmentation candidates according to its distance from an organ's model space. Here, first a general segmentation algorithm that covers all segmentation results from under to over segmentation is utilized. After generating a set of segmentation hypotheses, a statistical model, based on Principal Component Analysis (PCA), is used to generate an organ space. The distance of each candidate segmentation hypothesis from the organ space is measured to choose the closest

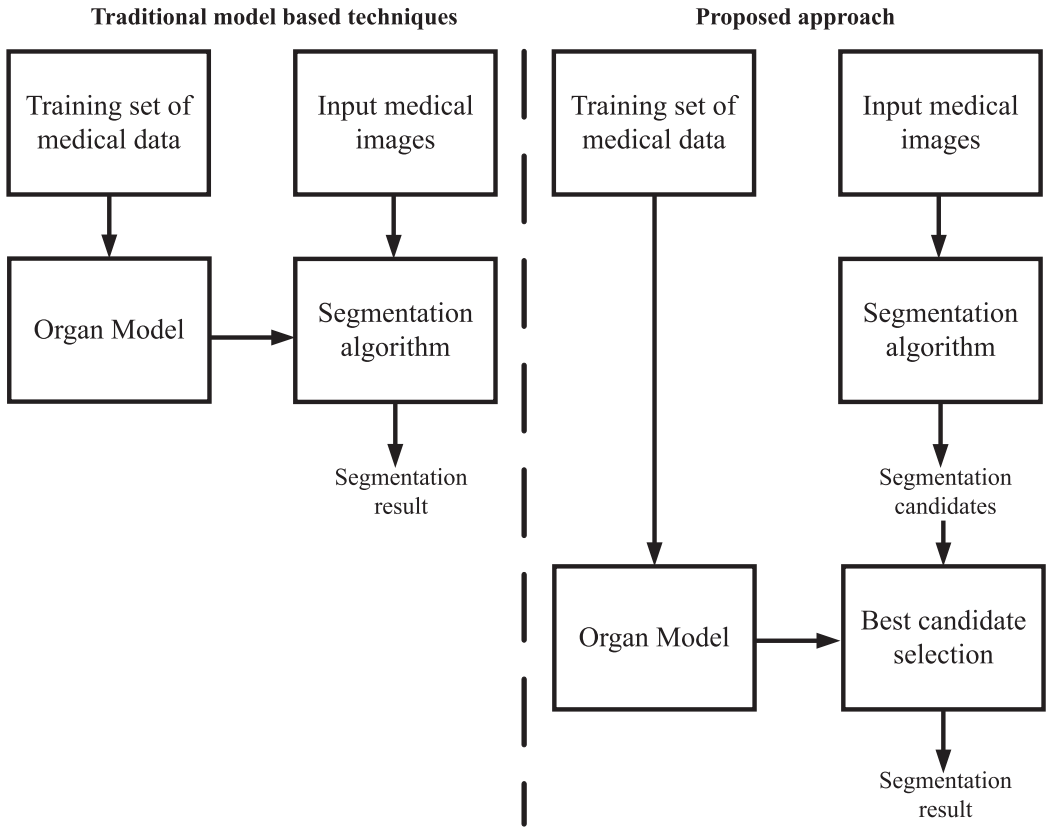

Figure 2.1: Comparison of the traditional model based techniques with the proposed method.

candidate as the best segmentation result. Here, the organ space information utilized independently from the segmentation algorithm and therefore it does not constrain the shape variations that can be generated by the segmentation algorithm. Figure 2.1 shows and compares the flowcharts of the traditional model based approaches with that of the work proposed in this thesis.

Chapter 3

Proposed Algorithmic Approaches

In this chapter, two algorithmic solutions for performing organ segmentation on medical volumes are presented. In the first approach, the input to our algorithm is a CT scan volume of abdominal area and the output is the segmentation of a specific organ within the input volume. In the second solution, in addition to the input CT scan volumes, a number of training volumes for which the organ of interest is manually segmented is provided to the system as inputs. The first proposed solution is tested and verified on liver while the second solution is tested and verified on both liver and kidney organs in the CT volumes data.

In order to perform segmentation in the input CT scan volume, originally a semi-automatic method based on DEformable Registration and Multi-layer Segmentation (DERMS) is proposed [44]. DERMS is a non-model based approach that relies on two types of information: organs shape similarity in consecutive slices and its image intensity characteristics. Here the organ shape information is retained by measuring the shape similarities between consecutive slices in CT scan volumes. This is performed through a deformable registration scheme. The organ intensity is utilized by a multi-layer image segmentation algorithm that emphasizes on the true boundaries of the organ. Such multi-layer technique utilizes any generic segmentation approach as its core part (here mean shift segmentation [45] has been utilized). DERMS requires manual setting of a seed point for the segmentation process and therefore it is categorized as a semi-automatic method. DERMS has been applied for segmentation of liver on CT scan volumes and it is able to deliver satisfactory results only for some of the input dataset volumes. The main setback of DERMS is the use of fixed thresholds in the segmentation process.

DERMS was improved by including a model, representing a space for the organ of interest. Such space was reconstructed by applying PCA over a training set of CT scan volumes. The mission of this model is to dynamically set the fixed threshold applied in DERMS. Also by including a pre-processing stage, the need for manual setting of the seed point was removed hence achieving a fully automatic method. Here the model information is used to perform validation for segmentation candidates generated using a generic segmentation approach (such as mean shift segmentation [45] and graph based segmentation [46]). Generation of segment candidates in this method is similar to DERMS as the same multi-layer segmentation scheme is applied to generate different segmentation candidates. This method is called: Model based Validation Scheme (MOVS). MOVS is tested for segmentation of both liver and kidney from CT scan volumes of MICCAI's 2007 grand challenge workshop. The results for these segmentations proved satisfactory for all the volumes.

In the following sections, at first the strategic planning for performing segmentation are discussed. This discussion includes the introduction of utilized dataset and visualization tool. DERMS is presented in the second section and its shortcomings are discussed. The third section discusses our model based solution to the problem of organ segmentation (MOVS). Finally, in the last two sections of this chapter, the application of MOVS for segmentation of liver and kidney in CT scan volumes are presented.

3.1 Strategic Planning

This section describes the datasets used as well as visualization techniques that are incorporated to depict 3D segmentation results.

3.1.1 The Employed Dataset: MICCAI's 2007 Grand Challenge Workshop

The MICCAI's 2007 grand challenge workshop dataset is utilized for testing of the proposed algorithm. This dataset was prepared for a competition started as part of the workshop 3D Segmentation in the Clinic: A Grand Challenge, on October 29, 2007 in conjunction with MICCAI 2007. This competition was designed for segmentation of human caudate and liver organs with separate datasets provided for each organ. Teams that participated in the liver segmentation contest downloaded training and test datasets and submitted the results of their algorithms on the test data to the workshop organizers for final evaluation.

Figure 3.1: Example of iodine based contrast in cerebral angiography, source: Wikipedia.org.

A total of 30 volumes are available in this dataset. Most of them are pathologic and include tumors, metastasis and cysts in different sizes and at different locations. Volumes have been categorized into two groups: 20 training, 10 testing. The ground truth for this dataset was created manually by radiological experts, working slice-by-slice in transverse view. Only the ground truth for the training set is provided to the contestants while the organizers use the undisclosed ground truth of the test data for evaluation purposes.

All CT images were enhanced with contrast agent. Contrast agent or medium is a substance used to enhance the contrast of structures or fluids within the body in medical imaging. Iodine and barium are the most common types of contrast medium for enhancing CT based imaging methods. Figure 3.1 shows an example of iodine based contrast in cerebral angiography.

The CT images are scanned in the central venous phase on a variety of scanners (different manufacturers, 4, 16 and 64 detector rows). The task of the detector rows of the scanner is to measure the attenuation of the X-ray beams (generated from a source positioned across the detectors) that pass through the body. The detected beam attenuation is then translated into intensity profile and generates the CT images. [47] provides a complete description on the fundamentals and functionality of CT scanners.

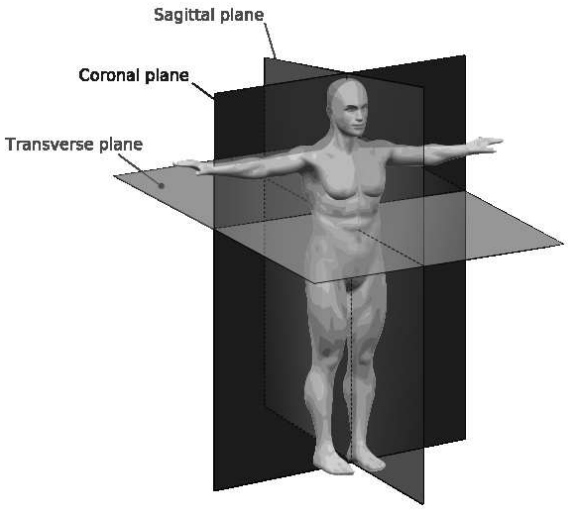

Figure 3.2: Human anatomy planes, source: Wikipedia.org.

Same as any CT data volume, all datasets have been acquired in transverse direction. All the images of the volume in the transverse direction are 512 by 512 and the inter-slice distances vary from $0.7mm$ to $5mm$. There is no overlap between consecutive slices. All the data is stored in Meta format containing an ASCII readable header and a separate raw image data file. In this work a simple MATLAB code is used to open and read each of the volumes according to its corresponding header information. Each volume is read into a 3D data array that can be observed in any of the three dimensions. Therefore, 2D images of each volume can be generated in transverse, sagittal, and coronal planes directions. Figure 3.2 shows these three planes on a human body. Figure 3.3 describes three sample slices from the three different directions extracted from one volume data of the dataset.

3.1.2 The Employed Visualization Technique: Marching Cubes

In this section the Marching cubes [48] algorithm, used for representing a 3D triangular mesh from a set of points in 3D space, is presented. Marching cubes is a computer graphics algorithm that estimates a polygonal mesh, representing a surface, from a scalar field in 3D space.

The scalar field in this approach is the points of the organ boundary segmented from an image volume. Each boundary point in the space is assigned the value '1' and any other point is assigned the value '0'. Next, the space is partitioned into connected cubes so that

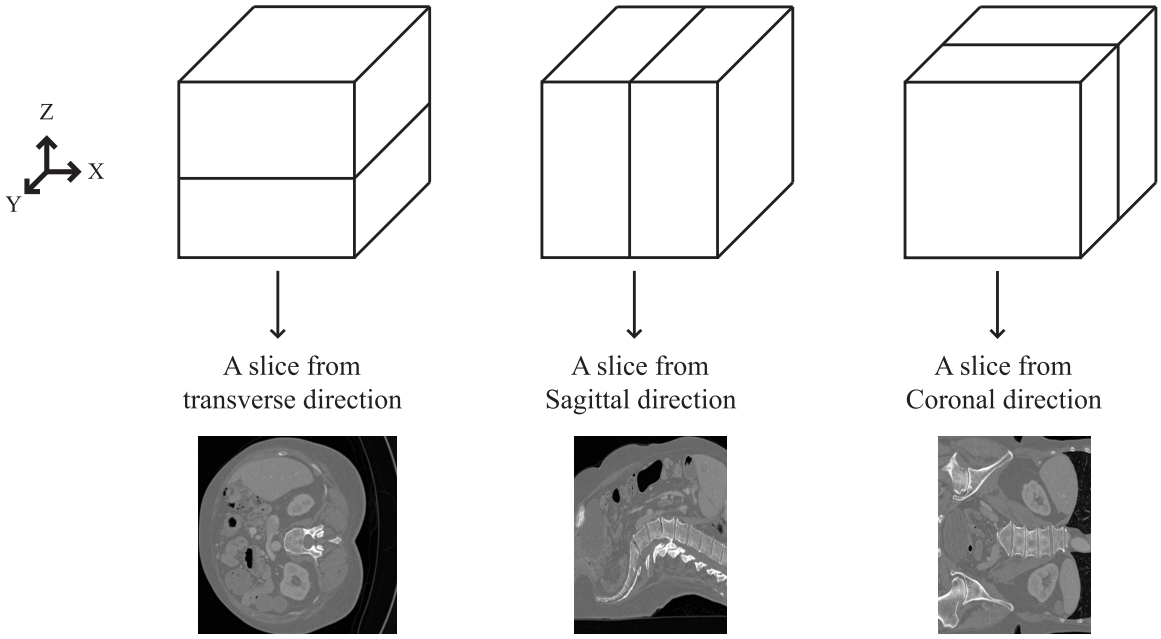

Figure 3.3: A CT scan volume from abdominal area with sample slices extracted from all three directions.

each cube vertex is assigned either the value '1' or '0' according to the scalar field. Here, the assumption is that the goal surface intersects only the cube edges with one vertex with value '1' and one vertex with value '0'. This is because the '1' values represent the boundary points that are located on the surface. By this assumption the topology of the surface inside each cube can be determined (called triangulation of the cube). Using this, an individual set of polygons will be created for each cube and fusing these polygons from neighboring cubes together results in the desired surface.

For triangulation of each cube, an index to a pre-calculated array of 256 possible polygon configurations ($2^8 = 256$) is created within the cube. This is performed by treating the value of each vertex ('1' or '0') as a bit in an 8-bit integer. Therefore each cube has a value between 0 and 255 that is the index to a precalculated polygon configuration. The precalculated polygon configuration has 256 cube configurations which can be obtained by reflections and symmetrical rotations of 15 unique cases. These cases are shown in Figure 3.4.

By visiting all the cubes, all the vertices and their connectivity (triangles) are computed and therefore a mesh is reconstructed. Figure 3.5 shows an example 3D mesh of a liver constructed using marching cubes.

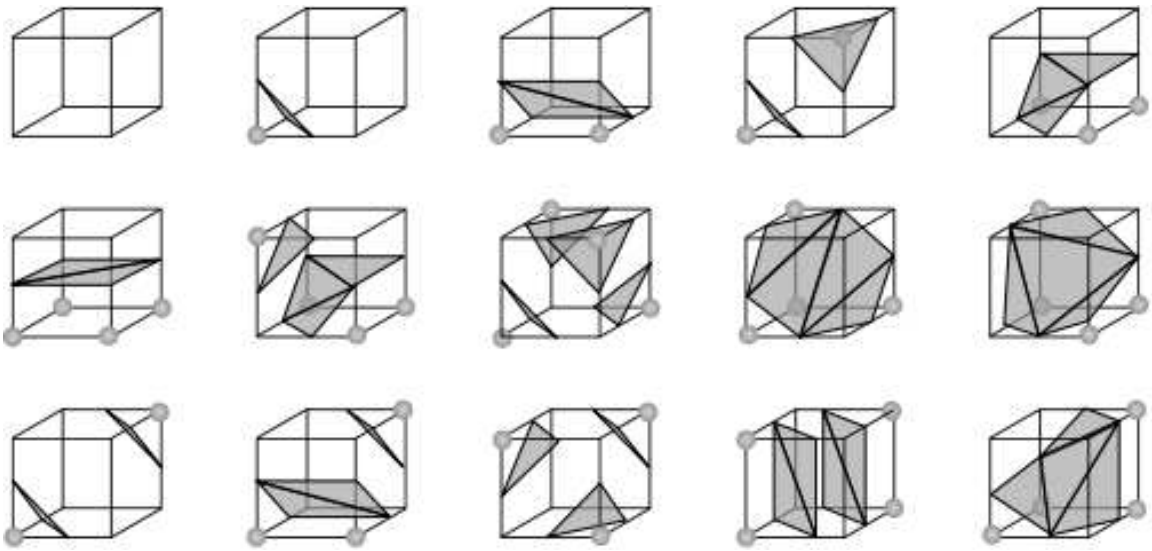

Figure 3.4: Triangulated cubes, source: Wikipedia.org.

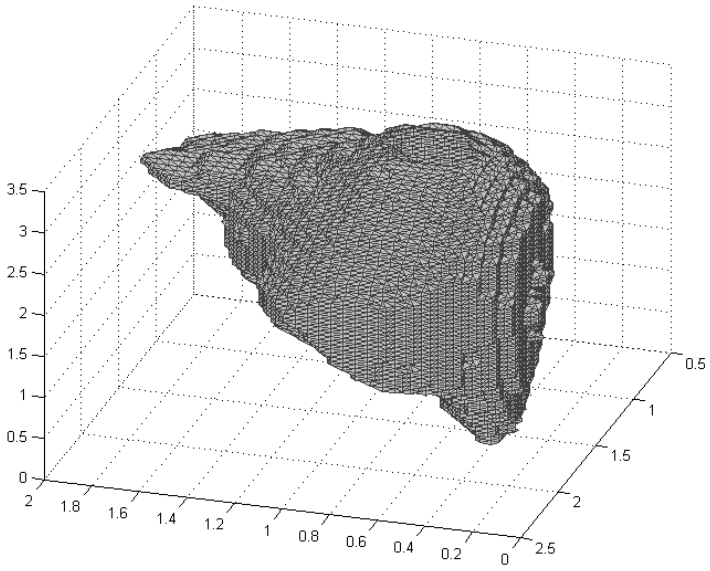

Figure 3.5: 3D mesh of a sample extracted liver.

3.2 DERMS: Deformable Registration and Multi-Layer Segmentation Method

In this section an algorithm is proposed that does not rely on training data but rather relies on the intensity of organ slices in a CT scan volume and shape similarities of the organ in every two consecutive slices in the transverse direction. Here, organ shape similarity in consecutive slices are measured by deformable registration. Also the algorithm incorporates a multi-layer segmentation that focuses on true boundaries of the organ regions. Therefore the algorithm is a combination of DEformable Registration and Multi-layer Segmentation (DERMS). This algorithm has been applied on segmentation of liver from CT scan volumes. Therefore, without loss of generality, the algorithm is described based on its application on the liver while the same procedure can be applied over any other organ.

The algorithm starts from one of the middle slices in the transverse direction whose liver mask is provided in the input set. This middle slice is usually selected from the regions of the abdominal area where the liver area is at its largest. The algorithm processes the input slices in two batches. Both two batches start from the middle slice but one moves in the proximal direction towards the head and the other in the direction towards the feet. In every step, the liver mask of the previous step's slice (slice number $i-1$) is manipulated to form the liver mask for current slice (slice number i). Such order in processing is held until the last slice in each proximal direction is visited and its liver mask extracted.

There are three stages in extracting the 2D liver from every slice in the transverse direction. The first stage provides a rough estimation (we refer to this as guesstimate) of the liver mask for slice number i using the deformation field from deformable registration. The second stage utilizes mean shift segmentation [45] to estimate the liver regions around the rough estimation of the first stage. At the third and last stage, all the extra regions that might have been wrongfully added to liver mask guesstimate are removed by taking advantage of a multi-layer segmentation based on mean shift segmentation. Figure 3.6 displays the main stream of operations for the proposed method. Details of each process are described next.

3.2.1 Stage 1: Deformable Registration

In this stage, shape changes are estimated and tracked from image slice $i-1$ to image slice i. These changes are then applied on the liver mask of slice $i-1$ to form a guesstimate of

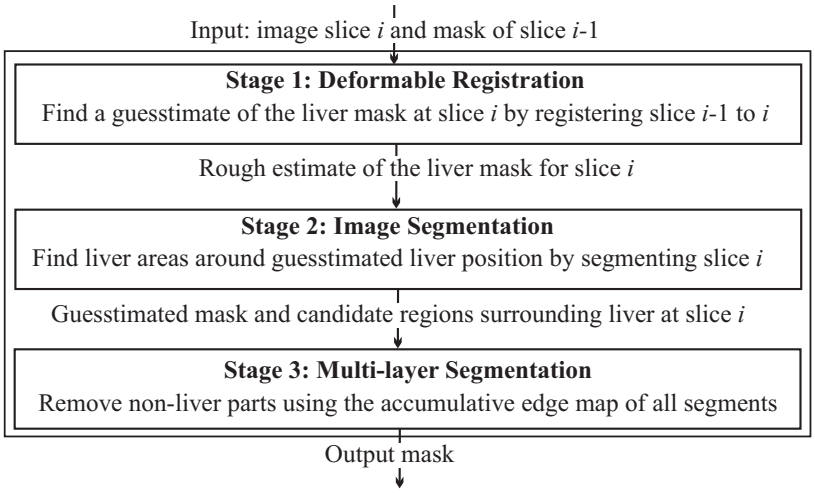

Figure 3.6: Order of operations for slice i in DERMS method.

liver mask for slice i. This operation is performed as following:

1. The image of the slice $i-1$ is registered with the image of slice i. Registration is performed using Drop software, which registers using non-rigid registration based on discrete labeling and linear programming [49, 50]. Here the output is a deformation field.

2. The estimated deformation field projects mask points of slice $i-1$ onto their new locations at slice i. Since the transformation transfers integer locations to non-integer locations, the nearest neighbor scheme is used to estimate new transformed locations.

3. The rounding error from nearest neighbor scheme manifests itself by a number of scattered undefined/hollow points inside new masks. A morphological closing is applied to close hollow points on the new mask.

Due to the fact that often each liver dataset contains sudden and large changes including additive connected or isolated pieces from one slice to the next, the results of this operation cannot account for all changes that exist between two consecutive slices. Hence, these results are basically a rough estimate of the liver's profile at slice i, which might not necessarily cover the entire actual liver region or might include regions from neighboring organs. Figure 3.7-a shows the initial mask for slice $i-1$. The result of stage 1 for a typical case is shown in

Figure3.7-b. The rest of the images in Figure3.7 depict intermediate results of other stages and the final result of segmentation.

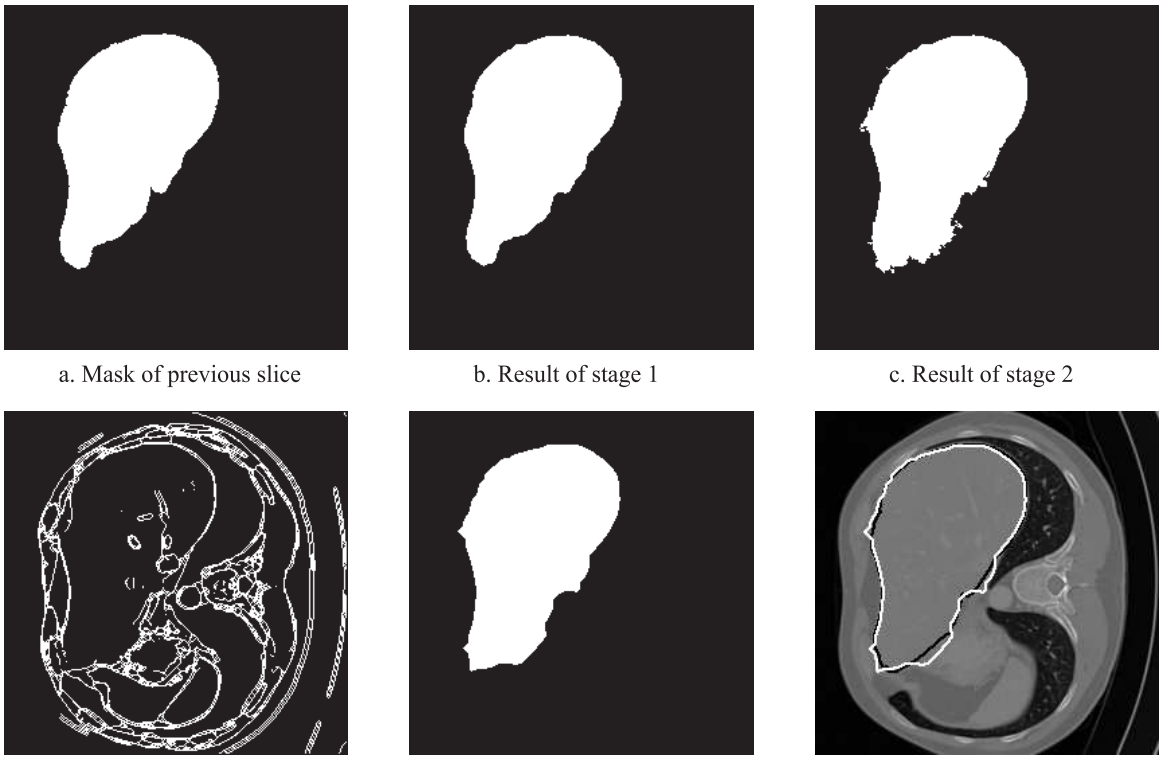

a. Mask of previous slice b. Result of stage 1 c. Result of stage 2

d. Enhanced Edge Map e. Result of stage 3 f. Comparison with ground truth

Figure 3.7: Intermediate image results at different stages.

3.2.2 Stage 2: Image Segmentation

After estimating a guesstimate of the liver mask at slice i, the algorithm inspects those regions that are newly appeared in the slice i compared to slice $i-1$. For this, first the liver image is segmented using the mean shift segmentation algorithm. Mean shift segmentation algorithm controls the quality of segments through three parameters of intensity (h_r) and spatial (h_s) resolutions, and minimum segment size. For a segmentation that leads to segments with texture similarity, regardless of the regions' nose level, typical values of 7,6.5, and 20 are chosen for h_r, h_s, and minimum segment size respectively.

Using results of the segmentation, all image regions that are physically connected to each other and have overlaps with the mask guesstimate of the liver at slice i, are connected

together to generate an updated liver mask region. This step is intended for identifying and admitting all liver regions that just appeared in slice i and were not present in slice $i-1$. It must be noted that, organs and tissues in close proximity of the liver with similar textures to the liver could be wrongly added to the liver mask at this stage. A typical result for this stage is shown in Figure 3.7-c.

3.2.3 Stage 3: Multi-layer Segmentation

This stage removes those regions that were wrongly identified as liver and added to the mask. For this purpose, a boundary that surrounds the liver region at slice i is required. To estimate such boundary an edge map that contains all edges of the liver is utilized using a multi-layer segmentation technique. In this technique the image of slice i is segmented with the mean shift algorithm several times using a range of parameters. The ranges for intensity and spatial resolutions are: $h_r \in [1:2:27]$ and $h_s \in [1:2:15]$ and minimum segment size was kept fixed at 20 pixels. These ranges were chosen according to simulation results over several input images. Details of this simulation is presented in Section 3.5.

After performing the segmentation several times with the aforementioned ranges, the boundary edges of all segmented slices are then extracted. The extracted edges are added together to form an Accumulative Edge Map (AEM). The AEM highlights more dominant edges such as liver external boundaries which are less sensitive to the parameter setting of the segmentation algorithm. The contrast of AEM is enhanced using Log transform [51] in order to attain more emphasis on the edges of the image. Figure 3.8 shows the (AEM) and enhanced (AEM) for a sample slice.

Figure 3.8: Left: sample slice, Middle: AEM, Right: enhanced AEM.

The enhanced AEM is thresholded (computed automatically) to form an Enhanced Edge Map (EEM) that contains only liver's boundary edges. If the edge map of a segmented image is called $EMSI$ and s represents the segmentation parameters for the mean shift algorithm, the above operation can be described by:

$$AEM = \sum_{s} EMSI \tag{3.1}$$

$$EEM(x,y) = \begin{cases} 1 & Log(AEM(x,y)) > Thresh \\ 0 & \text{otherwise} \end{cases} \tag{3.2}$$
$$\text{Where:} \quad Thresh = \frac{max(Log(AEM)) - min(Log(AEM))}{2}$$

A sample result for generating the EEM is shown in Figure 3.7-d. EEM is then subtracted from the output of segmentation operation at Stage 2 (Figure 3.7-c) to separate the liver from non-liver regions. The result for this stage is shown in Figure 3.7-e. The results of proposed method and the manual extraction are overlaid on a sample slice as shown in Figure 3.7-f. The black contours in this image shows the ground truth segmentation while the white contours represents the results of DERMS.

3.2.4 Refinement of Non-single Piece Liver Masks

Due to anatomical features of the liver, often its cross sections consist of two or more pieces. When processing such slices, the proposed algorithm creates only a one-piece mask for the largest piece of the liver. In order to identify and add the missing pieces of the liver to the mask, a supplementary process is designed. In the supplementary process, the system first returns to the starting slice (middle slice, say index $i-1$). The liver mask for this slice will be transformed onto the slice i using the deformable transformation scheme proposed in Stage 1. Comparing results of this transformation with the actual mask of slice i (found by running Stages 1 to 3) the algorithm determines whether there is any large piece of the expected mask missing. If not, the supplementary process moves to the slice i and uses its mask as the ground truth for slice $i+1$. If however one or more pieces of the expected mask are missing, the algorithm creates the guesstimates of the missing mask pieces (through subtraction) in slice i. The following two conditions must be satisfied for a secondary piece to be examined as a potential missing mask piece.

1. It had been part of liver mask in slice $i-1$, and

2. Its area must be at least 10% (an empirical threshold) of the previously calculated mask area at slice i.

The mask identification process (Stages 2 to 3) then will be applied to all extra pieces that have satisfied the above two conditions to fine estimate each mask. Once all pieces are estimated, they will be added to the mask of slice i and the process continues by finding all secondary pieces of slice $i + 1$ using the updated mask of slice i as the ground truth. This process is performed for all slices of the volume in two batches on the two sides of the middle slice.

Some results are shown in Figure 3.9. Figures 3.9-a and -b display results for non-single pieces and 3.9-c and 3.9-d for dark slices. Figures 3.9-h and 3.9-i depict examples of bad segmentation. This algorithm is not performing perfectly for all the input cases. Although no algorithm is perfect, there is always room for improvement.

3.2.5 Discussion on DERMS

In order to evaluate the results of the proposed method, the datasets and evaluation metrics from MICCAI 2007 grand challenge workshop [18] are adopted. As mentioned before, the dataset includes 20 training and 10 test volumes. The results for the test volumes are shown in Table 4.3. The definition of the metrics used in this table are explained in Section 4.2.

The results show an overall improvement over some similar non-model based techniques ([17] [21]) that rely on liver texture and similarity of liver shape in consecutive slices. As shown in this table, good results have been obtained for only 70% of the datasets and estimates for the remaining 30% volumes (numbers 3, 5 and 10) are really bad. This is mainly due to the fact that a fixed threshold was applied for all volumes in multi-layer segmentation (in Equation 3.2). The next approach is proposed to improve the performance of DERMS.

3.3 MOVS: Model Based Validation Scheme

In this section, a general model based validation and segmentation scheme (called MOVS) is introduced. In a unique way, this method chooses appropriate segmentation parameters dynamically and according to specific characteristics of the slice/volume dataset. Such parameters were fixed for our previously proposed approach. Also in this method, the need

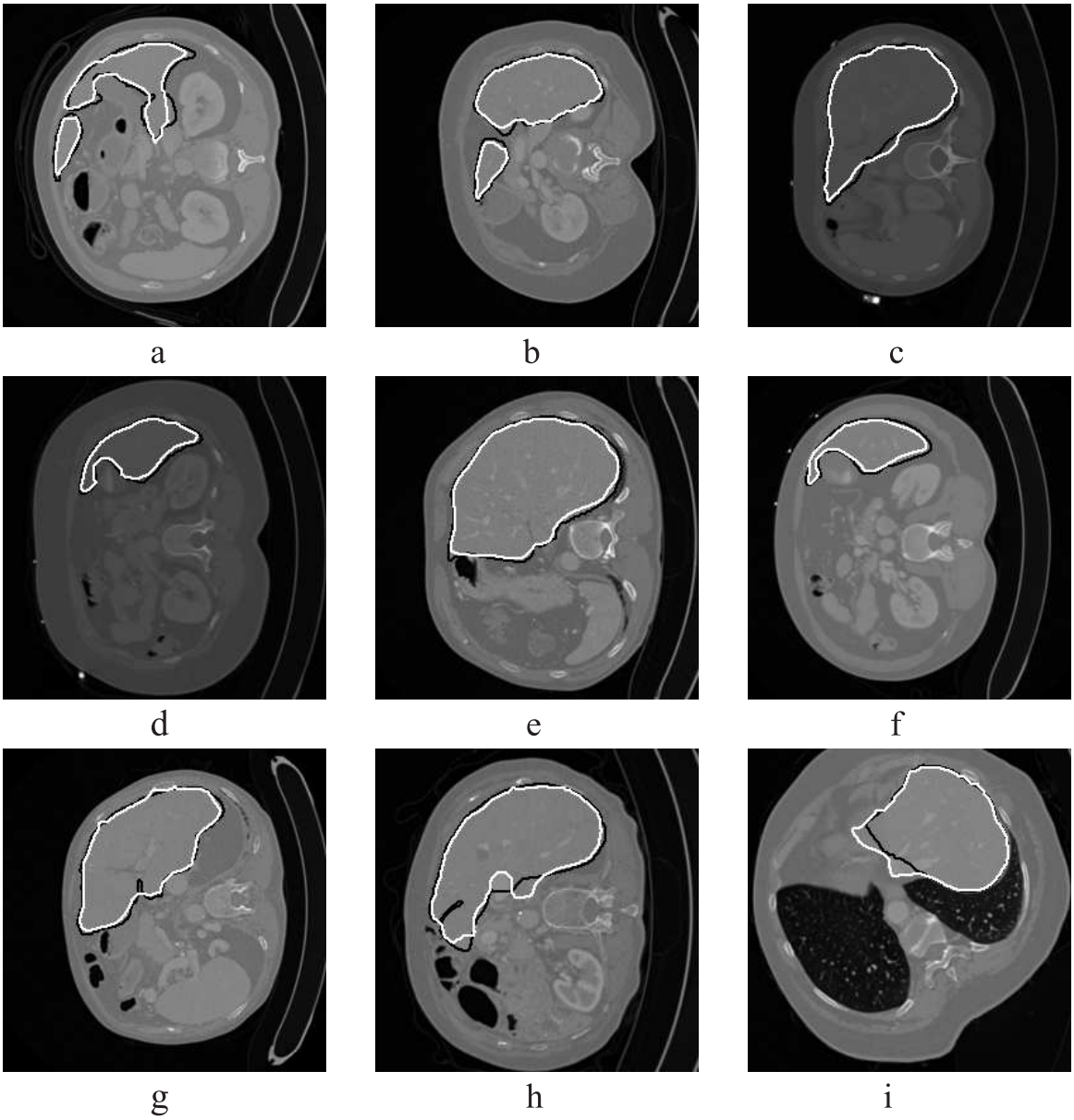

Figure 3.9: Sample results from the training volumes of MICCAI 2007 dataset (black: ground truth, white: boundaries by the proposed algorithm).

for inclusion of the manually extracted mask of the dataset's middle slice is eliminated by including structural information from the anatomy of human body and the region of interest. Therefore MOVS is a fully automatic algorithm.

In MOVS instead of using the model information to direct the segmentation algorithm towards segmenting an organ in an image, the model information is used to choose a segment (among all possible segmentation outcomes) with the highest fidelity to the organ. The data flow diagram for this work is depicted in Figure 3.10.

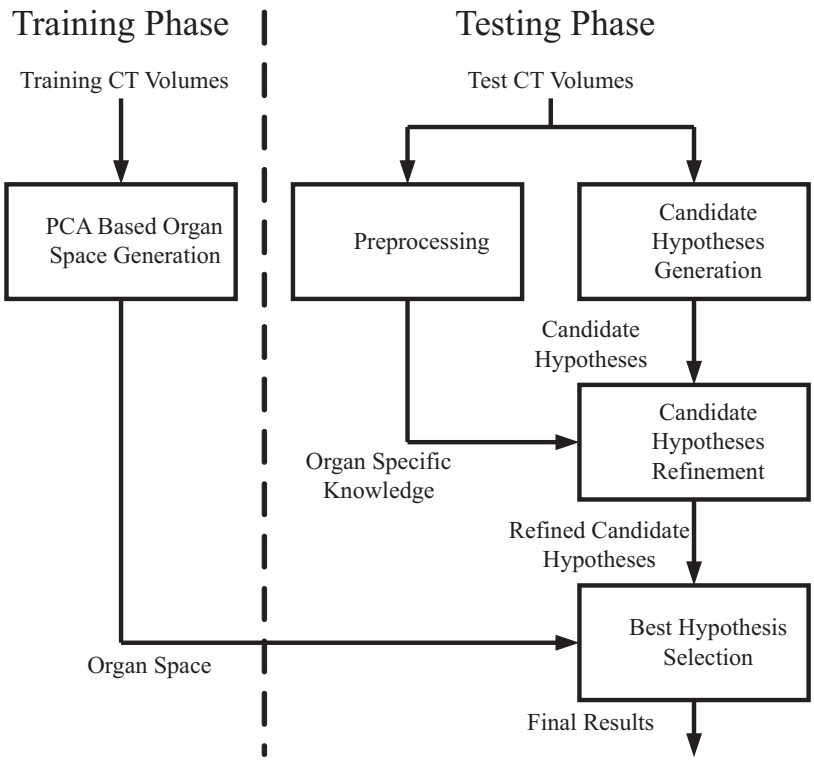

Figure 3.10: Flow diagram of the proposed method (MOVS).

The algorithm includes two phases of training and testing. In the training phase, using the ground truth provided by the training dataset, an eigen space is constructed that describes the organ (this space is referred to as the organ space). The organ space is a group of eigenvectors that are generated by applying PCA over the ground truth of the training dataset. In the testing phase, unknown CT volumes are processed to segment the organ of interest. The testing phase includes four main procedures:

1. Pre-processing: This procedure includes an alignment process, in which the orientation of the CT volumes are automatically estimated and corrected to a reference orientation. It is also responsible for establishing a starting point within the volume under process. This starting point relies on unique characteristics of the organ of interest and the general knowledge of the organ (such as its trajectory and physiological attributes) that occurs at a specific location within the volume.

2. Candidate Hypotheses Generation: This procedure segments each image slice into a very large number of overlapping regions (each with a unique property) among which one region could potentially be the true region corresponding to the organ of interest on that specific slice.

3. Candidate Hypotheses Refinement: This procedure reduces the search space (candidate hypotheses) by imposing constraints that incorporate temporal relationships between organ's regions in consecutive slices of the CT volumes.

4. Best Hypothesis Selection: This procedure measures the quality of all generated candidate hypotheses (after step 3) according to the organ space generated in the training phase and identifies the best candidate.

In the following subsections, details of the training and testing procedures are described.

3.3.1 Training Phase: PCA Based Model Generation

The objective of this section is to create a vector space that represents an organ. Such space is a model that encapsulates the variations of the organ according to the training set volumes. In general an organ space can be created using boundaries, masks or image regions of the organ of interest in CT images. Such information is used to either create masks for the organ or extract the cropped image of the organ from the CT scan data to create the organ space. The space can also be created for 2D images/masks of the organ or 3D volumes of images/masks of the organ. Therefore the input data to this module could be 2D or 3D vector data of organ's mask or cropped image.

In this work, we have used different sets of information for the applications of the proposed method. In Section 3.4, 3D kidney organ reconstruction, we have incorporated the cropped images of the kidney region in each training dataset volume. In Section 3.5, where the application of the proposed method for construction of 3D liver models is presented, the

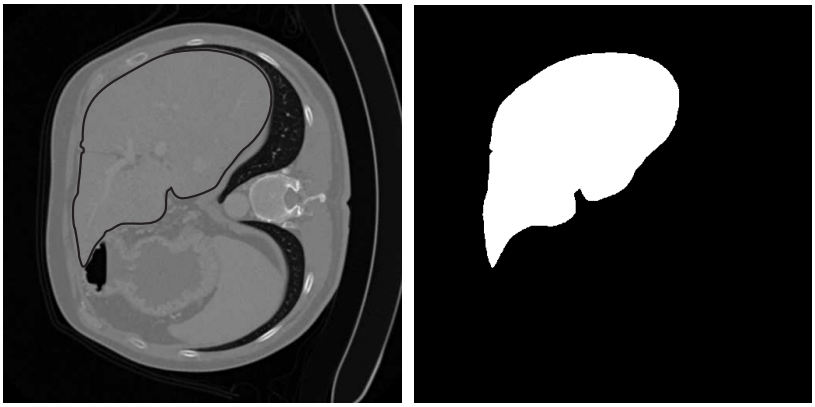

Figure 3.11: Image of the abdominal area with its corresponding 2D liver region boundaries (identified in black, left) along with its corresponding liver mask area (right).

3D liver masks from the training datasets are used for creating the organ space. Figure 3.11 shows image slice of the abdominal area with its 2D mask and the extracted liver's image region. Figure 3.12 shows how 2D extracted masks of the liver in the CT slices are piled up together to generate the 3D liver.

One approach to create an organ space that encodes variations of an organ in a series of training data is to find the principal components of the distribution of the training set. This is equivalent to computing the eigenvectors of the covariance matrix of the set of vector data. Each input vector contributes more or less to each eigenvector. Each eigenvector looks like a ghostly organ mask or image depending on the input type. The eigenvectors form a space that represents the organ where each new organ vector data can be approximated using a linear combination of these eigenvectors. Here, without loss of generality, we explain the generation of the model for one training set of 3D input vectors. Note that these vectors can contain either image pixels or binary mask values.

All the volumes in the training set of MICCAI's 2007 grand challenge workshop have the same size in sagittal (X) and coronal (Y) directions (512×512 pixels) but the sampling in the transverse (Z) direction is not the same and therefore each volume has a different number of slices. Also the thickness of each volume is different and varies between $138mm$ to $213mm$ with a mean of $175mm$. In this work, all the volumes used in the training set for generating the PCA based model are re-sampled in the transverse direction to the same number of slices (100 for each volume).

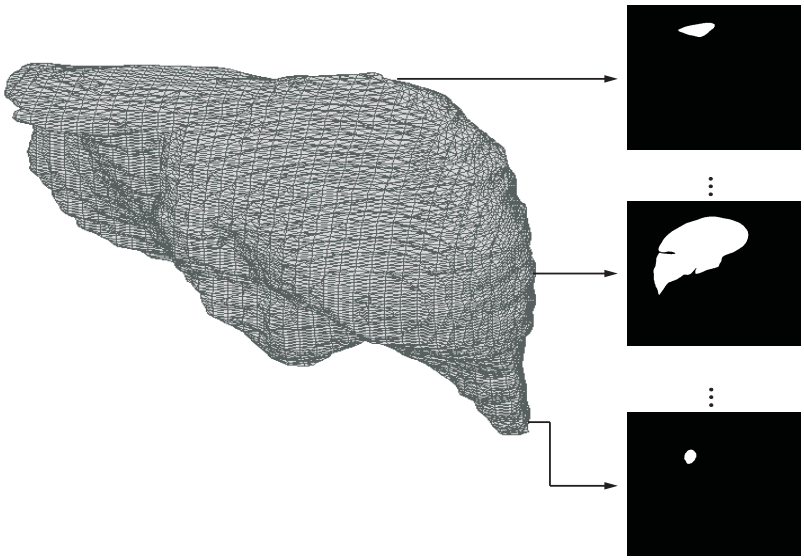

Figure 3.12: A 3D liver volume and it's corresponding 2D liver masks.

We assume that each 3D input vector in the training set is a 3D array of X by Y by Z or equivalently a 1D vector of size $X{\cdot}Y{\cdot}Z$. If L_1, L_2,..., L_n are 1D vectors of the training set and ψ is their mean, the distance of each vector from its mean is defined by $\phi_i = L_i$ - ψ. Here, we look for the set of n orthonormal vectors u_i that best describe the distribution of the vector data. These vectors are the result of applying PCA over the entire training set. They are eigenvectors of the following covariance matrix:

$$C = \frac{1}{n}\sum_{i=1}^{n}\phi_i\phi_i^T = AA^T \tag{3.3}$$

where $A = [\phi_1\ \phi_2\ ...\ \phi_n]$. Usually matrix C is large and computing its eigenvectors is exhaustive. [52][53] introduced a computationally effective way to estimate these vectors. The number of data points in the organ space is n, therefore only $n-1$ meaningful eigenvectors exist and the remaining eigenvectors will have associated eigenvalues of zero. Due to this, the eigenvector equation can be solved for an n by n matrix instead of a $X{\cdot}Y{\cdot}Z$ by $X{\cdot}Y{\cdot}Z$ matrix. Considering the eigenvectors v_i of A^TA such that:

$$A^TAv_i = \mu_i v_i \tag{3.4}$$

Pre-multiplying by A:

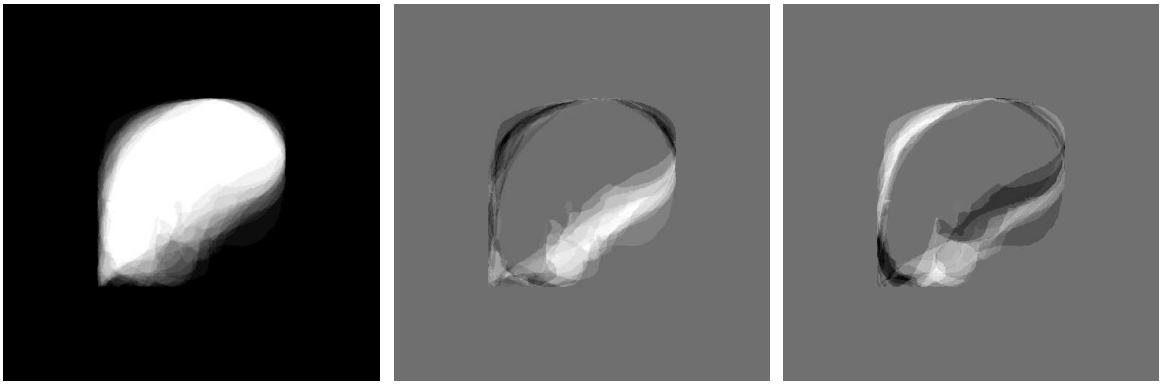

Figure 3.13: Left: mean vector ψ, Middle: first eigenvector u_1, Right: second eigenvector u_2.

$$AA^T Av_i = \mu_i Av_i \tag{3.5}$$

Equation 3.5 shows that Av_i is an eigenvector of AA^T. Using this, instead of calculating the eigenvectors of AA^T, the eigenvectors of $A^T A$ are calculated and are called v_i. Linear combination of v_i and the n training set vectors (ϕ_i) is used to form the eigenvectors that represent the organ space and are called u_i. This is performed by:

$$u_i = \frac{1}{n} \sum_{j=1}^{n} v_{ij} \phi_j \tag{3.6}$$

Once eigenvectors are approximated, they are used to model the organ. This model is used (as explained in the Section 3.3.2.4) to measure the similarity of segmented regions (candidate hypotheses) to the organ. Figure 3.13 shows the mean vector and the first two eigenvectors for a training set of 2D liver masks.

3.3.2 Testing Phase

This phase is responsible for processing unknown CT scan volumes to identify regions of the organ of interest. This phase includes four main processes that are explained next.

3.3.2.1 Pre-processing

To initially localize points that belong to the organ of interest, we propose a pre-processing procedure. This procedure utilizes specific and unique physical attributes of the organ and

its environment to identify regions of CT images (in one slice or more) that belong to that organ. Clearly this procedure must be customized for different organs. We discuss in details examples of such procedure in the applications of the proposed method for 3D modeling of kidney and liver.

3.3.2.2 Candidate Hypotheses Generation

For creating potential segment hypotheses, any generic segmentation algorithm may be utilized. The basic idea is to create a set of variant segmentation parameters (algorithm dependent) that drives the segmentation results from under segmentation to over segmentation. For instance, let's assume that a segmentation algorithm Seg depends on N parameters p_1,..., p_N. If the lower and upper boundaries of these variables, presented by (v_{1l}, v_{1u}),...,(v_{Nl}, v_{Nu}), drive the output results from under to over segmentation, a combination of values for $p_1 \in [v_{1l}, v_{1l} + \Delta l_1,...,v_{1u}]$,...,$p_N \in [v_{Nl} + \Delta l_N,..., v_{Nu}]$ will be generated to segment the input image multiple times. Every unique combination of p_1,..., p_N generates one set of segmentation results. The number of overall output segments depends on Δl_i where $i \in 1,...,N$.

3.3.2.3 Candidate Hypotheses Refinement

The purpose of this process is to refine potential candidates by utilizing information that was identified in the pre-processing phase. In general, this phase could rely on organ specific information to remove outliers. It could also involve further analysis (based on local or global features) to verify the fidelity of a hypothesis to the organ.

3.3.2.4 Candidate Selection Based on Similarity to the Organ Space

Similar to the approach proposed by [52], where the face space was used for face detection, the organ space can be used to measure the similarity of a candidate hypothesis to the organ. Each candidate hypothesis is a vector data, same as the training dataset that was used to create the organ space. For measuring the similarity of each candidate hypothesis vector (L_{hypo}) with the organ, first, the mean adjusted hypothesis vector ϕ_{hypo} is projected onto the organ space using:

$$\phi_{hypo} = L_{hypo} - \psi \tag{3.7}$$

$$\eta_i = u_i \phi_{hypo} \tag{3.8}$$

The result of this projection is a vector of $[\eta_1, \eta_2, ..., \eta_n]$. Each η_i represents the contribution of an eigenvector u_i in the reconstruction of projected candidate hypothesis. The reconstructed candidate hypothesis is then generated by:

$$\phi_{rec} = \sum_{i=1}^{n} \eta_i u_i \tag{3.9}$$

For each refined candidate hypothesis, generated in Section 3.3.2.3, the Euclidean distance between the mean adjusted volume (ϕ_{hypo}) and the reconstructed version (ϕ_{rec}) is computed by:

$$E = \| \phi_{rec} - \phi_{hypo} \| \tag{3.10}$$

The candidate hypothesis with the smallest Euclidean distance from its reconstructed version in the organ space is chosen as the best segmentation result. Here it must be noted that the validation scheme is only able to validate the candidate hypothesis whose characteristics such as shape, lie within the variations encoded by the PCA model. In other words, only the candidates that vary in the ways seen in the training set can be validated by the model.

In the following sections, the application of this algorithm is explored over segmentation of both kidney and liver organs.

3.4 Application of MOVS for Kidney Segmentation

In this section, the application of the proposed method for segmentation of the 3D right and left kidneys in CT scan volumes is presented. We follow the same organization as in Section 3.3 for presenting processes utilized in this application.

3.4.1 Training Phase: PCA based Model Generation

For this application, a kidney space is generated for the 2D cropped images of the kidney from the training set of MICCAI's grand challenge workshop [18][19]. It is worth to mention that different volumes of the data have different thicknesses. They usually range between $0.7mm$ to $5mm$ in the Z direction (transverse) with the aspect ratio of 0.586:0.586:1 for

each voxel. In order to establish correct correspondences between different volumes, all the volumes are re-sampled to the same number of slices (100) in the Z direction. First the CT volume is divided into several sections in the transverse direction with each section containing the same number of slices in them (5 slices in this work). The kidney is then manually extracted for all slices (as the ground truth in the MICCAI dataset was presented only for the liver) and translated into the center of a blank image with the same size as the image slice. The kidney images of each section, from the training set of MICCAI's CT volumes, are used to train the kidney space for that section of slices. Here, shape, texture, intensity, and size of kidney regions are more similar to each other for closer slices. Therefore, multiple kidney spaces are generated for different temporal sections of CT volumes along the transverse direction. The process of assigning different slices to different sections is shown in Figure 3.14.

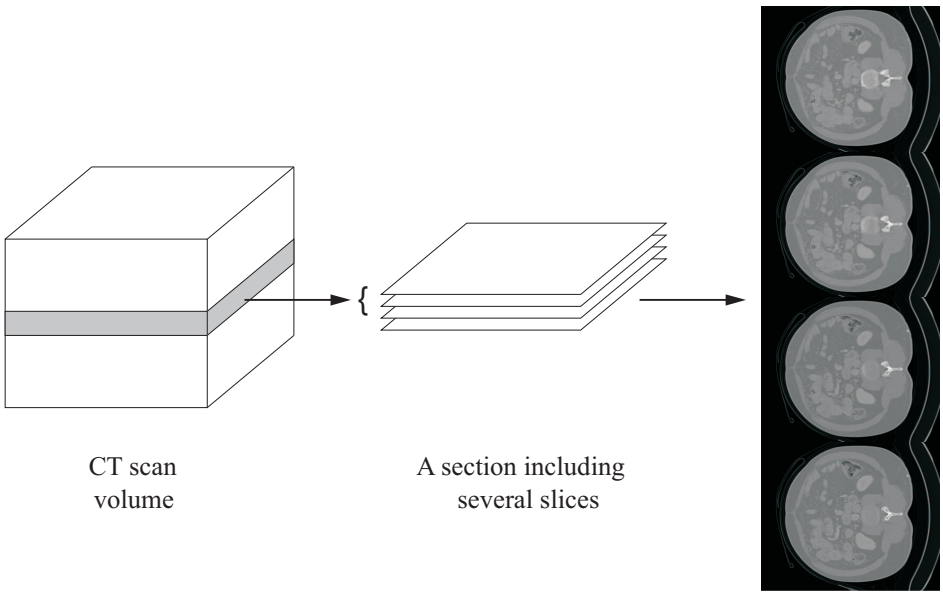

Figure 3.14: Different sections of CT scan volumes used for training separate kidney spaces.

3.4.2 Testing Phase: Pre-processing

In this application, the pre-processing phase includes two main automatic processes: aligning the dataset volumes, and identifying those slices of each volume that indeed include the organ of interest and finding an initial starting point within the organ.

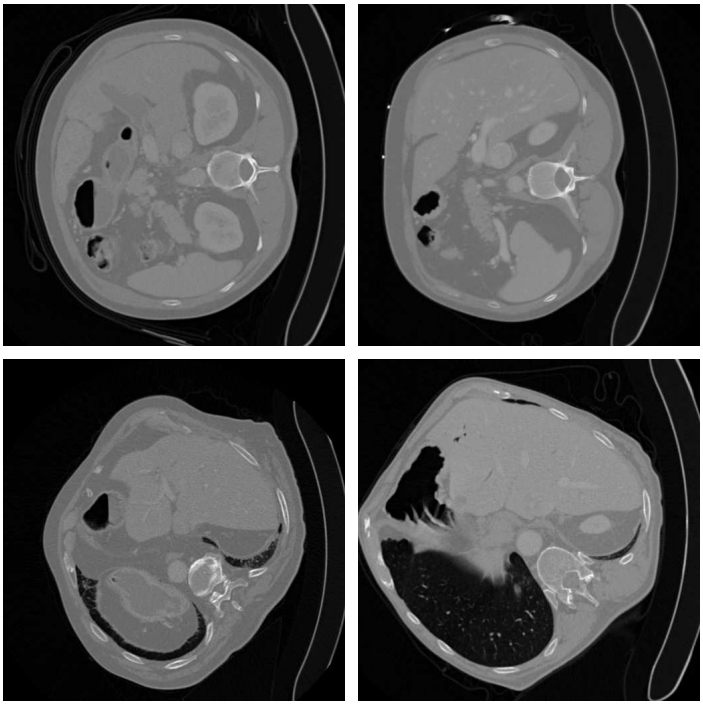

Figure 3.15: Top row: 2D images from volumes with orientation of angle zero, Bottom row: 2D images from volumes rotated from angle zero.

3.4.2.1 Aligning volumes

Most CT scan volumes of the used dataset have orientation angle of zero meaning the patient's back is rested on the right side of the image and the body is positioned along the horizontal line. However, some of the datasets seem to be created when the patient's body is rotated from angle zero. This is shown in Figure 3.15. In this figure, there are two images from volumes at zero angle and two images from volumes rotated by non-zero angles.

In order to generate the organ model from the training set or projecting the segmentation candidates onto the organ space, it is necessary that all the dataset volumes are aligned at the same rotation angle. In order to identify the orientation of the dataset volume and to correct for potentially various orientations, the following algorithm is implemented:

i. The area associated with the spine (referred to as spine mask) in the physical middle slice of each test volume in the transverse direction is extracted according to the described procedure in Section 3.4.2.2.ii.a. The center of gravity of this mask is also computed.

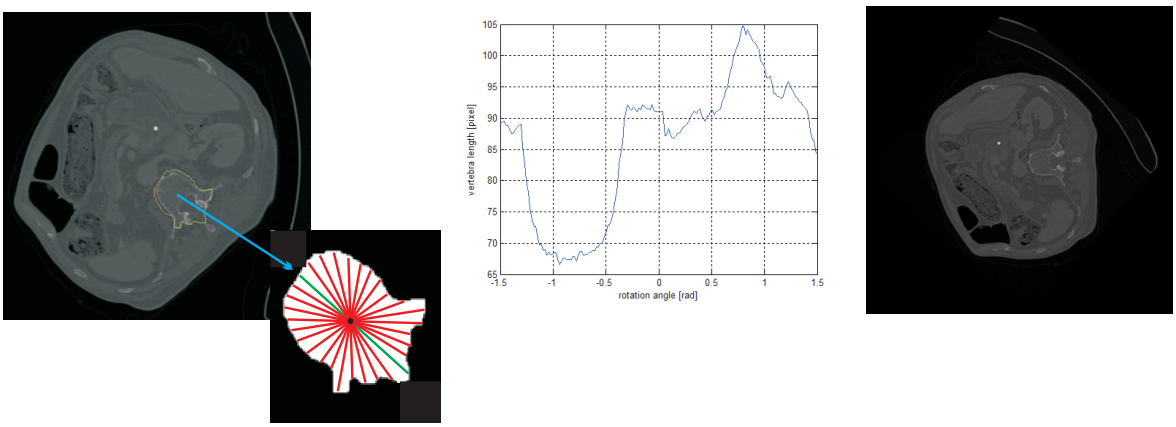

Figure 3.16: Visual presentation of the aligning process for dataset volumes.

ii. The lengths of all line segments passing through the center of gravity and limited to the boundaries of the mask (with an incremental rotation angle of 1 degree ranging from -90 to +90 degrees) are computed.

iii. The rotation angle corresponding to longest line segment is found. The image is then rotated back by that angle. After the rotation the longest axis of the spine mask becomes parallel with image horizontal axis. To make sure that the spine is always rotated in the correct direction (we want the spine to be on the right side of the image) the distance of the spine mask's center of gravity from image right border is used. Once the rotation angle and the rotation direction are estimated, all slices of the volume are rotated. This procedure is shown in Figure 3.16.

3.4.2.2 Organ region identification

In this phase, first the upper and lower slices, corresponding to the beginning and end of the kidney in the CT volume, are automatically identified. Once these slices are identified, their middle slice is processed to find the kidney region in it. This section includes two main procedures.

i. A fully automated organ reconstruction system requires automatic identification of slices that include that organ within each volume. Such algorithm varies from organ to organ as characteristics of various organs differ. Here, we introduce a method for

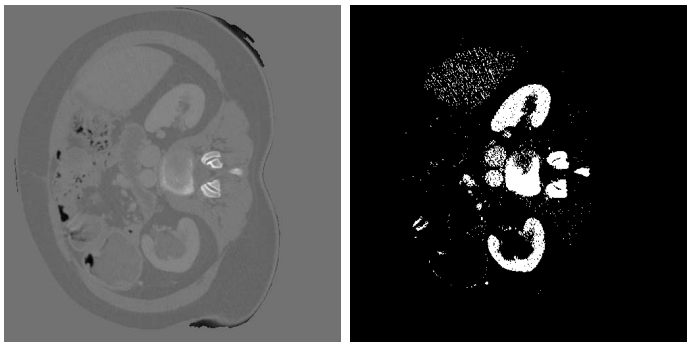

Figure 3.17: Left is the slice from transverse direction containing only the abdominal area and right is the thresholded image.

identification of the lower and upper boundary slices of the CT volume that contain the kidney (in the transverse direction). This algorithm includes three steps:

(a) In the first step, each slice is thresholded in the transverse direction using a dynamic threshold value. The threshold is determined for every slice as follows:

$$TR = k \times mean(I) \tag{3.11}$$

here k is set to 1.35 (a constant value for the entire dataset volumes, found empirically) and I is the image region corresponding the abdominal area of each slice (estimated as described in Section 3.4.2.2.ii.b). This is shown in Figure 3.17.

(b) Next we identify a slice that includes the kidney. This slice is called starting slice. Based on the observation from the training datasets, usually slices that fall between the bottom slice of the liver and the slice corresponding to the largest 2D liver surface (in the transverse direction) contain a slice that corresponds to a large 2D segment of kidney. Identification of slices containing the largest 2D surface and the bottom slice of the liver are described in Section 3.5.2. Therefore, the slice corresponding to the midpoint between these two slices is chosen as the starting slice of each volume. Using the kidney subregion area, as described in Section 3.4.2.2.ii.c, a kidney mask guesstimate is extracted for the starting slice. The thresholded image from step 3.4.2.2.i.a is then utilized to identify the segment with largest area within the kidney subregion.

(c) Finally, the algorithm propagates the kidney mask guesstimates in two directions from the starting slice (in the transverse direction). The propagation is performed by choosing the segment with the largest area overlap with the kidney mask guesstimate of the previous slice. This process continues in both directions until the mask guesstimates reach to zero at the two ends which highlight the slice boundaries of the kidney for that dataset volume.

ii. In this section, the middle slice of the kidney slices is processed to estimate the approximate location of the kidney. The relative location of the kidney with respect to the spine is used for this purpose. This procedure includes the following steps:

(a) In CT scan images of the abdominal area, pixels corresponding to bones (spine and ribs) appear substantially brighter than pixels of soft tissue regions. Using intensity based thresholding approach (similar to [22]), the middle slice is thresholded. The threshold value is found empirically based on the training dataset. For CT scan images with maximum and minimum pixel values of 1024 and -1024, this threshold was set to 400. To make the process more robust, 10 slices before and 10 slices after the middle slice are also thresholded. The thresholded results of all 21 images are unionized. The resulting image is a binary mask that holds values of 1 for spine and rib regions and 0 otherwise. In this process, some soft tissues with brighter intensities (as shown in Figure 3.18.a) could be wrongly thresholded and therefore will be added to the mask. These points usually sparse and are filtered out using a morphological operations that first fills the holes and then removes rib regions (connected to the spine) using a disk structuring element of radius 4 pixels (Figure 3.18.b). The largest connected piece in the resultant image is then identified as spine, as shown in Figure 3.18.c. Also Figure 3.19 shows the spine extracted for a number of selected slices from different volumes.

(b) In the next step, we extract the boundary of abdominal area. For this, first the middle slice is enhanced using a Log transform. Canny edge detector is then applied to extract an edge map image. The NOT of the resulting edge map image is opened with a circular structuring element of radius 4. The largest piece of the resultant mask is selected. This region represents the entire abdominal area and its boundary is extracted to highlight the region in which the kidney is located (Figures. 3.18.d, e and f). Figure 3.20 shows the extracted abdominal region for

a number of selected slices from different volumes.

(c) In the final step, we require to identify a subregion within the abdominal area that most likely contains the kidney or parts of it. Focusing on processing a smaller region of the image, reduces the chance of misidentification of the kidney which is a real problem given it's size and texture in comparison with its neighboring organs such as heart and gall bladder. Usually, the location of the kidney with respect to the spine lies on a line that creates a 70^o angle with the horizontal line passing from the center of the spine (Figure 3.21.a). The 70^o is determined empirically. Therefore from the center (center of gravity) of the spine mask, a line is emitted at 70^o and its intersection with the boundary of the abdominal region is found (length of l). Center of the kidney is usually located at a distance of $0.3l$ from the center of spine. A circular region (radius of 50 pixels) that most likely withholds the kidney, is then centered at the location of $0.3l$. Figure 3.21.b represents the identified circular region for a sample slice. For the left kidney the angle of the line is -70^o with the horizontal line passing from the center of spine. Samples of the extracted kidney region for left and right kidney from a number of selected slices in different volumes are depicted in Figure 3.22.

3.4.3 Testing Phase: Candidate Hypotheses Generation

After the pre-processing, segmentation is performed on all images of the CT scan volume and all candidate segments are identified. These candidates are generated for every 2D slice of each volume of the test set using the graph based segmentation method [46]. Graph based segmentation is a method capable of preserving details in low-variability image regions while ignoring details in high-variability areas. The algorithm includes following steps:

i. Each image pixel is considered as a region where it corresponds to a node ($v \in V$) in the overall image graph of $G(V, E)$.

ii. Neighboring pixels are connected by undirected edges ($e \in E$). For each edge a weight coefficient is computed according to the dissimilarities between pixels.

iii. Similar regions A and B are merged together to produce a larger region if the following condition is held:

$$Dif(A, B) \leq MInt(A, B) \tag{3.12}$$

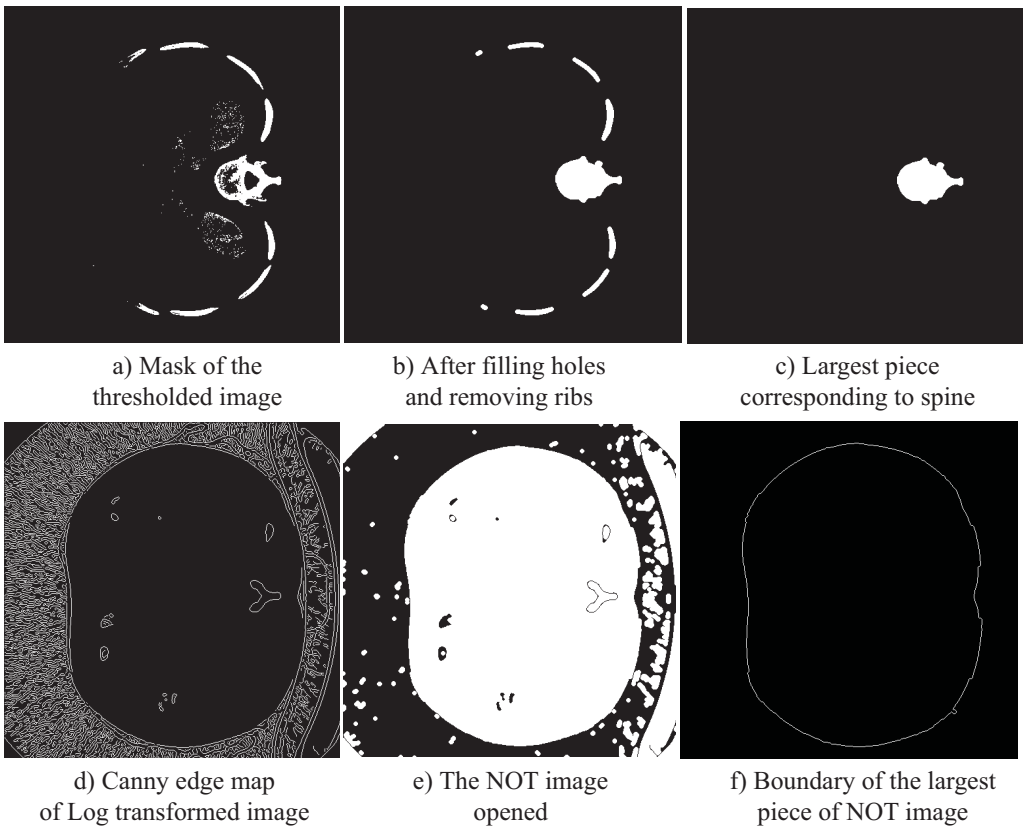

Figure 3.18: Kidney extraction pre-processing: extracting spine and abdomen area boundary.

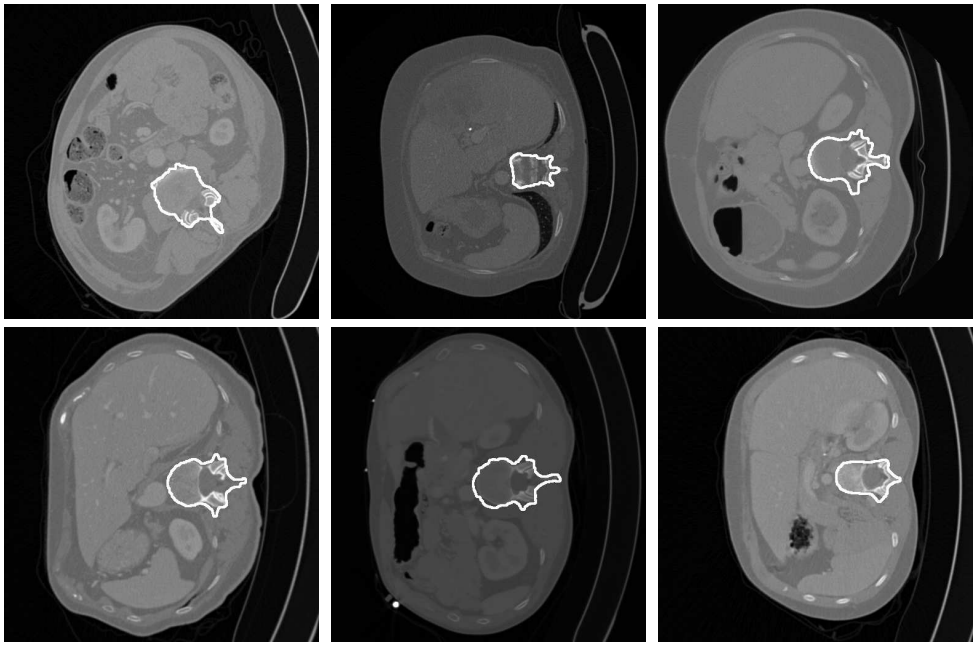

Figure 3.19: Kidney extraction pre-processing: spine region determined for sample slices of different volumes.

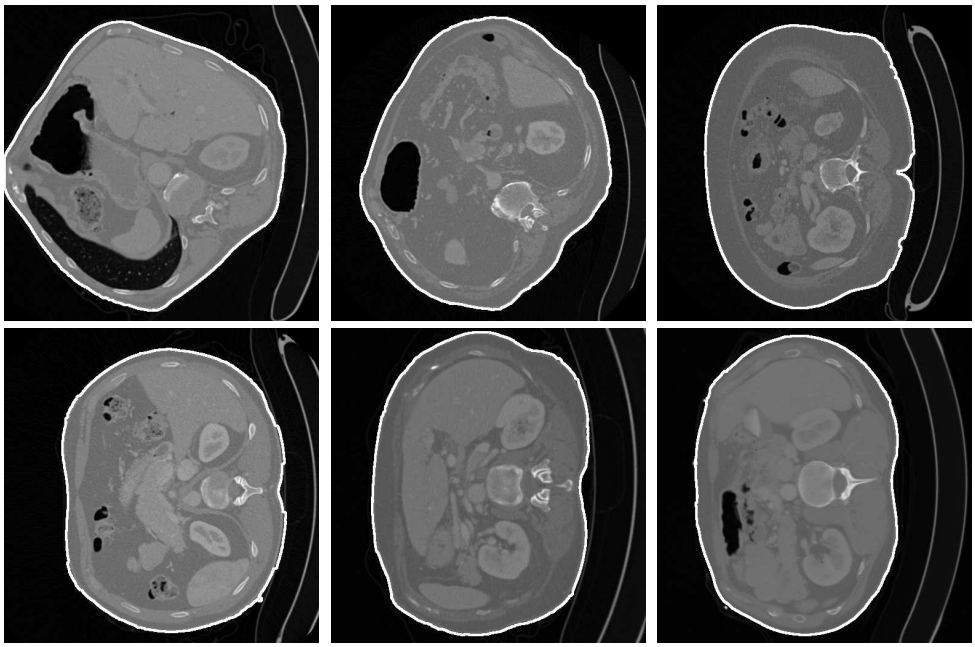

Figure 3.20: Kidney extraction pre-processing: abdominal area determined for sample slices of different volumes.

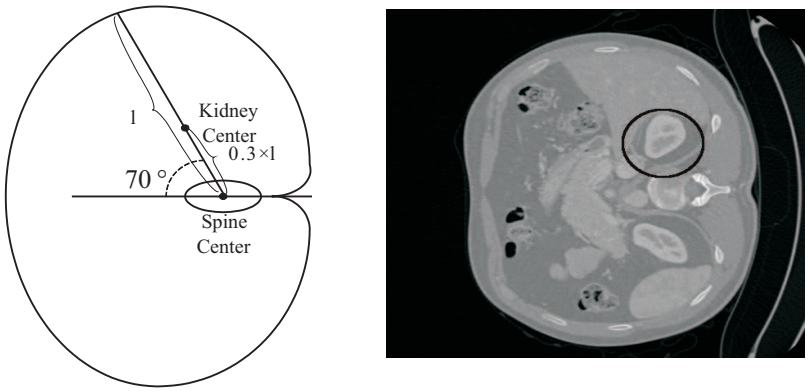

a) Kidney center calculation

b) Kidney area highlighted

Figure 3.21: Kidney extraction pre-processing: extracting kidney location center.

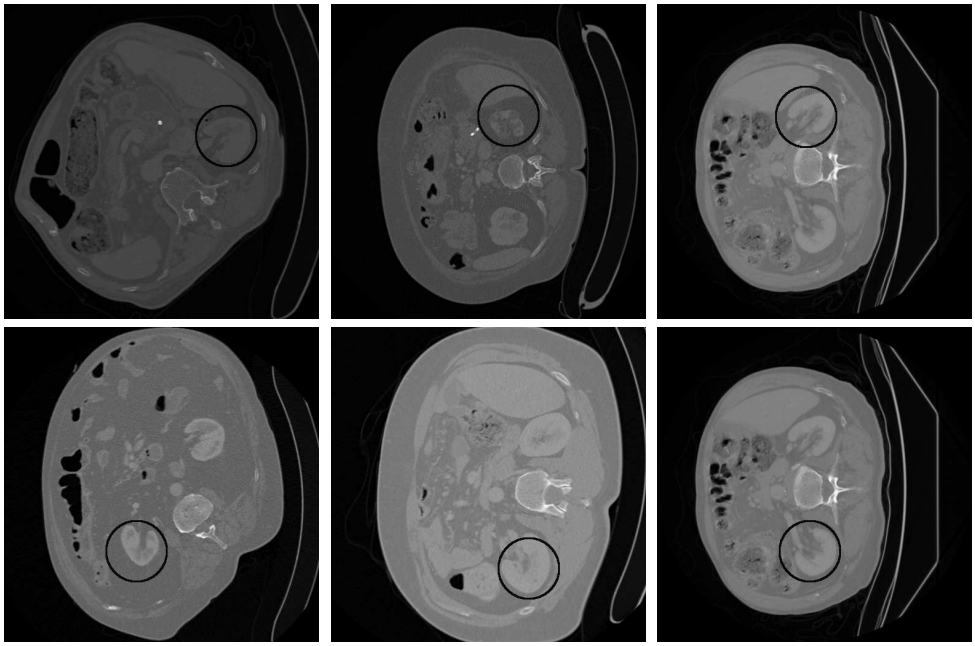

Figure 3.22: Kidney extraction pre-processing: left and right kidney region determined for sample slices of different volumes.

Where

$$Dif(A,B) = \min_{v_i \in A, v_j \in B, (v_i,v_j) \in E} w((v_i,v_j)) \tag{3.13}$$

Here E is the graph edge set and $w((v_i,v_j))$ is the weight between vertex v_i and v_j.

$$MInt(A,B) = min(Int(A) + \tau(A), Int(B) + \tau(B))) \tag{3.14}$$

$$Int(A) = \max_{e \in MST(A,E)} w(e) \tag{3.15}$$

MST represents the Minimum Spanning Tree graph $G(V,E)$.

$$\tau(A) = \frac{k}{|A|} \tag{3.16}$$

The control parameters of this algorithm include: Gaussian smoothing σ, threshold function τ, and scale of observation k.

The range of values selected for σ and τ are found through statistical analysis of the data in the training sets. Initially, values of $\sigma \in [0.1 : 0.2 : 1.7]$ and $\tau \in [5 : 25 : 155]$ were used to segment each slice of every training dataset volume, $9 \times 7 = 63$ segment images for each slice. The overlaps of all segment images of a slice with the mask of that slice (from the ground truth) are computed and the σ and τ of the segment image with the highest overlap are collected. The histograms of the distribution of these two parameters were then estimated, as shown in Figure 3.23.

Using these histograms, a range of $[0.1 : 0.2 : 1.1]$ for σ and a range of $[5 : 25 : 105]$ for τ are chosen. These ranges cover 90% of the best potential σ and τ according to the training dataset volumes. The observation scale of k proved to have minimal affects on the results and therefore was kept constant at 50. Figure 3.24 shows a few segmentation candidates for a sample slice. The top and middle rows contain bad segmentations while the bottom row shows examples of good kidney segmentation for this particular slice.

At the end of this process, for each slice of the CT volume a large number of candidate segments are generated. These candidates are refined in the next process.

3.4.4 Testing Phase: Candidate Hypotheses Refinement

This procedure begins from the middle slice. Using the kidney's potential location (found Section 3.4.2.2.i.c), all detected segments of the middle slice, are inspected and only those

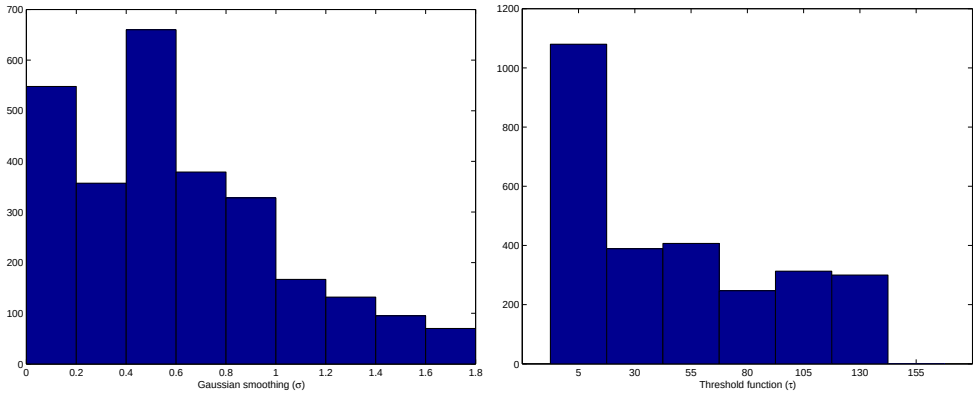

Figure 3.23: Distributions of σ and τ values for the kidney.

that fully or partially overlap with that circular region are kept. For the middle slice, all these candidates are passed to Section 3.4.5 where only one segment that represents the best kidney region for the middle slice is selected.

The process of hypotheses refinement for other CT slices is slightly different from the middle slice and it is based on the overlap of candidate hypotheses with the best candidate segment from the previous slice. Since the starting point for the processing is the middle slice, this procedure treats CT slices in two batches. Both batches start from the middle slice but move in opposite directions. In each slice, all candidate hypotheses that have overlaps smaller than 50% with the kidney segment (best chosen segment) of the previous slice will be removed.

At the end of this process, for each slice, a number of hypotheses remain that location- and size-wise are the most probable representative of the kidney region for that slice.

3.4.5 Testing Phase: Best Hypothesis Selection

At this point, for each slice there are a number of potential kidney region hypotheses. These candidates are projected into their corresponding kidney space (from Section 3.4.1) and the hypothesis with the smallest Euclidean distance (as described in Section 3.3.2.3) is chosen as the kidney region (kidney mask) of that slice. Once the best candidates for all slices are identified, they are stacked up together to generate a 3D model of the kidney. To refine this 3D model, a post processing procedure based on morphological operation in the sagittal direction is performed. Here the mask slices of the kidney (in the sagittal direction) are first opened by a disk structuring element of radius 2 pixels and then closed by a disk structuring

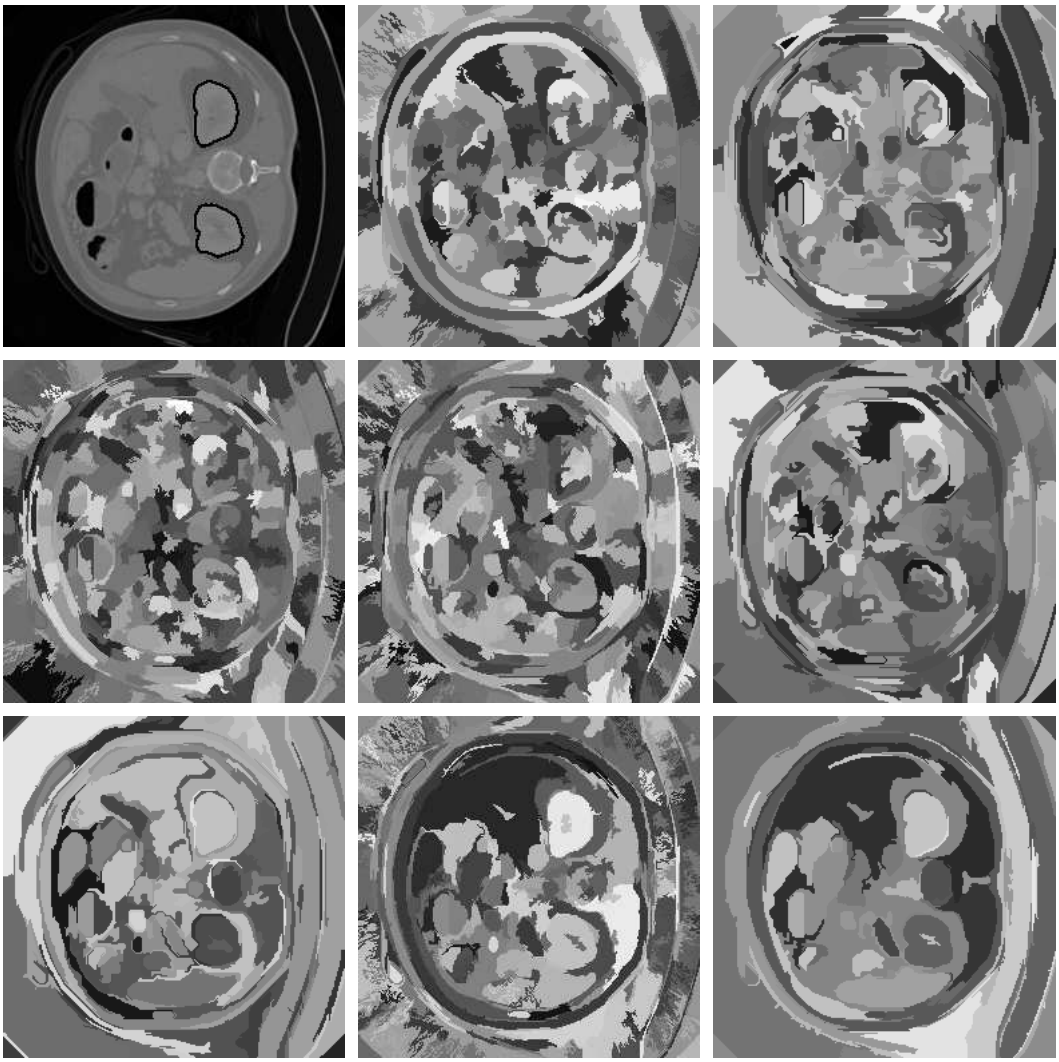

Figure 3.24: Kidney segmentation candidates. The image on the top left corner shows the ground truth. The candidates here are generated according to the proposed range of parameters for kidney.

element of radius 4 pixels. This procedure fills out small holes inside the kidney mask and removes the excess small parts attached to its boundaries.

3.4.6 Results

Some segmentation results for different CT slices are shown in Figure 3.25. In these results, the ground truth are shown with black solid lines and the contours found by the proposed method with white lines. The quantitative assessment of the algorithm based on the entire test set volumes is presented in Section 4.

3.5 Application of MOVS for Liver Segmentation

In this section, the application of the proposed method for segmentation of 3D liver in CT scan volumes is presented. For this application, the organ space is generated from 3D mask volumes of the liver of MICCAI's 2007 grand challenge workshop training dataset of twenty patients.

The human liver has a soft triangular shape with four lobes that are different in shape and size. Slicing 3D CT volumes of liver in the transverse direction usually results in images that include more than one liver piece. This adds to the complexity of candidate hypotheses and makes their identification process more complicated. Therefore, CT volumes of liver are processed in the coronal and sagittal directions in which the observed 2D liver regions consist of one single piece.

3.5.1 Training Phase: PCA based Model Generation

Similar to Section 3.4.1, in this section a liver space is generated for 3D masks in the training dataset. Liver masks for 2D slices of CT training volumes are extracted and stacked up as shown in Figure 3.12. These 3D mask volumes are used to generate the liver space. This liver space is later used for assessment and identification of candidate segment hypotheses.

3.5.2 Testing Phase: Pre-processing

The pre-processing phase includes two main automatic processes: aligning the dataset volumes, and identifying those slices of each volume that indeed include the liver. The alignment of dataset volumes is performed by procedure presented in Section 3.4.2.1. Since the

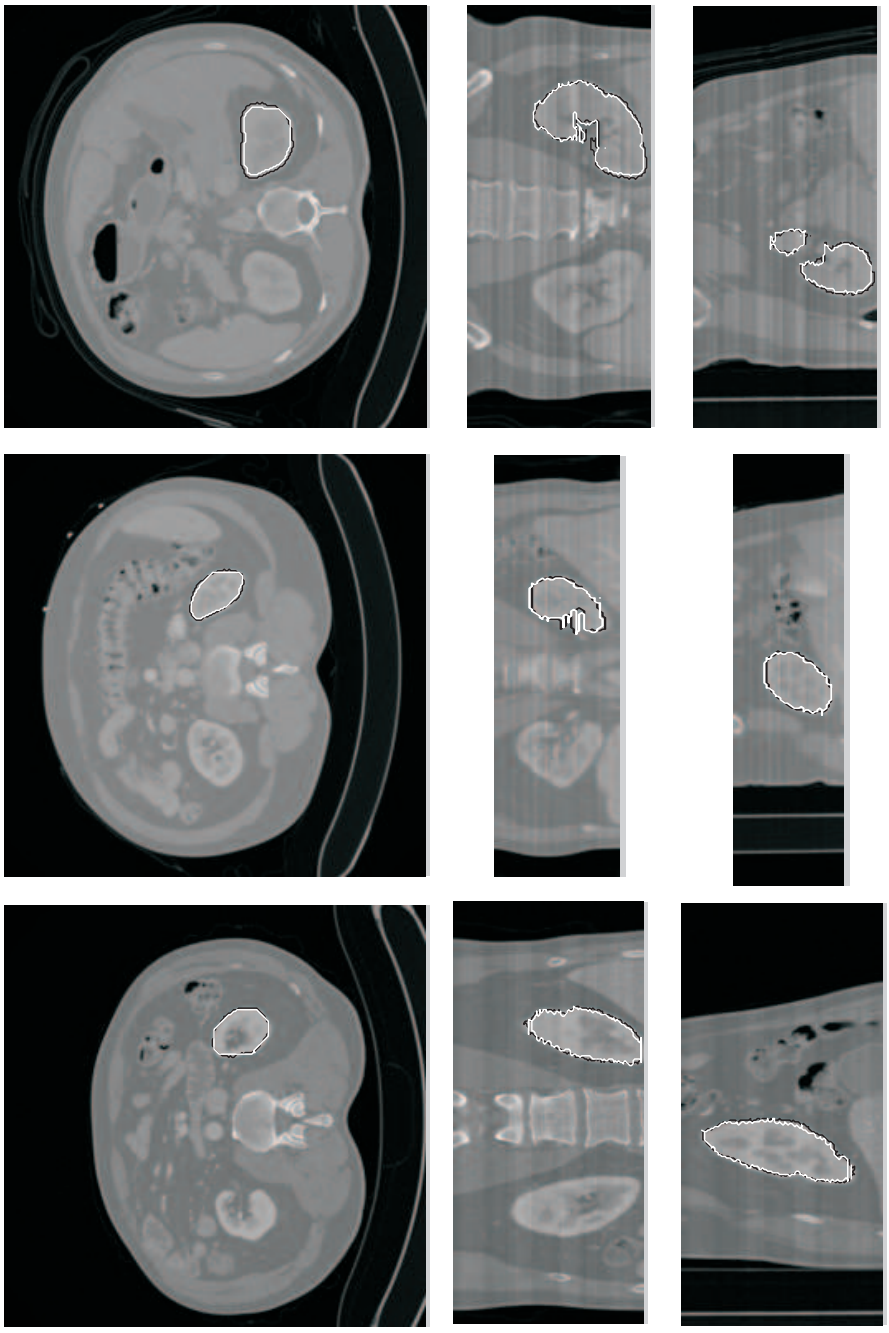

Figure 3.25: Sample results of kidney segmentation in transverse (left column), coronal (center column) and sagittal (right column) directions; black contours: ground truth, and white contours: boundaries found by our work (MOVS).

number of slices and the location of the liver in each volume vary, the following procedure is performed to identify those slices that include the liver. This procedure includes three steps:

i) In the first step, a number of 3D models of the liver are generated using segmentation results of the liver slices in the sagittal and coronal directions. The human liver is the largest glandular organ of the body within the abdominal area. When looking at the CT volumes, the middle slice (regardless of the number of slices) always includes a segment from the liver. Also in the middle slice, the segment corresponding to the liver usually is the largest segment among all detected segments that correspond to other organs or areas. These two observations are utilized in this step. Therefore, starting from the middle slice of each test volume and moving in two directions, for both sagittal and coronal axes, we generate 21 3D liver models by changing a threshold called: β, in each case. The role of this threshold is described in the candidate hypotheses refinement stage in section 3.5.4. This number of liver models has been chosen experimentally since this range covered all the desirable candidates for all the volumes in the training set. Each slice of each volume is segmented 21 times. The 3D model for each β is generated by moving from the middle slice in two directions and choosing the segment (for the results of current β) with the maximum overlap with the liver segment from the previous slice. Obviously, the qualities of these models are different and their number depends on the range of segmentation parameters used in the system (in our work 21 3D models).

ii) In this step, the system identifies the slice that most probably corresponds to largest liver region for the test volume (in the transverse direction). For each 3D model generated in step i, the slice (in the transverse direction) corresponding to the largest liver segment is identified. Once all such slices are identified for all the 3D models, a voting scheme is used to identify the most popular slice. The voting scheme unionizes the candidates of each slice to select the slice with the largest union area. We refer to this slice as the center slice although it generally does not correspond to the physical center of the liver. Once this center slice is identified, the next step is incorporated to estimate the upper and lower boundaries of the liver slices.

iii) In this step the liver's upper and the lower boundary slices in the transverse direction are identified as following:

(a) A number of liver mask candidates are generated for the center slice that was found in step ii. As described in Section 3.3.2, using a range of segmentation parameters, a number of liver segments are generated (one segment for each set of parameter). All these candidate segments are added together and thresholded. The threshold value is dynamically chosen so that the resultant segment has the highest similarity with the 2D mask extracted from the 3D training model (Section 3.3.1). The 2D mask of the 3D training model is chosen according to the liver area (the largest).

(b) The remaining slices in the transverse direction are treated in the same way but in two opposite directions. Therefore, each test volume slice image is segmented several times. The segmentation results are added together and thresholded using the threshold value found in iii.a. The segment with the largest overlap with the liver segment from the previous slice is considered as the liver segment for that slice.

(c) This process is repeated until the liver mask area becomes zero in both directions. At that point the algorithm has reached to the boundary slices of that dataset volume.

3.5.3 Testing Phase: Candidate Hypotheses Generation

To highlight the generality of the proposed algorithm, for the liver segmentation application a different segmentation algorithm (the mean shift segmentation method [45]) is utilized.

Mean shift segmentation is a non-parametric feature space originally introduced by Fukunaga and Hostetler in [45]. In this method the maxima of a local density function is located based on a set of data points. In mean shift segmentation usually an attribute of the image (for example color or intensity) is chosen as the feature. Therefore, first a search window is chosen and is centered on an initial location. The mean location of the data in that window represents the new centroid. Therefore, the search window is migrated to a new position which is centered at the location of the centroid found from the previous step. The procedure is repeated until window has reached a local maximum in the density function and the movement of the window's centroid becomes negligible. When segmenting an image, search windows are uniformly positioned over the image data. The converged mean shift window for each initial position is found and windows with the same local maxima

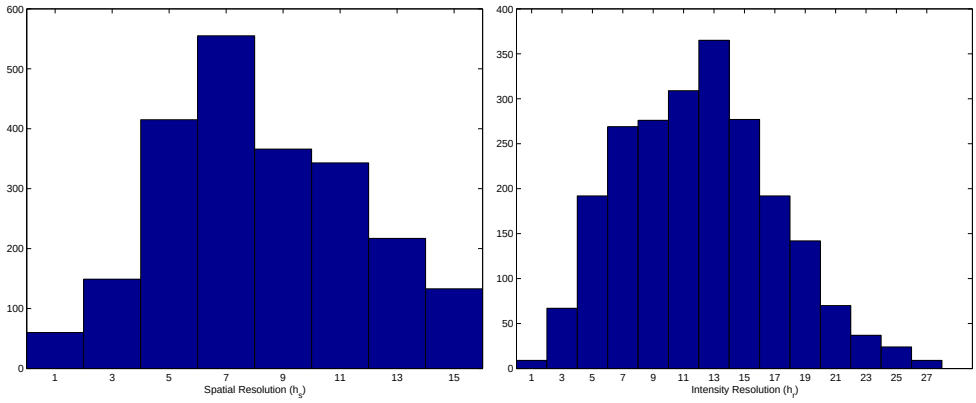

Figure 3.26: Distributions of h_r and h_s values for the liver.

are merged together. The data of the merged windows traversed are considered the same cluster and each cluster corresponds to one segment in the image. Mean shift segmentation algorithm controls the quality of segments through three parameters of intensity (h_r) and spatial (h_s) resolutions, and minimum segment size. The spatial resolution parameter affects the smoothing, and connectivity of the potential segments. The range resolution parameter controls the number of segments. The minimum segment size is the area (in pixel) of the smallest individual segment.

In this work the minimum segment size was kept fixed at 20 pixels. The range of values selected for h_r and h_s are found through statistical analysis of the data in the training sets. Initially, values of $h_r \in [1 : 2 : 27]$ and $h_s \in [1 : 2 : 15]$ were used to segment each slice of every training volume. The overlap of all segmented images of a slice with the mask of that slice (from the ground truth) is estimated and the h_r and h_s of the segmented image with the highest overlap are collected. The histograms of the distribution for these two parameters are then estimated, as shown in Figure 3.26. Using these histograms, the range of h_r and h_s are then set to $[5 : 2 : 23]$ and $[3 : 2 : 13]$. Using these two ranges, over 90% of the data in the training volumes will be segmented to their potential segments. At the end of this process, for each slice of a test CT volume, a number of segments are generated. Figure 3.27 shows a few segmentation candidates for a sample slice. The top and middle rows contain bad segmentations while the bottom row shows examples of good liver segmentation for this particular slice.

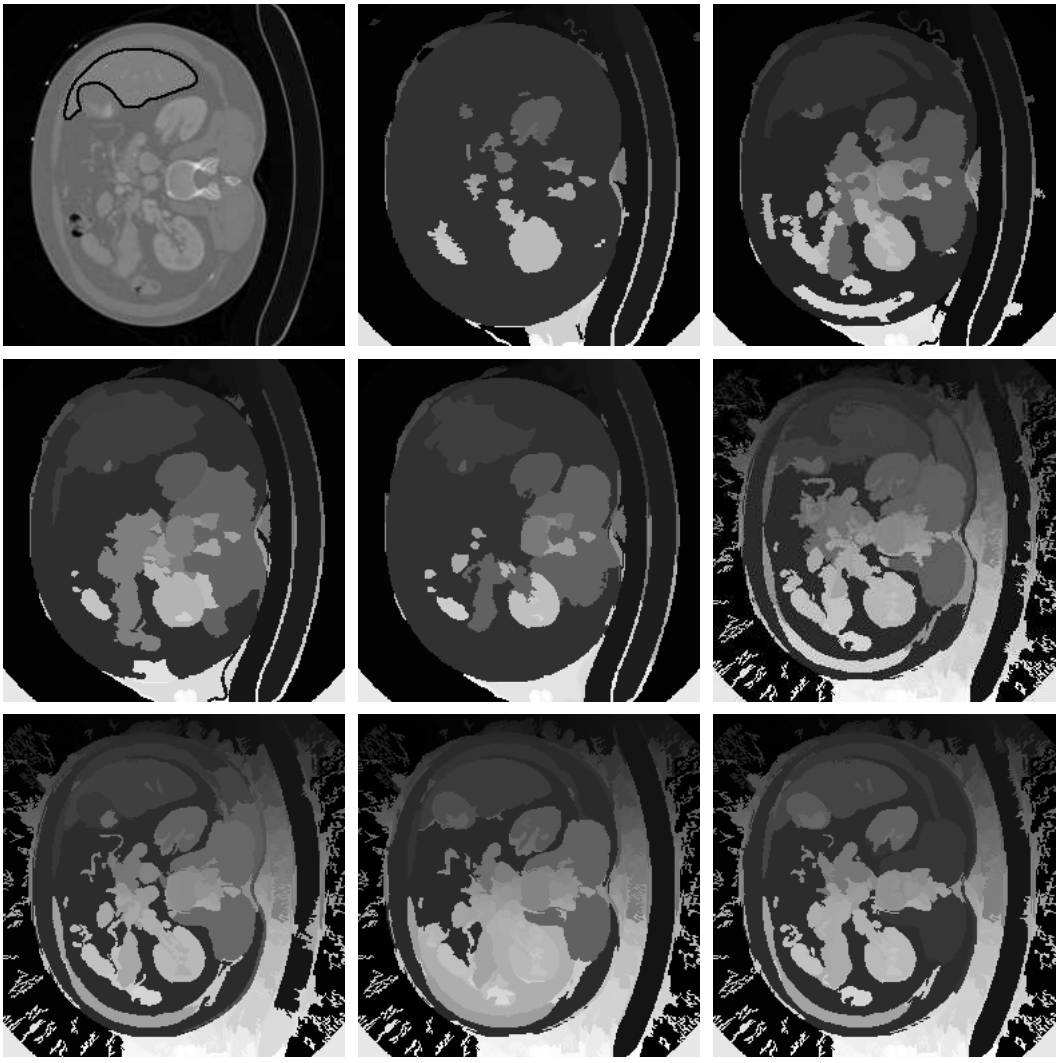

Figure 3.27: Liver segmentation candidates. The image on the top left corner shows the ground truth. The candidates here are generated according to the proposed range of parameters for liver.

3.5.4 Testing Phase: Candidate Hypotheses Refinement

The process of candidate hypotheses generation starts from the middle slice of each CT volume in the coronal and sagittal directions where liver has its largest or near largest 2D surface.

Due to the large size and unique texture of the liver region, the candidate hypotheses generation process tends, occasionally, to cut the liver into smaller pieces. To ensure that such condition does not jeopardize the quality of the process, a post processing procedure is proposed in here. This procedure allows reduction of a large number of segments into a smaller number but more consistent set. It includes the following steps:

i) The boundary edges of segment regions (for each set of parameter combination) are extracted to form an Edge Map (EM).

ii) The EMs of each image (one EM for each set of parameters) are added together to form an accumulative edge map (AEM) for that input image (equation 3.17).

$$AEM = \sum_{s} EM \tag{3.17}$$

iii) The contrast of AEM is enhanced using the Log transform. The AEM image includes a few gray levels. The logarithmic correction in here expands the low-level range of the AEM image. This allows utilizing the thresholding process at finer levels which leads to a larger number of segment candidates with more precise differences.

iv) Contrast enhanced AEM is then thresholded to form an Enhanced Edge Map (EEM) that includes isolated connected regions. This is described by equation 3.18:

$$EEM_{\beta}(x,y) = \begin{cases} 1 & Log(AEM(x,y)) > Thresh \\ 0 & otherwise \end{cases} \tag{3.18}$$

where $Thresh = max(max(Log(AEM)))/\beta$.

The threshold applied here ($Thresh$, the frequency of observation in the segmentation) represents the minimum strength of the boundaries of each segment hypothesis. Naturally, a constant $Thresh$ would not provide same quality results across all input images. Therefore, different values of β are utilized to generate a number of $Thresh$s and EEM images. A

range of [1.5,1.6,...,3.5] for β is used for the liver segmentation in this work. This range was found empirically by inspecting thirty liver CT scan volumes of different patients including a variety of shapes and imaging conditions.

At each slice, different EEMs are generated according to equation 3.18. If the processed slice is indeed the middle slice of the CT volume, the algorithm selects the segment (in EEM) with the largest area as the best segment representative of the liver. If the current slice is not the middle slice of the volume, the segment (in EEM) with the largest overlap with the liver's segment from the previous slice is considered as the liver segment. This segment is first morphologically opened by a circular structuring element (radius of 4 pixels) to remove any excess small parts around its boundary. Next a morphological hole filling process is applied to fill any small gaps within this segment. Sample EEM results with their detected liver segments at different βs are shown in Figure 3.28 for two different volumes. It can be seen that for the first volume of this figure, the β value of 2.5 has provided the best result while for the second volume the β value of 2.3 delivers the best result.

After extracting all liver segments of a volume for a β value, these masks are stacked up together to form a candidate 3D liver mask volume. This implies that for each $Thresh$ value (or β), one liver volume hypothesis is generated.

As mentioned earlier, the segmentation candidate generation for liver is performed in the sagittal and coronal directions. If segmentation results in any of those directions include an extra part attached to them, when viewing from transverse direction, such extra part manifest itself as a line of angle zero or 90 degrees. This is clearly under the condition that such an extra piece is not constantly found on consecutive slices. To filter out such those lines, first all detected segments are stacked together to create a 3D model. Then the model is sliced in the transverse direction and filtered using a morphological post processing with a line structuring element.

Figure 3.29 shows three examples of 3D volumes generated for different values of β along with the associated 3D ground truth for two different volumes. Here it can be seen that the best value of β for the first volume was 2.5 and for the second volume it was 2.3.

3.5.5 Testing Phase: Best Hypotheses Selection

After generating all liver volume candidate hypotheses (including all candidate hypotheses for both sagittal and coronal directions) they are projected into the liver space according to equation 3.8. They are then reconstructed using equation 3.9 and the hypothesis with

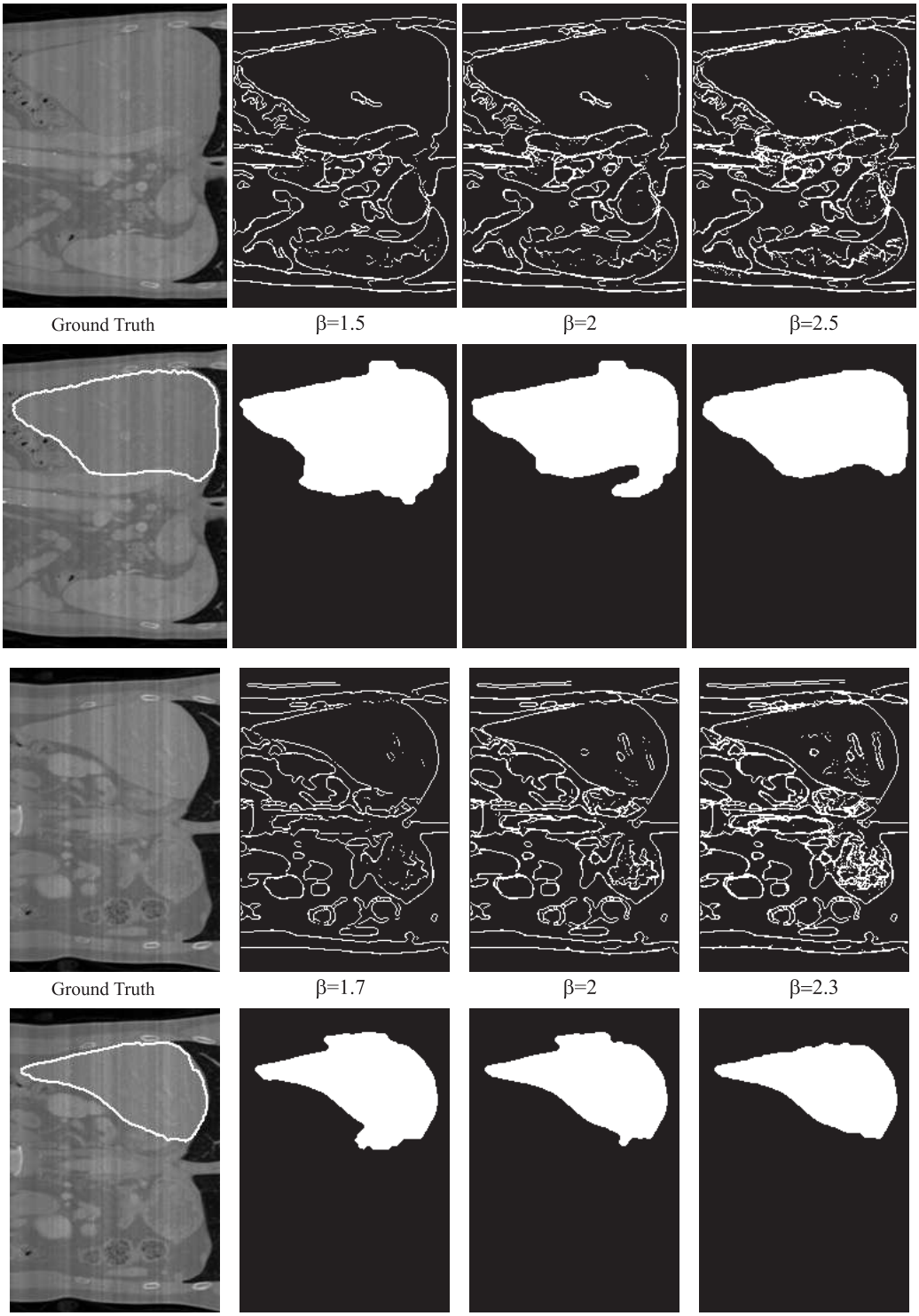

Figure 3.28: Sample EEM and corresponding masks for different β values for two different volumes. The first two rows are from one volume and the bottom two rows are from another volume. In each volume case, top row is the EEM and the bottom row is the corresponding extracted mask candidate for the liver extraction application.

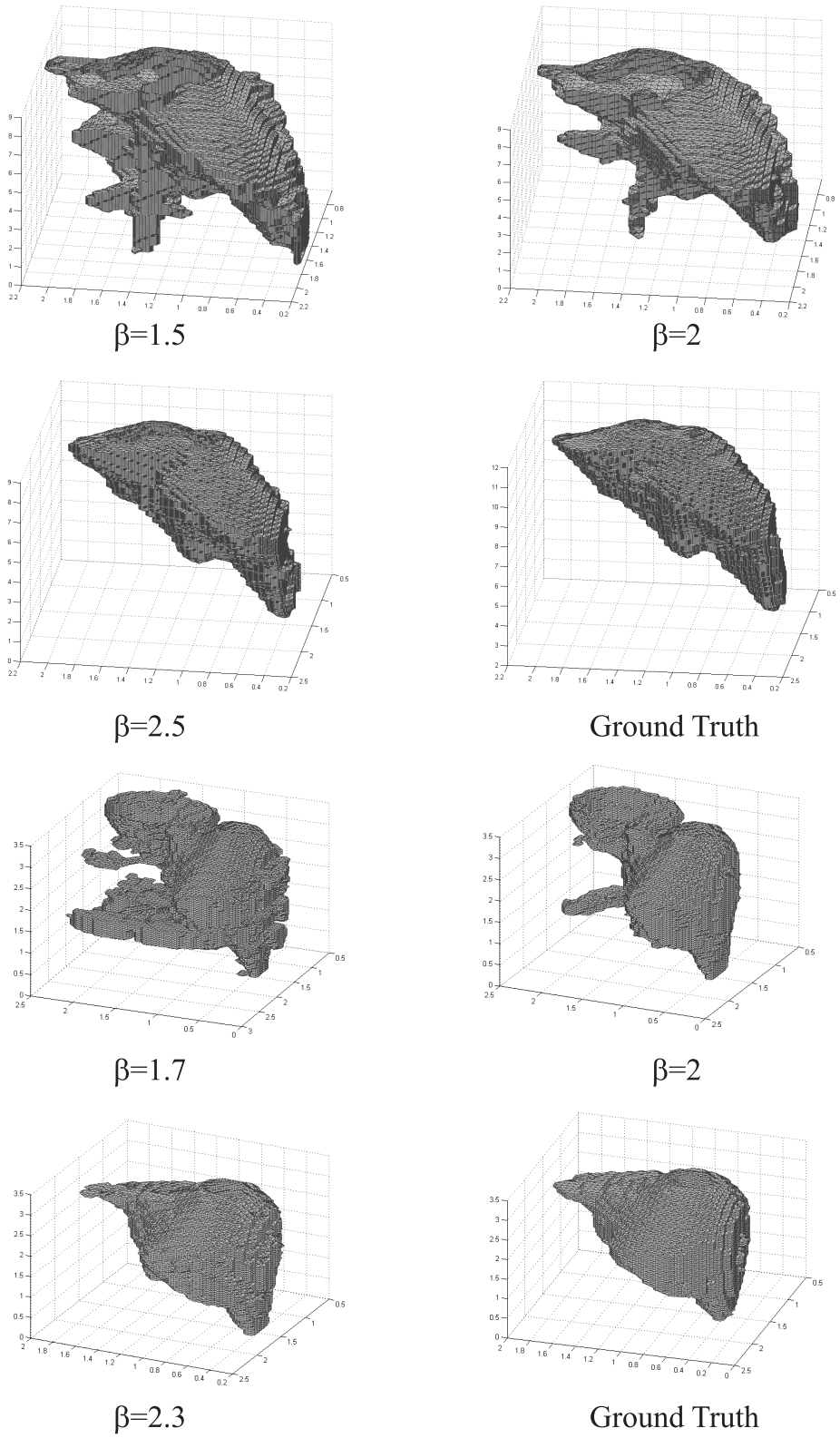

Figure 3.29: Sample 3D volume mask representation for different β values in the liver extraction application. First and second rows belong to one volume while third and fourth row are from another volume.

the smallest Euclidean distance from its reconstructed version is chosen as the best 3D reconstructed model of the liver for that CT volume. Note that here we have created two sets of models: one using the data in the sagittal direction and one using the coronal direction. The two sets of models are then measured against the PCA model and the model with the highest similarity will be chosen. Therefore the final selected 3D model could have been originated from either sagittal or coronal directions.

3.5.6 Results

Figure 3.30 shows some examples of the detected 2D liver mask boundaries along with their corresponding ground truth at transverse, coronal and sagittal directions.

In these results, the ground truth is highlighted by black solid lines and the boundaries by the proposed method are shown with white lines. Quantitative results along with a comparison with the state of art are presented in the next chapter.

3.5.7 Comparison of DERMS and MOVS

As mentioned before the DERMS method had been applied for segmentation of the liver from the same dataset. Quantitative results for the DERMS method are shown in Table 4.3 while the quantitative results for MOVS for liver and kidney segmentation are discussed in the next chapter. The results of MOVS over liver segmentation are shown in Table 4.4. Comparison between these results shows that MOVS is performing better and more robust across all the volumes in the dataset while DERMS is performing poorly over a number of volumes and the results for DERMS is not robust for all the volumes. In order to graphically illustrate the improvement in performance of MOVS in comparison to DERMS, Figure 3.31 shows a few examples. Here the segmentation of DERMS and MOVS over the same slices are compared with respect to the ground truth.

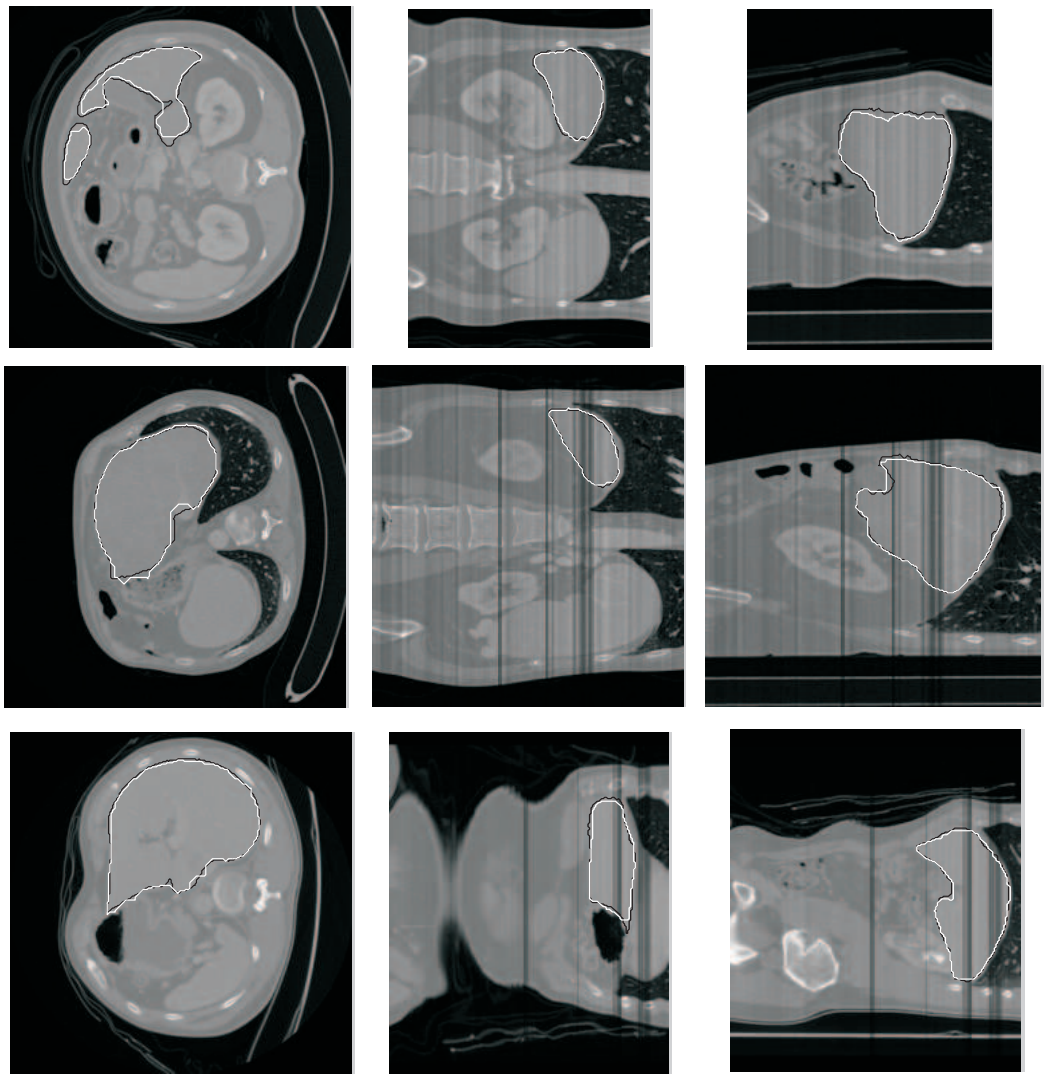

Figure 3.30: Sample results of liver segmentation in transverse (left column), coronal (center column) and sagittal (right column) directions; black contours: ground truth, white contours: boundaries identified by our work (MOVS).

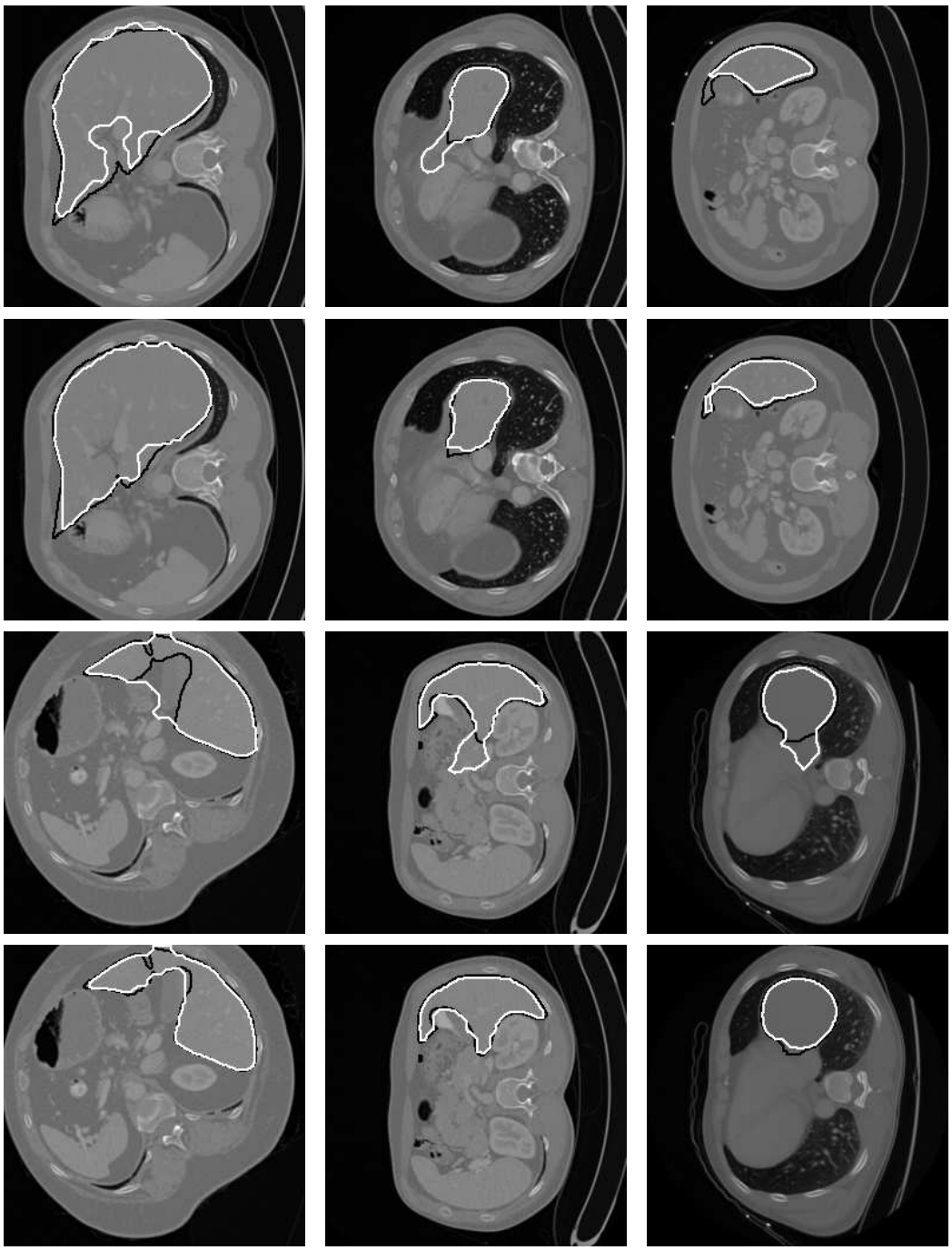

Figure 3.31: Comparison of the results of DERMS and MOVS over sample images. The first and third rows show the segmentation of DERMS with respect to ground truth; while the second and fourth rows show the segmentation of MOVS with respect to ground truth. Black contours belong to ground truth while white contours belong to (DERMS/MOVS) segmentation results in all cases.

Chapter 4

Experimental Results

This section presents complete results and discussions for both applications of the proposed method. In generating segmentation results, the dataset of MICCAI's 2007 grand challenge workshop is used. This dataset includes 20 training and 10 test CT scan volumes.

In the kidney case, 23 volumes (15 training and 8 test) was used. The MICCAI's grand challenge was designed for the liver 3D modeling and therefore some of its volumes did not include the kidney organ completely. Also, the training volumes did not include the ground truth for the kidney. Therefore, in the kidney application the ground truth for both training and test volumes were found manually.

For the liver, in order to generate the organ space for the PCA based model of the liver, first all 20 training volumes were used. The ground truth (liver masks for the training volumes) was provided by the MICCAI's workshop. The ground truth for the test volumes however was not provided but the quality of the results was measured against MICCAI's ground truth by MICCAI's workshop. By exchanging the role of training and test volumes and utilizing the manually found ground truth for one of the test volumes, we were able to present 30 test cases. Details of this process are presented in Section 4.2.

To compare the proposed method with the state of the art, two sets of measures are used. While both these sets can be estimated for each one of these applications, the first set is used for the kidney and the second set for the liver. This was imposed by the state of art, since we could not find any paper that represents both measures for both of these organs.

4.1 Results for Kidney Segmentation

The proposed solution has been applied on 20 test volumes. Also to make our comparison compatible with the state of art [39], the training phase utilizes 3 models based on 7, 10 and 15 training volumes. The ground truth was prepared manually for both training and test volumes. In order to accommodate the 15 training volumes and 20 test volumes (given that the entire MICCAI's dataset include only 23 (training and test) volumes with both kidneys entirely contained within the sets) the role of training and test volumes are exchanged at several points during the test results generation.

To evaluate the performance of this work on the kidney segmentation, following metrics and sensitivity measure are utilized.

i) Dice Coefficient: this is a similarity measure defined according to the following:

$$Dice = \frac{2|X \bigcap Y|}{|X| + |Y|} \tag{4.1}$$

here X is the segmentation result by our algorithm and Y is the gold standard (ground truth).

ii) Mean Square Error: this is computed by:

$$MSE = \frac{1}{\Omega} \sum (X - Y)^2 \tag{4.2}$$

here X and Y are segmentation results by our algorithm and manually found ground truth and Ω is the total number of the pixels in the union of X and Y.

iii) Sensitivity Measure: this is the ratio of correctly identified organ segments to the overall segments in the ground truth.

$$SE = \frac{TP}{TP + FN} \tag{4.3}$$

here TP is the True Positive and it represents the number of voxels that are segmented consistently (correctly) as kidney tissue by both the proposed method and the ground truth. FN is the False Negative and it represents the number of voxels that exist in the ground truth but were missed by our solution.

These measures are computed and are presented in Table 4.1 and Table 4.2. The results are separated according to the number of training sets and for left and right kidneys. The

mean Dice measure for the left and the right kidneys (across all three models) is 90% which shows slightly better results than the 88.6% presented by [22]. The results for SE (for training with 10 sets) indicate 15% improvement over the results presented by [39] (74%). Interestingly, our proposed method seems to perform rather uniformly regardless of the number of training sets. The presented MSE results are not compared against values reported by [39] due to the differences in the resolution, size, position and orientation of used datasets.

Sample segmentation results for the right kidney segmentation have been demonstrated graphically in Figures 4.1, 4.2, and 4.3, while sample segmentation results for the left kidney have been demonstrated graphcially in Figures 4.4, 4.5, and 4.6. Figures 4.1 and 4.4 show results in the transverse direction, Figures 4.2 and 4.5 depict results from sagittal direction and Figures 4.3 and 4.6 depict results in the coronal direction.

Table 4.1: Quantitative results for the right kidney extraction.

	Training by 7 sets			Training by 10 sets			Training by 15 sets		
Volume	Dice	MSE	SE	Dice	MSE	SE	Dice	MSE	SE
1	0.9357	1259	0.9538	0.9318	1417	0.9457	0.9287	1561	0.9356
2	0.8900	3901	0.9239	0.8970	3294	0.9469	0.8912	3439	0.9450
3	0.8828	2371	0.9655	0.8611	2870	0.9348	0.8602	2879	0.9347
4	0.9321	1163	0.9212	0.9357	971	0.9390	0.9207	1256	0.9193
5	0.8799	1711	0.9224	0.8779	1805	0.9185	0.8811	1659	0.9211
6	0.9479	4318	0.9536	0.9470	4323	0.9596	0.9512	3538	0.9658
7	0.8466	8849	0.7677	0.8835	6849	0.8239	0.7969	11052	0.6856
8	0.8872	1738	0.9384	0.8900	1902	0.9396	0.8914	1969	0.9332
9	0.8956	2969	0.9067	0.9317	2467	0.9108	0.9329	2151	0.9283
10	0.9278	2629	0.9230	0.9237	3735	0.8920	0.9316	2716	0.9162
11	0.8753	18719	0.8213	0.8726	19022	0.8188	0.8847	15578	0.8405
12	0.8458	10757	0.7921	0.8267	10914	0.7731	0.8658	8687	0.8519
13	0.9334	2698	0.9088	0.9386	2251	0.9263	0.9425	2029	0.9284
14	0.7262	6529	0.7500	0.8879	3109	0.8838	0.8930	2734	0.9051
15	0.9340	6793	0.8989	0.9479	3297	0.9462	0.9384	4686	0.9284
16	0.9463	3482	0.9306	0.9447	3479	0.9303	0.9436	3486	0.9289
17	0.8828	13716	0.8101	0.8767	12761	0.8030	0.9029	10495	0.8439
18	0.9266	3051	0.8822	0.9314	2708	0.8896	0.9338	2520	0.8969
19	0.9141	1125	0.8980	0.9087	1272	0.8765	0.9127	1225	0.8755
20	0.9187	4845	0.8787	0.9181	5272	0.8715	0.9222	4631	0.8851
Mean	**0.8964**	**5131**	**0.8873**	**0.9066**	**4686**	**0.8965**	**0.9063**	**4415**	**0.8985**

Table 4.2: Quantitative results for the left kidney extraction.

	Training by 7 sets			Training by 10 sets			Training by 15 sets		
Volume	Dice	MSE	SE	Dice	MSE	SE	Dice	MSE	SE
1	0.9169	1902	0.9115	0.9331	1197	0.9441	0.9273	1537	0.9183
2	0.9082	2911	0.9093	0.9105	3282	0.8964	0.9205	2248	0.9172
3	0.9157	1257	0.8983	0.9175	1236	0.8973	0.9137	1294	0.8972
4	0.8593	1426	0.8922	0.8195	1584	0.8891	0.8464	1574	0.8834
5	0.9374	4195	0.9404	0.9334	4306	0.9456	0.9325	5044	0.9281
6	0.9318	6405	0.9033	0.9343	6065	0.9064	0.9354	5529	0.9089
7	0.9120	2688	0.8883	0.9145	2588	0.9043	0.9157	2480	0.8970
8	0.8658	2168	0.9068	0.8951	1821	0.9079	0.8983	2006	0.8819
9	0.9176	2822	0.9063	0.9189	2471	0.9308	0.9263	2371	0.9302
10	0.9122	5019	0.9213	0.9166	5039	0.9075	0.9073	5482	0.8853
11	0.9103	11745	0.9158	0.9125	11787	0.9126	0.8916	15551	0.8663
12	0.9177	5814	0.9271	0.9057	6759	0.9040	0.8401	10743	0.7956
13	0.9149	3642	0.9123	0.9156	3427	0.8917	0.9123	3937	0.8940
14	0.8530	3602	0.8307	0.8424	3659	0.8131	0.8700	3476	0.8721
15	0.8885	9198	0.8782	0.8904	9166	0.8783	0.8888	9003	0.8928
16	0.9218	7445	0.9254	0.9257	6859	0.9345	0.9209	7023	0.9437
17	0.8676	15596	0.8259	0.9072	12399	0.9101	0.9296	9786	0.9429
18	0.8951	4923	0.8355	0.9293	2853	0.9082	0.9190	2894	0.9023
19	0.9015	1269	0.8878	0.8944	1367	0.8630	0.8808	1491	0.8492
20	0.8734	7892	0.8073	0.9065	4820	0.8737	0.9076	4994	0.8715
Mean	**0.9010**	**5096**	**0.8912**	**0.9062**	**4634**	**0.9009**	**0.9042**	**4923**	**0.8939**

4.2 Results for Liver Segmentation

In this section the proposed algorithms have been assessed for liver. In order to generate the organ space for the PCA based model of the liver, first all 20 training volumes are used. The ground truth (liver masks for the training volumes) was provided by the MICCAI's workshop. The ground truth for the test volumes however was not provided but the quality of the results was measured against MICCAI's ground truth by MICCAI's workshop.

Both DERMS and MOVS algorithms have been applied for the segmentation of the liver from test volumes. For further evaluation of MOVS, the number of test cases are extended by 20 more tests. This is done by using the ground truth of one of the test volumes (manually prepared) and 19 training volumes (leaving one out) to generate the organ space for the PCA model. The left out training volume (acts a test volume) was then modeled using

the PCA model. The measurements for these 20 cases were estimated using the assessment program that was provided by the MICCAI's workshop.

To evaluate the performance, the evaluation metrics of MICCAI's 2007 workshop [18][19] are adopted. Brief descriptions of these metrics are as follows.

i) Volumetric Overlap Error (in percent): This is the number of voxels in the intersection of segmentation and ground truth divided by the number of voxels in their union, subtracted from 1 and multiplied by 100.

ii) Relative Volume Difference (in percent): This is the total volume difference between segmentation and ground truth divided by total volume of ground truth multiplied by 100.

iii) Average Symmetric Surface Distance (in millimeters): First the Euclidean distance between every bordering voxel in segmentation and the closest bordering voxel in ground truth is determined. Then, the Euclidean distance between every bordering voxel in ground truth and the closest voxel in ground truth is determined. These two sets of distances are stored. The average of all these distances measures the Average Symmetric Absolute Surface Distance.

iv) Symmetric RMS Surface Distance (in millimeters): This measure is similar to the previous measure but here the squared distances are used and the root of the average value is taken.

v) Maximum Symmetric Absolute Surface Distance (in millimeters): This measure is similar to the two previous measures but only the maximum of all the distances is considered.

The results of DERMS for the test volumes, based on the above metrics, are shown in Table 4.3. Table 4.4 show the above metrics computed for the segmentation results of liver for MOVS. In this table, the row Mean^1 represents the mean of the MICCAI's test volumes and the row Mean^2 displays the mean for all the 30 test cases. The proposed algorithm achieves an average of 8.70% for Volume Overlap Error and an average of 1.51 mm for Average Symmetric Surface Distance. The best reported average values for these measures (6.65% and 1.03 mm) by an automatic algorithm on the same dataset are reported by [35]. The average quantitative results for liver segmentation based on all the aforementioned

measures show that, at the time of this publication, our algorithm stands among the top four automatic segmentation algorithms for liver extraction and are comparable to those presented by some of the interactive methods.

Sample segmentation results for liver segmentation have been demonstrated graphically in Figures 4.7, 4.8, and 4.9. Figure 4.7 shows results in the transverse direction, Figure 4.8 in the sagittal direction, and Figure 4.9 in the coronal direction.

Table 4.3: Quantitative results for the liver extraction based on DERMS algorithm.

Data set No.	Vol err %	Score	Ave diff %	Score	Ave dist [mm]	Score	RMS dist [mm]	Score	Max dist [mm]	Score	Total
1	10.08	60.63	-1.99	89.39	1.54	61.62	2.53	64.86	17.96	76.36	70.57
2	11.00	57.03	-3.57	81.02	1.90	52.58	4.13	42.67	40.95	46.11	55.88
3	12.18	52.41	-9.63	48.80	4.72	0.00	9.38	0.00	50.44	33.63	26.97
4	10.52	58.90	1.66	91.19	2.03	49.18	3.94	45.22	27.34	64.03	61.70
5	12.95	49.40	0.50	97.33	2.81	29.79	6.69	7.14	73.15	3.75	37.48
6	11.57	54.80	-4.03	78.59	1.91	52.15	3.32	53.88	24.28	68.05	61.49
7	9.55	62.71	2.30	87.77	2.21	44.83	5.67	21.23	47.68	37.26	50.76
8	9.68	62.18	0.99	94.74	2.25	43.73	4.58	36.33	34.81	54.20	58.24
9	8.34	67.41	-2.18	88.42	1.01	74.82	1.85	74.27	20.83	72.59	75.50
10	15.33	40.11	-6.18	67.11	3.55	11.25	6.66	7.57	37.20	51.06	35.42
Mean	**11.12**	**56.26**	**-2.21**	**82.44**	**2.39**	**41.99**	**4.87**	**35.32**	**37.47**	**50.70**	**53.40**

4.2.1 Execution

All the codes for this project are implemented in MATLAB 7.6.0.324 environment (on a PC with an Intel Core 2 Duo (2 GHz) processor) except for the generic segmentation algorithms (mean shift and graph based), which are performed in C++. Since for each slice of each volume, the segmentation algorithm is performed multiple times (60 times in the case of liver and 30 times in the case of kidney), a large percentage (about 80%) of the running time is spent on the segmentation process. The average runtime for extracting the liver mask of a single slice using the proposed algorithm is about 1 minute for both DERMS and MOVS algorithms since they both share the same multi-layer segmentation process. This time for kidney is about 40 seconds. Also the entire system can be programmed in C++ to make the execution time much faster.

To ensure the quality of the results, the segmentation parameters are chosen to have a

Table 4.4: Quantitative results for the liver extraction based on MOVS algorithm.

Results based on 20 training datasets

Data set No.	Vol err %	Score	Ave diff %	Score	Ave dist [mm]	Score	RMS dist [mm]	Score	Max dist [mm]	Score	Total
1	8.95	65.03	-4.69	75.04	1.32	66.98	2.52	65.06	18.37	75.83	69.59
2	9.90	61.32	-6.16	67.42	1.33	66.75	2.44	66.14	18.23	76.02	67.53
3	7.37	71.20	4.09	78.25	1.58	60.51	3.16	56.07	25.00	67.11	66.63
4	10.01	60.91	0.30	98.42	2.01	49.68	4.27	40.73	39.54	47.98	59.54
5	8.69	66.04	-5.28	71.92	1.45	63.71	2.83	60.73	23.73	68.78	66.24
6	8.12	68.28	-1.82	90.32	1.26	68.45	2.41	66.53	15.06	80.18	74.75
7	6.29	75.41	-2.81	85.08	0.86	78.41	1.67	76.85	12.99	82.91	79.73
8	7.83	69.40	-4.35	76.86	1.13	71.75	2.12	70.54	20.71	72.75	72.76
9	7.33	71.38	-1.03	94.54	0.90	77.39	1.78	75.23	20.77	72.67	78.24
10	10.90	57.41	-2.64	85.95	1.69	57.71	3.03	57.86	29.28	61.48	64.08
Mean[1]	**8.54**	**66.64**	**-2.44**	**82.38**	**1.35**	**66.14**	**2.62**	**63.57**	**22.37**	**70.57**	**69.86**
11	9.76	61.87	0.96	94.86	1.74	56.50	3.47	51.80	33.30	56.18	64.24
12	9.92	61.25	7.44	60.37	1.31	67.25	3.04	57.77	34.29	54.88	60.30
13	9.46	63.04	1.86	90.09	1.13	71.75	2.40	66.66	37.26	50.97	68.50
14	7.74	69.76	-1.16	93.78	1.54	61.5	3.58	50.27	33.25	56.25	66.31
15	8.72	65.93	-1.11	94.08	1.80	55.00	4.01	44.30	31.16	59.00	63.66
16	9.16	64.21	2.28	87.82	1.25	68.75	2.28	68.33	19.44	74.42	72.70
17	7.41	71.05	1.85	90.12	1.27	68.25	2.46	65.83	23.53	69.03	72.86
18	10.31	59.76	-1.76	90.60	2.51	37.25	4.64	35.55	41.25	45.72	53.77
19	8.22	67.89	2.94	84.31	1.51	62.65	2.71	62.36	26.70	64.86	68.33
20	9.53	62.77	1.38	92.60	2.22	44.50	4.31	40.13	35.51	53.27	58.65
21	9.74	61.95	-2.25	87.98	2.73	31.75	6.13	14.86	41.58	45.28	48.36
22	7.08	72.34	-1.95	89.58	1.40	65.00	3.22	55.27	38.78	48.97	66.26
23	8.56	66.56	-1.32	92.96	1.42	64.50	2.82	60.83	31.40	58.68	68.70
24	10.87	57.53	0.55	97.07	1.24	69.00	3.14	56.38	34.72	54.31	66.86
25	7.54	70.54	0.15	99.15	1.55	61.25	3.17	55.97	26.47	65.17	70.41
26	8.26	67.73	-2.69	85.66	1.84	54.00	3.93	45.41	32.75	56.90	61.94
27	8.53	66.67	2.48	86.78	1.26	68.50	2.47	65.69	23.02	69.71	71.47
28	9.99	60.97	-0.37	98.02	2.07	48.25	3.93	45.41	27.58	63.71	63.27
29	7.66	70.07	3.50	81.34	2.11	47.25	4.95	31.25	51.00	32.89	52.56
30	8.81	65.58	5.78	69.23	1.46	63.50	3.66	49.16	41.00	46.05	58.70
Mean[2]	**8.70**	**66.00**	**-0.76**	**85.35**	**1.51**	**62.22**	**3.06**	**57.37**	**27.78**	**63.44**	**66.88**

large range (covering results from under to over segmentation). This however contributes to substantially higher number of segmentation calls. One way of improving the execution time could be to lower the range of the parameters, concentrating only on the nominal values (as presented in Sections 3.4.3 and 3.5.3). This would cause an overall faster performance, but clearly in some cases the accuracy of the results will be compromised. By assessing the quality of the reconstructed model, we can decide whether further segmentation using an extended finer range of parameters is required or not. This should allow improving the results for such cases while reducing the mean processing time for the entire test volumes.

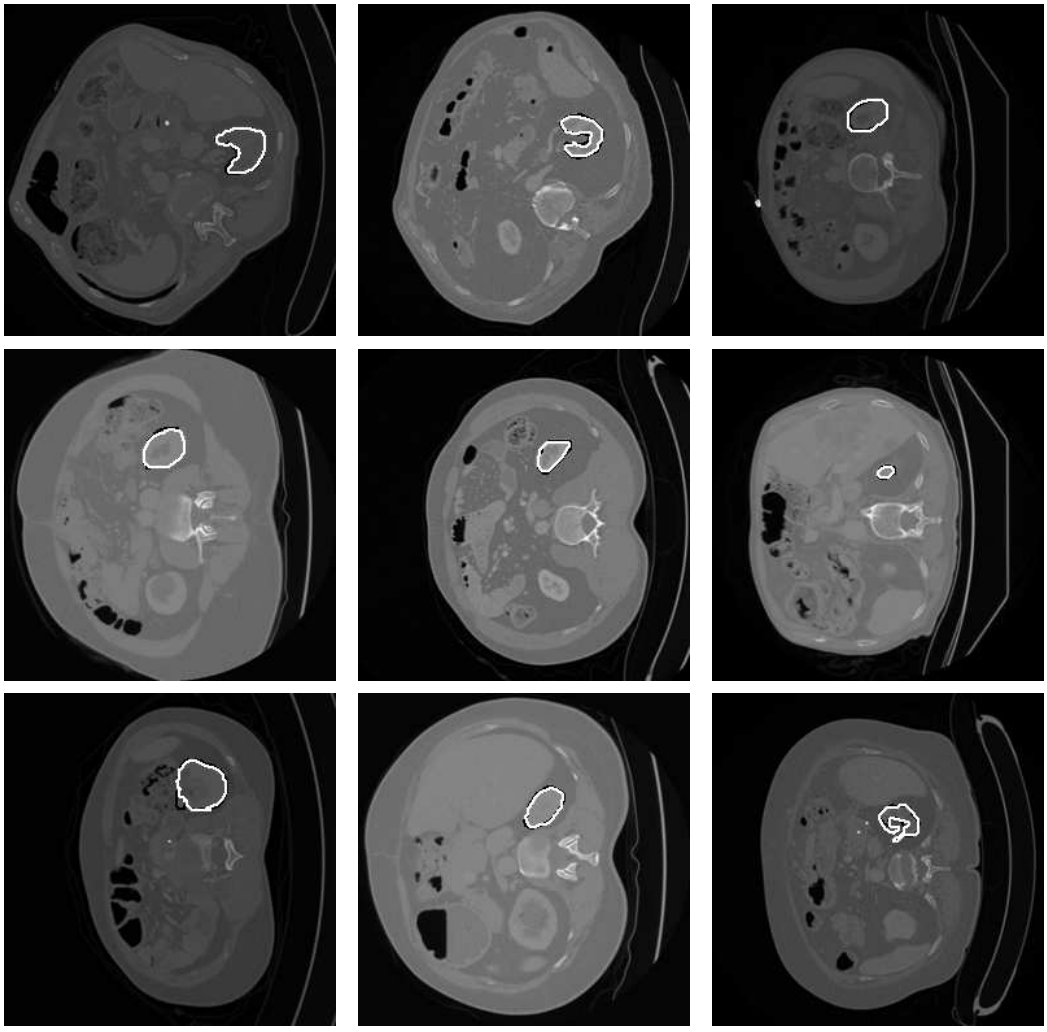

Figure 4.1: Sample right kidney results for transverse direction.

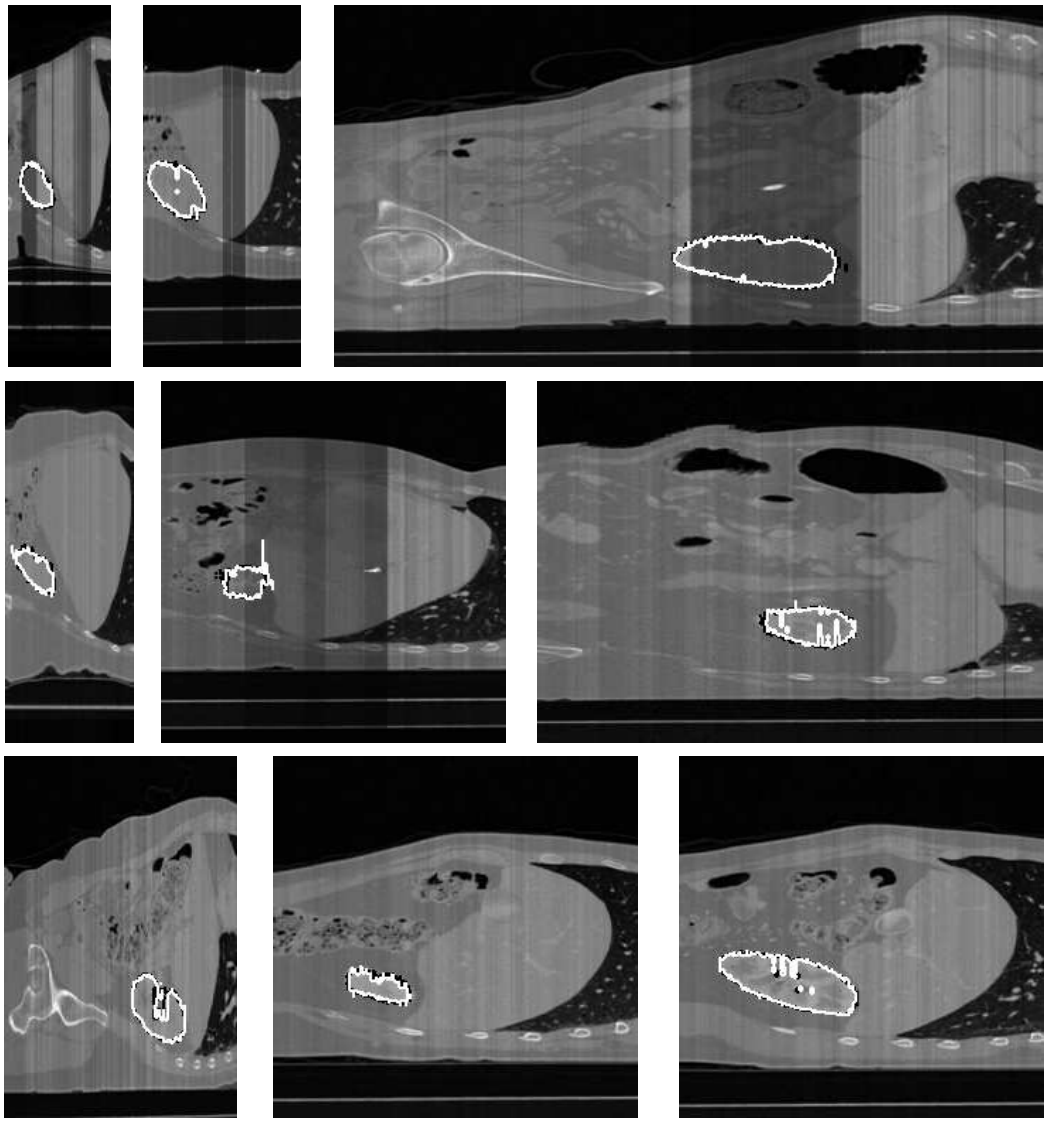

Figure 4.2: Sample right kidney results for sagittal direction.

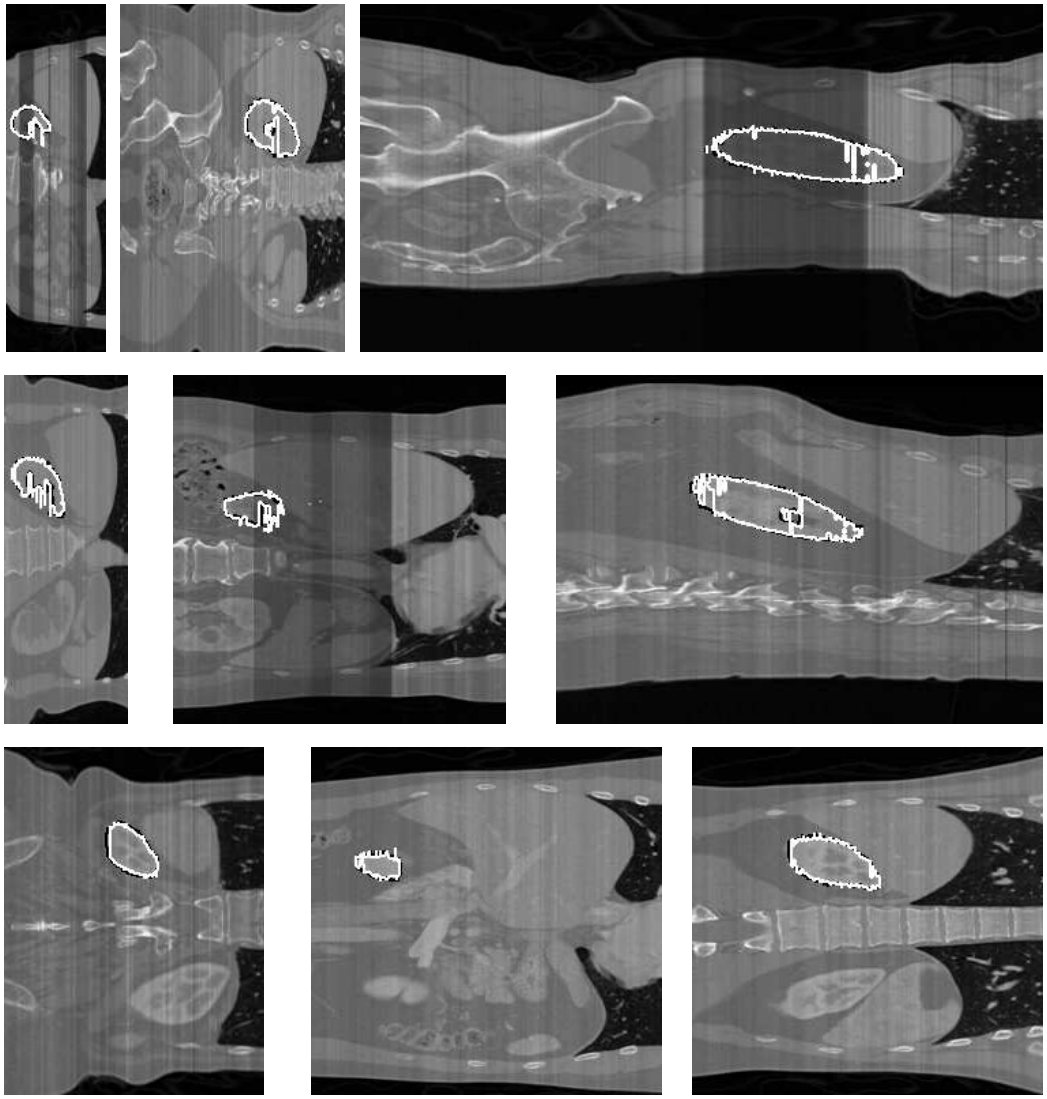

Figure 4.3: Sample right kidney results for coronal direction.

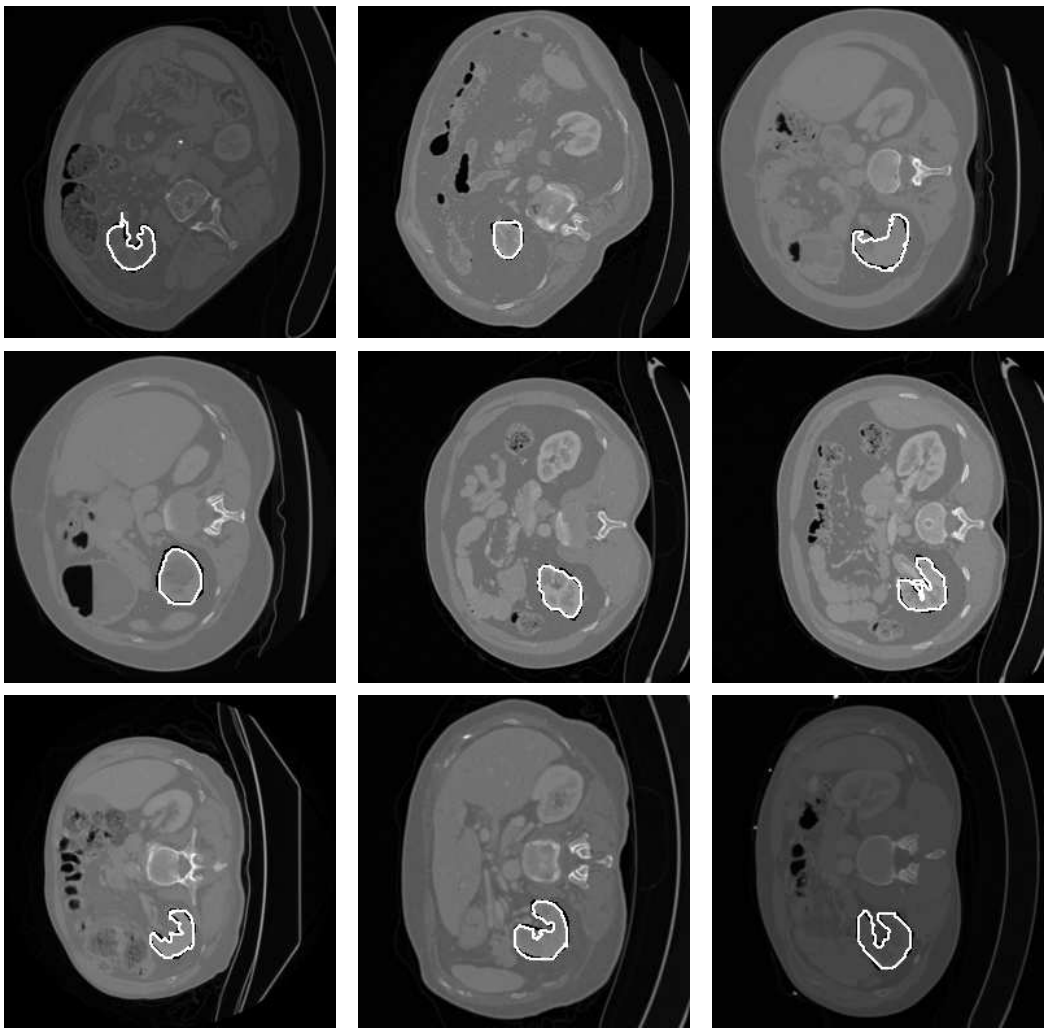

Figure 4.4: Sample left kidney results for transverse direction.

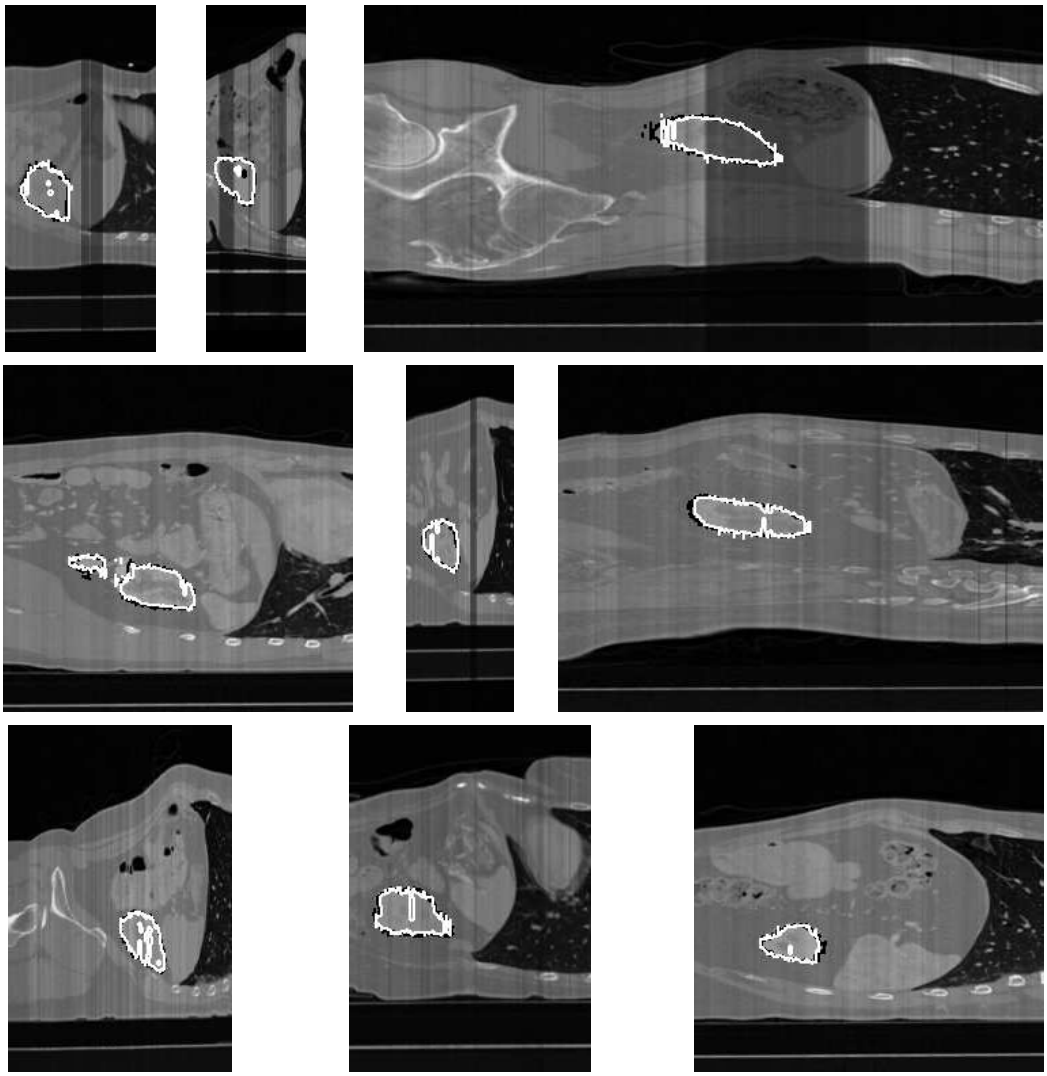

Figure 4.5: Sample left kidney results for sagittal direction.

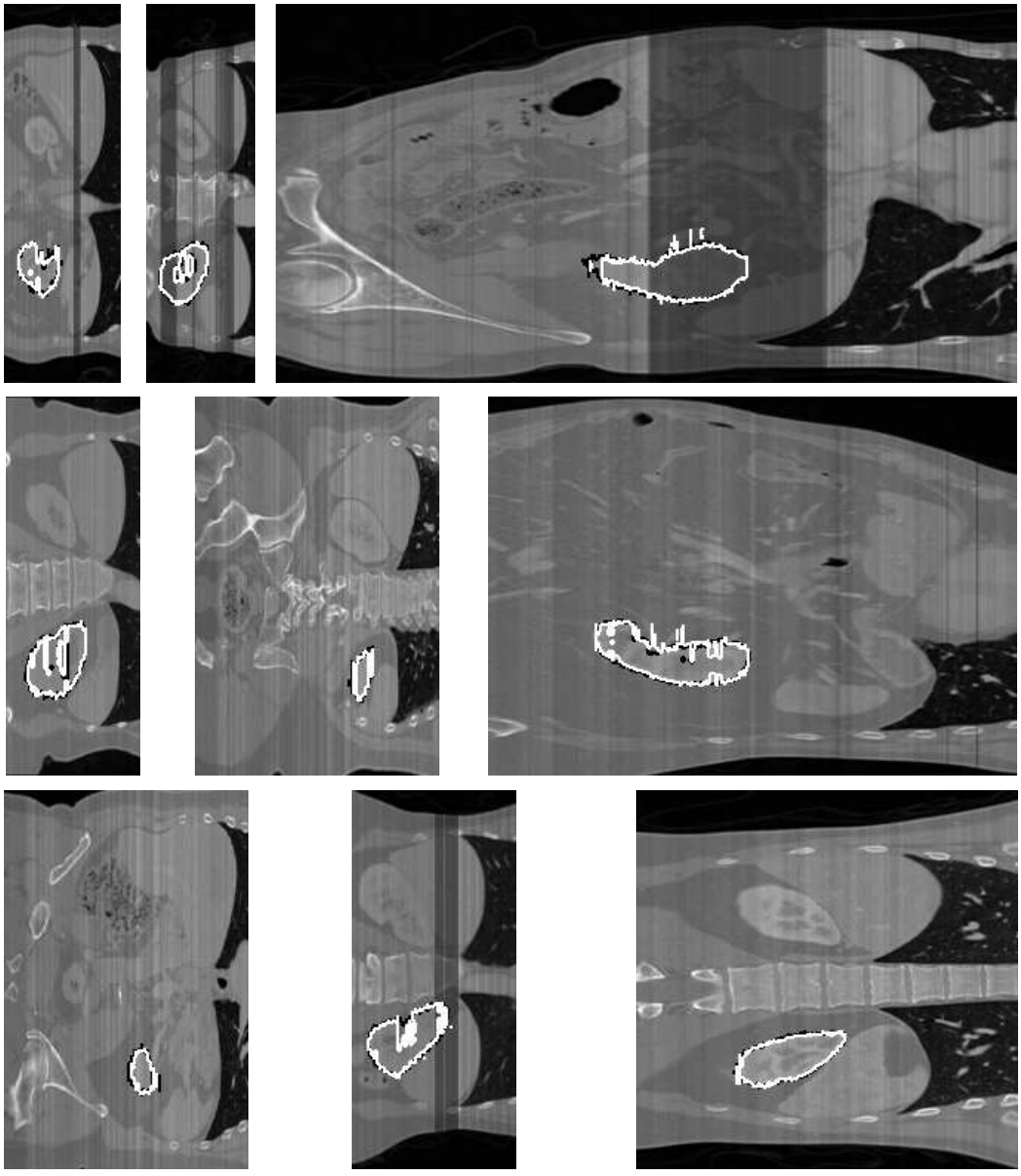

Figure 4.6: Sample left kidney results for coronal direction.

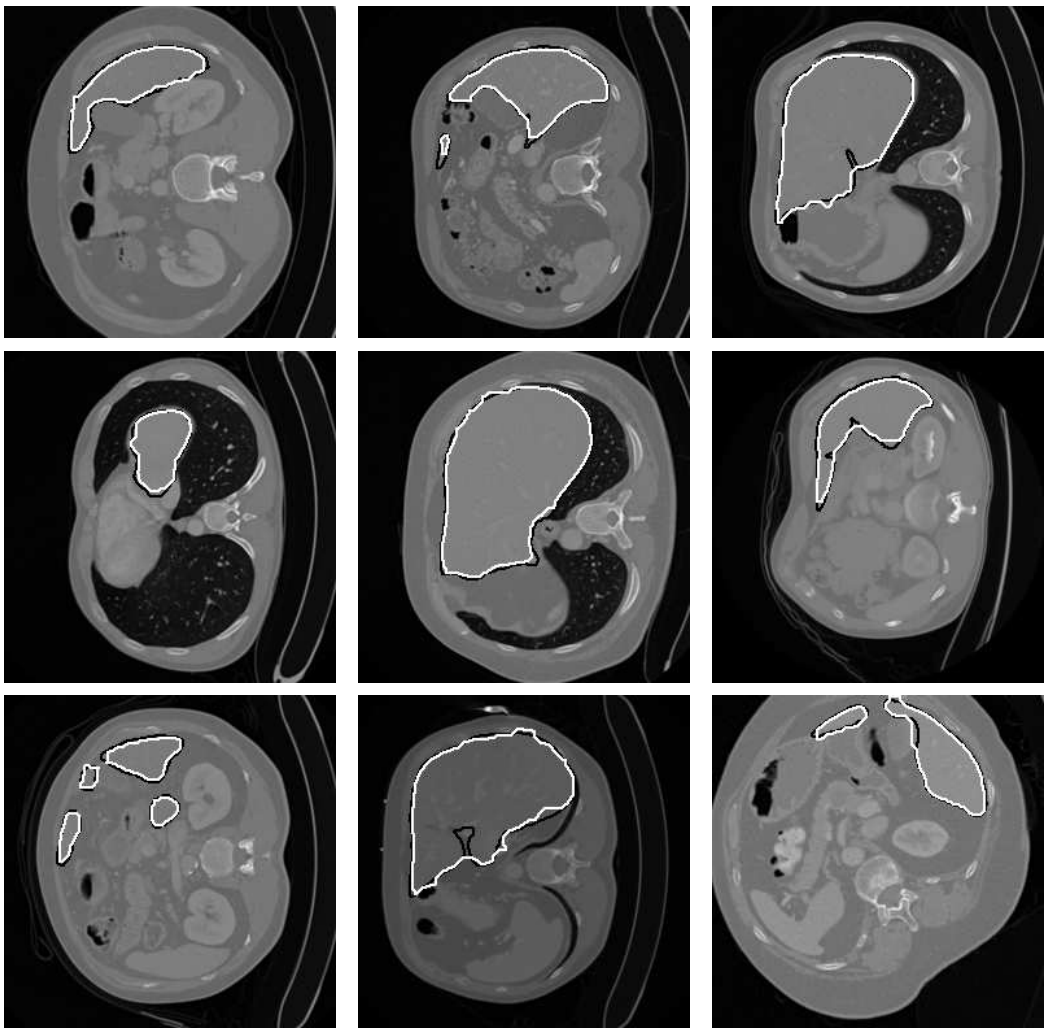

Figure 4.7: Sample liver results for transverse direction.

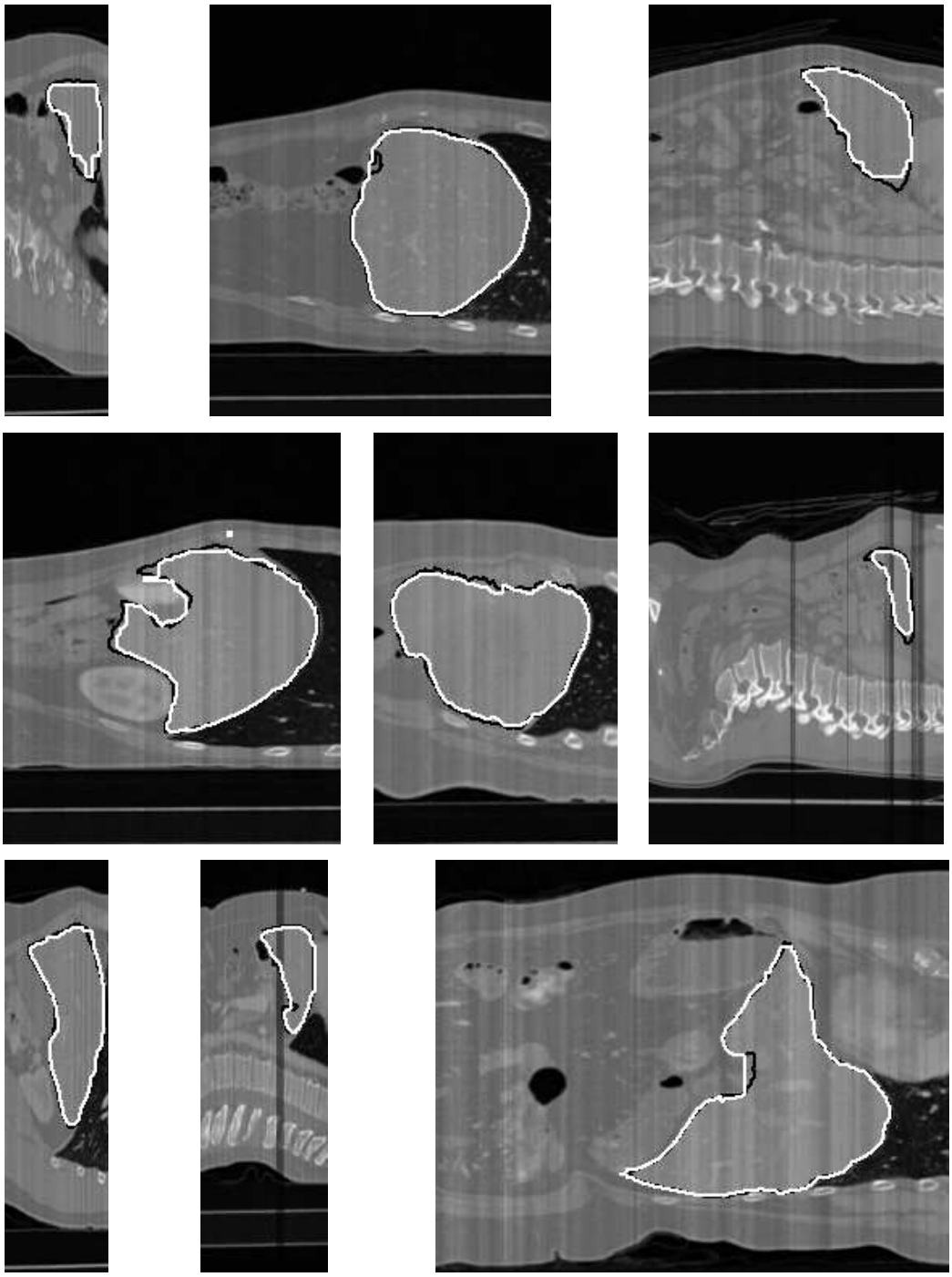

Figure 4.8: Sample liver results for sagittal direction.

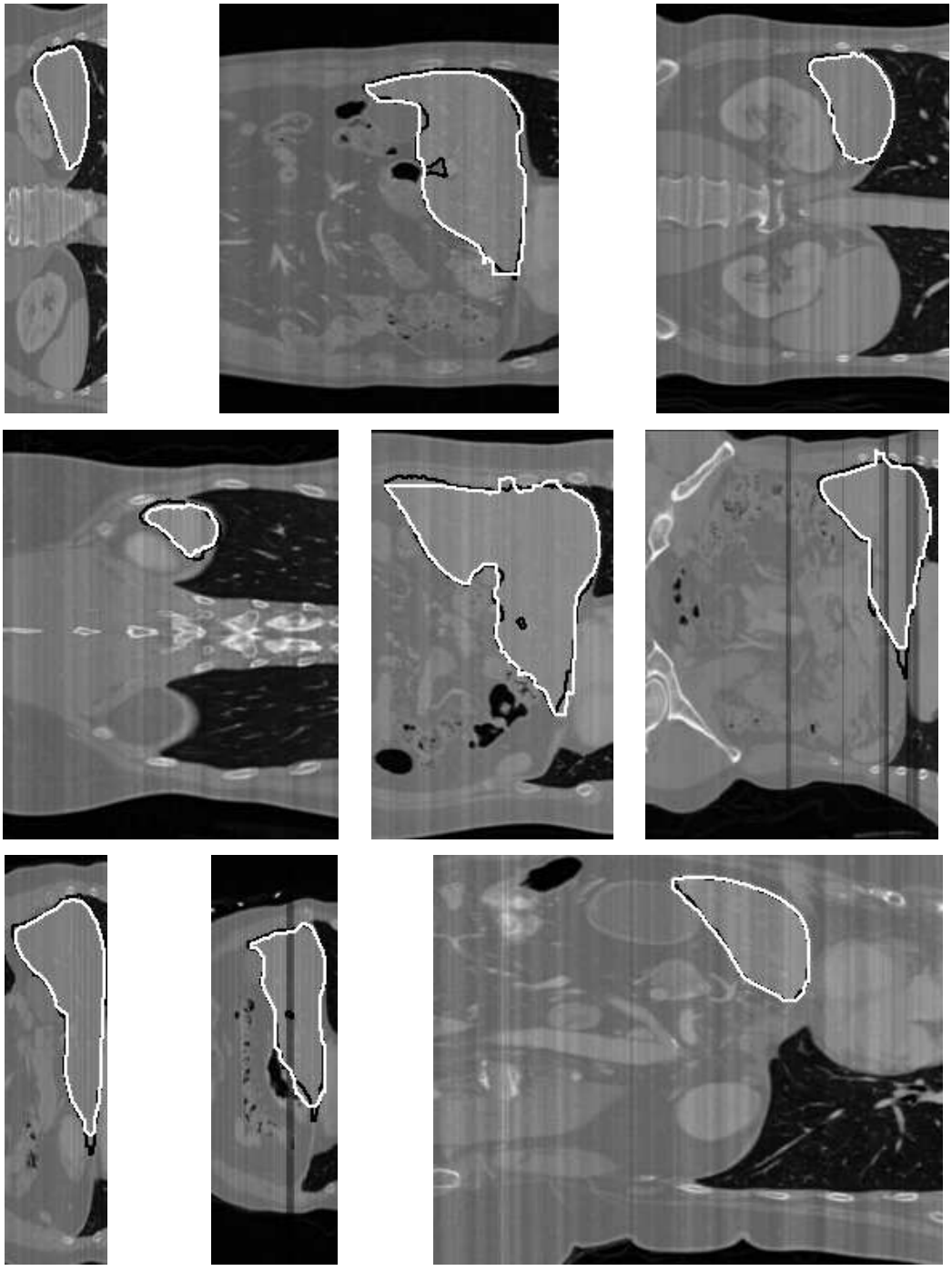

Figure 4.9: Sample liver results for coronal direction.

Chapter 5

Conclusions

In this work a problem in the field of biomedical image analysis has been addressed: development of an automatic organ segmentation algorithm from medical image data modalities such as CT scan.

An initial approach, named DERMS, was proposed that performed segmentation based on similarity of 2D organ shapes in consecutive slices of a CT scan volume and texture of the organ. Unfortunately the performance of DERMS tended to be highly dependent on the quality of the input image and when assessing on MICCAI's dataset, the results were not satisfactory. The poor performance of the DERMS algorithm can be explained by:

i) Hard coded parameters (that require to be adjusted for each case to perform satisfactory).

ii) Lack of a model to confirm the segmentation results.

To address both problems, another algorithm (called MOVS) was proposed. MOVS combined low-level segmentation schemes with statistical models to accurately identify organ's segments in CT images. MOVS includes a multi-layer segmentation scheme (through multiple parameter setting combinations) that enables segmentation of CT volumes that include non-linear and invariant intensity variations. Moreover, MOVS incorporates statistical model of the organ in the segmentation process in a unique way to automatically select the most appropriate low-level parameter setting (at the slice level). The use of statistical information through training datasets allows conforming the shape of segments to a predefined model.

The applications of MOVS were presented in details for segmentation of kidney and liver in CT scan volumes. Comparison of the performance with the state of art was demonstrated using MICCAI 2007 grand challenge dataset. Currently this work stands among the top four automatic algorithms reported for liver extraction on this dataset. Based on the results, two important conclusions can be drawn:

i) The MOVS organ segmentation algorithm is capable of segmentation of organs from medical image data with varying imaging conditions and different levels of illumination at the slice level. Experimental results have been performed over all the data volumes of MICCAI 2007 dataset and the same performance for darker images backs up this claim.

ii) This work has proven that object/organ models can be used as validation tools beside a bias in leading the segmentation algorithm to a predetermined direction. This work presented for the first time, the idea of such alternative use of a model in segmentation.

The proposed solution is considered to be a general approach that can be customized for general object detection and segmentation applications in areas other than medical image analysis.

The following two sections summarize the contributions of this work and its potential future research directions.

5.1 Contributions

In this work, two contributions toward the goal of organ segmentation from medical image data have been made:

i) Presenting a novel approach that instead of leading the segmentation process towards results that are biased by the prior information, validates all potential unbiased segmentation outcomes according to the statistical characteristics of the organ.

ii) Proposing a dynamic parameter setting scheme that allows automatic variation of segmentation quality control parameters at slice level and according to the fidelity of the generated output segments for that slice with the model.

5.2 Potential Future Research Direction

The following steps are the potential research direction for the future of this work.

i) The basic problem of the proposed approach is the speed of the algorithm. Due to nature of the proposed algorithm where a large number of segmentation candidates are generated, the time required to segment an organ from an image volume is relatively high. In order to overcome this issue, the range of the parameter set used to generate the candidates or the resolution of the input images can be reduced. Also, by running the algorithm on faster machines with larger memory space, the speed can be significantly increased.

ii) The proposed algorithm performs with just marginally lower scores compared to the best existing segmentation algorithm for segmentation of liver. Also the current method is capable of performing well for segmentation of other organs such as brain and heart as long as all variations occurring in the test inputs are encoded within the training samples. Therefore, it is proposed to use this algorithm as the general segmentation part of the planning phase in minimally invasive surgeries.

iii) This work was developed as part of a larger project on providing image guidance during surgery. As mentioned in Chapter 1, image guided minimally invasive procedures have two phases: pre-operative planning and intra-operative plan execution. This work accomplished developing an automatic segmentation tool for generating an organ model as part of the pre-operative planning phase. This work should be combined with a deformable model to generate a complete pre-operative plan.

iv) The second phase of every image guided minimally invasive surgery is the execution of plan which involves simulating the model generated in the pre-operative phase during the actual surgery. The simulation must be in full correspondence with what is actually happening in the body. In order to prepare and test the generated model for this phase, the model is generated and simulated for porcine, canine, and bovine internal organs or synthetic rubber phantoms. The next step of this project is to simulate the model generated in the first phase with actual or synthetic organ deformations as the final step of the realization of a system for providing visual guidance during surgery.

Bibliography

[1] Z.Yaniv and K.Cleary. Image-guided procedures: a review. *Technical report, Computer Aided Interventions and Medical Robotics (CAIMR), Georgetown University, Imaging Science and Information Systems Center, Washington, DC*, pages 1–63, 2006.

[2] H. Delingette and N. Ayache. Soft tissue modeling for surgery simulation. *Computational Models for the Human Body, Handbook of Numerical Analysis*, pages 453–550, 2004.

[3] T. K. Sinha R. L. Galloway D. M. Cash, M. I. Miga and W. C. Chapman. Compensating for intraoperative soft-tissue deformations using incomplete surface data and finite elements. *IEEE Transaction on Medical Imaging*, 24(11):1479–1491, 2005.

[4] A. P. King J. M. Blackall, G. P. Penney and D. J. Hawkes. Alignment of sparse freehand 3d ultrasound with preoperative images of the liver using models of respiratory motion and deformation. *IEEE Transaction on Medical Imaging*, 24(11):1405–1416, 2005.

[5] H. Badakhshannoory and P. Saeedi. Automatic liver segmentation from ct scans using multi-layer segmentation and principal component analysis. In *International Conference on Advances in Visual Computing*, pages 342–350, 2010.

[6] S. Samarasekeraa S. Sharmaa B. E. Hirschb A. X. Falcaoa, J. K. Udupaa and R. de A. Lotufo. User-steered image segmentation paradigms: Live wire and live lane. *Graphical Models and Image Processing*, 60:233–260, 1998.

[7] E. N. Mortensen and W. A. Barrett. Interactive segmentation with intelligent scissors. *Graphical Models and Image Processing*, 60:349–384, 1998.

[8] A. X. Falcaoa and J. K. Udupaa. A 3d generalization of user-steered live-wire segmentation. *Graphical Models and Image Processing*, 4:389–2000, 2000.

[9] G. Prause A. Schenk and H. O. Peitgen. Effcient semiautomatic segmentation of 3d objects in medical images. In *International Conference on Medical Image Computing and Computer Assisted Intervention (MICCAI)*, pages 186–195, 2000.

[10] S. Aharon. L. Grady, T. Schiwietz and R. Westermann. Random walks for interactive organ segmentation in two and three dimensions: Implementation and validation. In

International Conference on Medical Image Computing and Computer Assisted Intervention (MICCAI), pages 773–780, 2005.

[11] L. J. Reese. Intelligent paint: Region-based interactive image segmentation. *Master's thesis, Brigham Young University, Provo, UT*, 1999.

[12] S. A. Roll L. D. Griffin, A. C. F. Colchester and C. S. Studholme. Hierarchical segmentation satisfying constraints. In *British Machine Vision Conference*, pages 135–144, 1994.

[13] Y. Boykov and M. P. Jolly. Interactive organ segmentation using graph cuts. In *International Conference on Medical Image Computing and Computer Assisted Intervention (MICCAI)*, pages 276–286, 2000.

[14] Y. Boykov and M. P. Jolly. Interactive graph cuts for optimal boundary and region segmentation of objects in nd images. In *International Conference on Computer Vision (ICCV)*, pages 105–112, 2001.

[15] K. Shanmugam R.M. Haralick and I. Dinstein. Textural features for image classification. *IEEE Transaction on Systems, Man, and Cybernetics*, 3:610–621, 1973.

[16] D. Raicu R. Susomboon and J. Furst. Automatic single organ segmentation in computed tomography images. In *IEEE International Conference on Data Mining*, pages 1081–1086, 2006.

[17] D. Raicu R. Susomboon and J. Furst. A hybrid approach for liver segmentation. In *Proceedings of the MICCAI07 Grand Challenge, 3D Segmentation in the Clinic*, pages 151–160, 2007.

[18] M. Styner T. Heinmann and B. van Ginneken. 3d segmentation in the clinic - a grand challenge. In *International Conference on Medical Image Computing and Computer Assisted Intervention (MICCAI), Workshop Proceedings*, pages 7–15, 2007.

[19] B. van Ginneken T. Heinmann and M. Styner. Comparison and evaluation of methods for liver segmentation from ct datasets. *IEEE Transaction on Medical Imaging*, 28(8):1251–1265, 2009.

[20] S. Park K. Seo, L. C. Ludeman and J. Park. Efficient liver segmentation based on the spine. In *Advances in Information Systems*, volume 3261, pages 400–409, 2005.

[21] M. Hori A. H. Forouzan, R. A. Zoroofi and Y. Sato. Liver segmentation by intensity analysis and anatomical information in multi-slice ct images. *International Journal Computer Assisted Radiology and Surgery*, 4:287–297, 2009.

[22] C. C. Lei D. T. Lin and S. W. Hung. Computer-aided kidney segmentation on abdominal ct images. *IEEE Transaction on Information Technology in Biomedicine*, pages 59–65, 2006.

[23] T. F. Chan and L. A. Vese. Active contours without edges. *IEEE Transactions on Image Processing*, 10:266–277, 2001.

[24] S. Pan and B. M. Dawant. Automatic 3d segmentation of the liver from abdominal ct images: a level-set approach. *Society of Photographic Instrumentation Engineers (SPIE) on Medical Imaging*, 4322:128–138, 2001.

[25] J. Martel J. F. Garamendi, N. Malpica and E. Schiavi. Automatic segmentation of the liver in ct using level-sets without edges. In *Proceedings of the 3rd Iberian conference on Pattern Recognition and Image Analysis, Part I*, pages 161–168, 2007.

[26] T. Lambrou A. Linney A. Evans and A. Todd-Pokropek. Automatic segmentation of liver using a topology adaptive snake. In *Proceedings of the Second IASTED International Conference on Biomedical Engineering*, pages 205–208, 2004.

[27] C. H. Wu and Y. N. Sun. Segmentation of kidney from ultrasound b-mode images with texture based classification. *Journal of Computer Methods and Programs in Biomedicine*, 84:114–123, 2006.

[28] S. Lavallee A. Hamadeh and P. Cinquin. Automated 3 dimensional computed tomographic and fluoroscopic image registration. *Computer Aided Surgery*, 3:11–19, 1998.

[29] S. C. Joshi G. E. Christensen and M. I. Miller. Volumetric transformation of brain anatomy. *IEEE Transaction on Medical Imaging*, 16:864–877, 1997.

[30] J. P. Thirion F. Maes D. Vandermeulen B. M. Dawant, S. L. Hartmann and P. Demaerel. Automatic 3d segmentation of internal structures on the head in mr images using a combination of similarity and free form transormations: Part i, metholody and validation on normal subjects. *IEEE Transaction on Medical Imaging*, 18:909–916, 1999.

[31] Y. Chen B. C. Vemuri, J. Ye and C. M. Leonard. Image registration via levelset motion: applications to atlas-based segmentation. *Medical Image Analysis*, 7:1–20, 2003.

[32] D. H. Cooper T. F. Cootes, C. J. Taylor and J. Graham. Active shape models - their training and application. *Journal of Computer Vision and Image Understanding*, 61(1):38–59, 1995.

[33] C. J. Taylor T. F. Cootes and D. H. Cooper. Statistical models of appearance for medical image analysis and computer vision. *Society of Photographic Instrumentation Engineers (SPIE) on Medical Imaging*, 4322:236–248, 2001.

[34] G. J. Edwards T. F. Cootes and C. J. Taylor. Active appearance models. *IEEE Transaction on Pattern Analysis Machine Intelligence*, 23:681–685, 2001.

[35] T. Lange D. Kainmuller and H. Lamecker. Shape constrained automatic segmentation of the liver based on a heuristic intensity model. In *Proceedings of the MICCAI07 Grand Challenge, 3D Segmentation in the Clinic*, pages 109–116, 2007.

[36] H. P. Meinzer T. Heinmann and I. Wolf. A statistical deformable model for the segmentation of liver ct volumes. In *Proceedings of the MICCAI07 Grand Challenge, 3D Segmentation in the Clinic*, pages 161–166, 2007.

[37] Y. Zheng H. Ling, S. K. Zhou and B. Georgescu. Hierarchical, learning based automatic liver segmentation. In *IEEE Conference on Computer Vision and Pattern Recognition*, pages 1–8, 2008.

[38] G. Soza A. Wimmer and J. Hornegger. A generic probabilistic active shape model for organ segmentation. In *International Conference on Medical Image Computing and Computer Assisted Intervention (MICCAI)*, pages 26–33, 2009.

[39] V. Daum J. Wasza M. Spiegel, D. A. Hahn and J. Hornegger. Segmentation of kidney using a new active shape model generation technique based on non-rigid image registration. *Journal of Computerized Medical Imaging and Graphics*, 33:29–39, 2009.

[40] A. A. Farag A. M. Ali and A. S. El-Baz. Graph cuts framework for kidney segmentation with prior shape constraints. In *International Conference on Medical Image Computing and Computer Assisted Intervention (MICCAI)*, pages 384–392, 2007.

[41] S. C. Mitchell and J. G. Bosch. 3d active appearance models: segmentation of cardiac mr and ultrasound images. *IEEE Transaction on Mecical Imaging*, 21:1167–1178, 2002.

[42] B. K. Ersboll M. B. Stegmann and R. Larsen. Fame-a flexible appearance modeling environment. *IEEE Transaction on Mecical Imaging*, 22:1319–1331, 2003.

[43] R. J. van der Geest H. G. Bosch J. H. C. Reiber S. C. Mitchell, B. P. F. Lelieveldt and M. Sonka. Multistage hybrid active appearance model matching: segmentation of left and right ventricles in cardiac mr images. *IEEE Transaction on Mecical Imaging*, 20:415–423, 2001.

[44] H. Badakhshannoory P. Saeedi and K. Qayumi. Liver segmentation based on deformable registration and multi-layer segmentation. In *International Conference on Image Processing*, pages 2549–2552, 2010.

[45] D. Comaniciu and P. Meer. Mean shift: a robust approach toward feature space analysis. *IEEE Transanction on Pattern Analysis and Machine Intelligence*, 24(5):603–619, 2002.

[46] P. F. Felzenszwalb and D. P. Huttenlocher. Efficient graph based image segmentation. *International Journal of Computer Vision*, 59:167–181, 2004.

[47] T. G. Herman. *Fundamentals of computerized tomography: image reconstruction from projection (2nd Edition)*. Springer, 2009.

[48] W. E. Lorensen and H. E. Cline. Marching cubes: a high resolution 3d surface construction algorithm. In *Proceedings of the annual conference on Computer graphics and interactive techniques SIGGRAPH '87*, volume 21, pages 163–169, 1987.

[49] B. Glocker, N. Komodakis, G. Tziritas, N. Navab, and N. Paragios. Dense image registration through mrfs and efficient linear programming. *Medical Image Analysis*, 12(6):731–741, 2008.

[50] N. Komodakis, G. Tziritas, and N. Paragios. Fast, approximately optimal solutions for single and dynamic mrfs. In *IEEE Conference on Computer Vision and Pattern Recognition*, pages 1–8, 2007.

[51] R. C. Gonzalez and R. E. Woods. *Digital image processing (2nd Edition)*. Prentice Hall, January 2002.

[52] M. Turk and A. Pentland. Eigenfaces for recognition. *Journal of Cognitive Neuroscience*, 3(1):71–86, 1991.

[53] M. Turk and A. Pentland. Face recognition using eigenfaces. In *IEEE Conference on Computer Vision and Pattern Recognition*, pages 586–591, 1991.

[54] T. Duchamp J. McDonald H. Hoppe, T. DeRose and W. Stuetzle. Surface reconstruction from unorganized points. In *Proceedings of the annual conference on Computer graphics and interactive techniques SIGGRAPH '92*, pages 71–78, 1992.

[55] V. Blanz and T. Vetter. A morphable model for the synthesis of 3d faces. In *Proceedings of the annual conference on Computer graphics and interactive techniques SIGGRAPH '99*, pages 187–194, 1999.

[56] A. R. Webb. *Statistical pattern recognition (2nd Edition)*. Wiley, 2002.